Analysis and Optimization for Volume Holographic Recording

A thesis
Presented to
The Academic Faculty

by

Omid Momtahan

In Partial Fulfillment
of the Requirements for the degree of
Doctor of Philosophy in Electrical and Computer Engineering

School of Electrical and Computer Engineering
Georgia Institute of Technology
August 2006

Analysis and Optimization for Volume Holographic Recording

Approved by:

Professor Ali Adibi, Advisor
School of Electrical and Computer Engineering
Georgia Institute of Technology

Professor Thomas K. Gaylord
School of Electrical and Computer Engineering
Georgia Institute of Technology

Professor John A. Buck
School of Electrical and Computer Engineering
Georgia Institute of Technology

Professor Glenn S. Smith
School of Electrical and Computer Engineering
Georgia Institute of Technology

Professor Rick Trebino
School of Physics
Georgia Institute of Technology

Date Approved: 07/06/2006

In the name of God, Most Gracious, Most Merciful

In memory of my mother and my grandmother

and

thanks to my father and my wife

Acknowledgments

Acknowledgement is one of the most read parts of any thesis, I believe. That's why I do my best to keep it less boring while conveying my deepest appreciations to all who helped me. Many people have helped me during my studies and moreover my life. My sincere thanks go to all of them.

I have known Prof. Ali Adibi, my PhD advisor, from 1990 when I was a high school student. He was my Trigonometric teacher. At that time, he had just finished his B.Sc. with highest honor (he holds the record for the highest GPA in Shiraz University's history, I believe). He was teaching in my high school, while preparing for the national entrance exam of graduate studies, in which he achieved the first rank. He was a very talented teacher and challenged us a lot during his course. He was a real inspiration to me specially that he was tall and thin, just as I was (yes, at that time he was very thin)! Knowing this short background, you can imagine how delighted I was, when I got the opportunity to do my PhD under his supervision. It was like a dream come true.

During my PhD, Prof. Adibi has been both a great advisor and friend for me. At work, I have benefited from his ideas, encouragements, knowledge, and advices. Outside the work, he has been a brilliant friend, an honest consultant, and a tough competitor. We have competed in almost all the sports; volleyball, football, basketball, bowling … He has excellent athletic capabilities and he loves challenges. I have had a lot of wonderful memories with him during my PhD. It is impossible to thank him for every thing, I can only say that it was once in a lifetime opportunity to know him and to work with him, and I am proud of having that opportunity. Also, I would like to express my sincere thanks to his family, as they have been a great supporter of my wife and me all this time.

Being Prof. Adibi's first PhD student provided me the unique opportunity to have all his group members' support. I am indebted to all of my friends in Photonics Group. I am grateful to Mr. Chaoray Hsieh (Jerry), who has been a perfect collaborator. He is an organized, hard working, self-motivated, and smart researcher. Furthermore, he knows how to find great deals on ebay and fatwallet! I enjoyed working with him and I hope him all the best in his studies. I am grateful to Mr. Arash Karbaschi, my dear friend for more than 15 years, for all of his support and help. It has been wonderful to study and work with him at Georgia Tech. Having almost similar background, working on similar projects, sharing the same office, living in the same neighborhood, and … made me think that if someone converts the information about Arash and I to binary codes, they will differ only in a few bits!! I hope we will be in close contact after graduation too. I appreciate Mr. Babak Momeni for all his help and also for being such a kind and trustable friend. His clear understanding of optics and willingness to discuss scientific problems helped and motivated me in my research. I definitely will miss his thoughtful comments when I leave Georgia Tech. Other group members that I am really grateful to are Mr. Fengtao Wang, Mr. George Cadena, Mr. Trenton Ensley, Miss Atefeh Makhmalbaf, Mr. Mohammad Soltani, Mr. Ali Asghar Eftekhar (Reza), Mr. Ali Akbar Jafarpour (Saman), Mr. Majid Badiei (Seyed), and Dr. Siva Yegnanarayanan. Also, special thanks to Mr. Pouyan Mohajerani (Morab) for being such a great trainer and companion in the gym. I am thankful to all the other friends at Georgia Tech who helped me during my PhD. Especial thanks to Mr. Reza Sarvari, Dr. Azad Naeimi, Dr. Kaveh Shakeri, Dr. Sahar Javanmard, and Dr. Babak Nikoubakht. Also, I am grateful to Mr. Michael Sullivan from Duke University for his thoughtful discussions.

I believe I have had great teachers and outstanding friends from whom I learned a lot. I am grateful to all my teachers. I think it is necessary to mention the ones who helped me the most to succeed in my education endeavor. Especially, I would like to thank Mr. Hosseini-Motlagh, my math teacher in the 7th grade, who really taught me how to learn mathematics. I am thankful to Mr. Kamali, my physics teacher in the 11th grade, who introduced me a new way of thinking about physics problems. I was not successful in my physics courses until I had the chance to learn from him. I am really grateful to Mr. Bambai-ro, my literature teacher in high school, who has been a role model for me. His perfect skills in teaching and clear way of thinking about everything were inspiring to me. Worth to mention that I have not had tea for more than 16 years, as he advised us not to get addicted to any thing, no matter how minor it is!! I indebted to Prof. Seyedian from the Department of Civil Engineering, Shiraz University, with whom I took the Engineering Mathematic course. I remember the class was from 1:00 pm to 2:30 pm (right after lunch). If Dr. Seyedian had not taught that course, I would have enjoyed a sweet nap in each session! In his class, I didn't even think about it, I was 100% in the class grabbing all he was explaining. During my graduate studies at Sharif University of Technology, I had the chance to work under supervision of Prof. Hashemi. Also, I took a course with him and was the tutor of one of his courses. He has been a great mentor to me and I am really grateful to all he did for me. Also, I would like to remember the late Prof. Barkeshli, who was the head of the Electrical Engineering Department, Sharif University of Technology at the time I was a graduate student. He was an outstanding professor and an extremely kind person who helped me considerably in the process of applying for PhD. At Georgia Institute of Technology, I would like to

thank all the professors I had courses with, especially Prof. Gaylord, Prof. Bulk, Prof. Trebino, and Prof. Adibi. I am also very grateful to all the committee members of my thesis. Also, I am indebted to Prof. David J. Brady from Duke University, for his thoughtful guidance and interesting discussions.

The last but definitely not least, I am thankful to my parents, my wife, my brother, my sister, and my grandmother. Besides all the good things they have done for me I would like to mention a few and appreciate them. My mother had an important role in my education as she always tried her best to register me in the outstanding education programs. For instance, the high school that I attended was so excellent at that time that it had the highest success rate in the National Physics Olympiad among all the schools in the nation. My father has always respected science and scientists and advised me to do so. My sister curiosity about science and perseverance in learning have been exceptional and she has been always a great inspiration to me. My brother has been my greatest motivator in learning math and physics. I remember once I was asked a surprise question that who had encouraged me the most. I thought and replied immediately that my brother had. I believe he has been an exceptional inspiration to me in learning Physics and Math. My grandmother always encouraged me to pursue my studies. To her, being educated was very important. Unfortunately, she could not wait to see his grandson graduation.

I started my PhD right after marrying my college sweetheart, Sharareh. She has been an affectionate wife, a close friend, a helpful adviser, and a strong supporter during the last six years. I believe that the long period of my PhD was very hard for her and I apologize for that. I am really thankful to her and I am sure it would have been much more difficult, if I had not had her support and motivation.

Table of Contents

List of Tables

List of Figures

Summary

Applications of volume holography can be categorized into two main groups. In the first group of applications, the exact reference or signal beam is used to read the hologram. In the second group of applications, the beam that is used to read the hologram might be completely different from the signal and the reference beams used for recording. Optimization of the volume holography is needed for both groups of applications. In the first group of applications (mainly storage systems), the designs and the techniques of volume holography are well known and the main optimization effort is finding the proper material to store the holograms. One of the results of this research is complete global optimization of dynamic range and sensitivity in two-center recording that is the best technique for persistent rewritable storage. For this purpose, a complete theoretical analysis as well as experimental demonstration is presented. Also, other effects and processes such as electron tunneling and recording at high temperature are considered to improve the dynamic range of the material.

For the second group of applications (mainly holographic optical elements), the focus of this research is on analysis and optimization of the design of the volume holograms in contrast to material optimization. A new method (multi-grating method) is developed for the analysis of an arbitrary hologram that is based on the representation of the hologram as the superposition of several plane wave gratings. Based on this method, a new class of optical devices that integrates the functionalities of different optical elements into a simple volume hologram is introduced and analyzed. As a result, very compact, low cost, and easy to use devices such as portable spectrometers can be made with particular applications in biological and environmental sensing. As an example of

such devices, a slitless volume holographic spectrometer lumps three elements (the entrance slit, the collimator, and the diffractive element) of the conventional spectrometer into one spherical beam volume hologram.

Chapter 1

Introduction and Background

The invention of holography by Gabor in 1948 [1] has motivated both scientists and the artists over the decades. Holography is mainly known as the recording of the coherent interference pattern of a desired beam (the signal beam) with a reference beam. When either the reference beam or the signal beam illuminates the hologram, a beam exactly similar to the other beam will be diffracted from the hologram.

Recording the interference patterns over the volume of the holographic material (volume holography) provides a selective diffraction property known as Bragg selectivity. The maximum diffraction from the volume hologram can be obtained when the reading beam is Bragg matched with one of the recording beams. For reading at the same wavelength, the Bragg matched beam is exactly similar to the reference beam or the signal beam. For example for the case of recording a hologram using a plane wave reference beam, the Bragg matched reading beam has the same incident angle as the reference plane wave. Changing the angle of the reading beam results in partial Bragg-matched condition and partial diffraction from the hologram is obtained. The selective diffraction of the hologram as a function of the change in the incident angle of the reading beam is called angular selectivity. Similar to the incident angle, changing the wavelength of the reading beam results in partial Bragg matching condition. In this case, the selective diffraction of the hologram is called wavelength selectivity.

The Bragg selectivity in volume holography is very important for different applications. Using the angular selectivity, different signal beams can be recorded in the

same volume when the incident angles of the corresponding reference beams are different [2]. Holographic storage is one of the main applications of volume holography that enables a large amount of data to be recorded in the entire volume of the material, which in principle can provide storage capacities up to 1 Tbit/cm^3 [3-6]. Another example of the selectivity of volume holography is based on the selective mode coupling of the holographic optical elements that can be used for imaging and spectroscopic applications [7, 8].

To efficiently utilize the diffraction properties of the volume holograms, accurate analytic tools for modeling and designing are required. The theoretical study of holograms has a long history. The correct representation of the intensity interference is the core of the modeling for thin holograms and used for different applications [2-3]. We refer to a thin hologram as a hologram that is not selective or has more than one diffraction order. The volume holograms or Bragg gratings were modeled accurately by Kogelnik that is known as coupled wave analysis [9]. The selective properties of a Bragg grating (recorded using two plane waves) were completely explained by this model. Further extensions of this model were used to obtain the complete diffraction, reflection, and transmitted components of a plane wave from a grating (either thin or thick) at any wavelength [10]. Most of these methods are useful for analysis of a simple grating formed by the interference pattern of two plane waves and read by a plane wave or multiple plane waves. While these methods are accurate with minimal assumptions and approximations, they are usually numerical based analysis and have limited application for designing complicated holograms.

A different set of analysis based on Born approximation is used to find the diffraction from holograms with small modulation depth (weak hologram) [11]. In the Born approximation the depletion of the reading beam, caused by the coupling between the reading beam and the diffracted beam, is ignored. While this approximation is valid for limited number of applications, it provides closed form solutions for most of the cases. Therefore, a better insight to the problem is obtained specially for designing applications.

Modeling the formation of the holographic inside the material is as important as the analysis of the diffraction from the holograms. The mechanism of the holographic recording is different in different materials. In general, the holographic materials can be divided into two major groups of read-only and rewritable materials. The holographic recording in read-only material is usually followed by a development process for revealing and permanently storing the hologram. After that, reading the hologram would not affect or change it. Also, the hologram cannot be easily erased and cannot be rerecorded in these materials. Examples of these materials are dichromated gelatin [12] and photopolymers [13]. On the other hand, in rewritable holographic materials, a hologram can be recorded, erased, and rerecorded. The best example of rewritable materials is the photorefractive crystals. Among the photorefractive crystals, lithium niobate ($LiNbO_3$) has been most extensively investigated [14, 16]. Conventional holographic recording experiments were performed in singly doped $LiNbO_3$ crystals, especially in $LiNbO_3$:Fe [14,16] and $LiNbO_3$:Cu [17-18]. In these materials, the reading process is similar to recording a uniform intensity pattern; therefore, the original holograms will be erased during the readout (destructive readout). This is the main

drawback of holographic recording in photorefractive crystals. Several methods, like thermal fixing [19-20], electrical fixing [21-22], readout with wave-vector spectra [23-24], two-step recording [25-28], and two-center recording [29-30], have been proposed for persistent holographic recording. Fixing techniques extends the lifetime of the holograms considerably while still the whole process is reversible; the holograms can be erased, and a new hologram can be recorded.

Among different fixing methods, two-step recording and two-center recording are all-optical processes and require no specific preprocessing (such as pre-distortion in readout with wave-vector spectra) or post-processing (such as fixing in thermal and electrical fixing). The reference and the signal beam record a hologram inside the material in the presence of a sensitizing or a gating beam. During the readout the gating beam is not present and the hologram is persistent. For erasure and recording of the hologram, the gating beam should be present. The two-step recording is a sophisticated technique requiring high power pulsed laser for sensitizing the material. While the two schemes have some similarities, the two-step recording has lower performance compared to two-center recording and requires sensitizing and recording beams with much higher intensities [31].

The use of accurate analysis and modeling for volume holographic recording is important for different applications. While the concept of volume holography remains the same, each specific application could be analyzed and modeled more efficiently if the physics of the problem was considered. To improve the performance of volume holography, we develop the analytic tools and models needed for modeling different groups of applications. For this purpose, the modeling of the volume holography is

categorized into two different groups of applications. In the first group, the design of the hologram is well known and the main challenge is to improve the performance of the material used for recording the hologram. Examples of the applications in this groups are holographic data storage and holographic correlators [6, 32].For this group of applications, the main focus is on the material optimization for read/write recording. As explained before, two-center recording in doubly doped lithium niobate is the best candidate to record holograms for these applications. To obtain the best performance in these applications, we investigate and perform a global optimization of the persistent holographic recording in this thesis. Also, new ideas for further improvement of the material performance for specific applications are presented.

In the second group of applications, the main challenge is the design of the hologram rather than the material used for the recording process. The holographic devices IN this group are usually called holographic optical elements (HOEs) that are parts of general optical systems. Holographic lenses used in imaging systems and volume holograms used as dispersive components for spectroscopy are examples of HOEs [7-8]. In this group of applications, a holographic element is recorded once and used several times. The material that is used for these holographic elements should last for a long time and should not be erased under the light illumination. Therefore, read only holographic materials, such photopolymers, are the best candidates for these applications. While the optimization of these materials is still an active research topic, the performance of the photopolymer materials is adequate for most of the applications. The efficient and accurate modeling of the holographic elements is the main concern for this group of applications. For this purpose, a complete model for diffraction calculation from a general hologram is

developed that could be used for optimization of different holographic devices. Our new method (multi-grating method) for the analysis of a complicated hologram is based on the representation of the hologram as the superposition of several plane wave gratings. In particular, the dispersive properties of spherical beam volume holograms (SBVHs) are analyzed based on the multi-grating method. A SBVH is a volume hologram recorded using a spherical beam and a plane wave. Based on the analysis of these devices, we present a new class of compact and easy to use spectrometers that are suitable for potable applications in biological and environmental sensing. The complete design and analysis of such spectrometer are presented in this work.

After this introduction and in Chapter 2, a complete analysis of the two-center holographic recording is presented. The model is used to find the optimum performance for persistent holographic recording in $LiNbO_3$:Fe:Mn. In Chapter 3, a software based stabilizer system for holographic recording is introduced that is essential in material characterization in two-center recording. The system is used to characterize the material designed based on the optimization approach in Chapter 2. The two-center recording in highly doped lithium niobate crystals is investigated in Chapter 4. The two-center recording model is extended to consider the effect of high dopant concentration. In Chapter 5, the effect of high temperature on the tow-center recording is investigated in detail. The experimental data as well as theoretical analysis of the thermal fixing in two-center recording is presented in this chapter. In Chapter 6, a new method for modeling diffraction from complicated holograms is introduced. Particularly, this method is used for analysis of a spherical beam volume hologram. A new class of slitless spectrometers based on spherical beam volume holograms is introduced and analyzed in Chapter 7. The

performance of the spectrometers based on spherical beam volume hologram is compared with the conventional spectrometers in this chapter. The extension of the analytic model for any arbitrary hologram is introduced in Chapter 8 and it is used for analysis of lensless spectrometer based on spherical beam volume hologram. The conclusions and future works are summarized in Chapter 9.

Chapter 2

Analysis and Optimization of Two-center Holographic Recording

2.1 Introduction

Two-center holographic recording proposed recently attracted attention for recording persistence holograms. This method is based on using two different dopants to provide shallower and deeper traps in photorefractive crystals [29]. The interference pattern of two lower-frequency (longer wavelength) beams (reference and signal beams) is recorded in the presence of a higher-frequency (shorter wavelength) beam (sensitizing beam). During the recording phase, the sensitizing beam brings electrons from the deeper traps to the shallower traps via the conduction band, providing enough electron concentration in the shallower traps for holographic recording. The hologram will be recorded in both the shallower and the deeper traps. The readout by the reference beam partially erases the hologram by exciting electrons from the shallower traps. Eventually, all electrons in the shallower traps will be transferred to the deeper traps. The remaining hologram in the deeper traps persists against further readout.

Three important performance measures in holographic storage are the dynamic range (*M/#*) (which relates to the available room for multiplexing different holograms), sensitivity (*S*) or recording speed (which indicates how fast we can record a hologram with a fixed intensity and a fixed material thickness), and persistence (which indicates

how many times we can read the stored information before data refreshing is required). The parameters that affect these measures in two-center recording are dopant concentrations, annealing (or oxidation/reduction) state, and recording and sensitizing intensities and wavelengths.

Several aspects of two-center recording were recently investigated [33-45]. Although most of the reported results were obtained using $LiNbO_3$:Fe:Mn crystals, other crystals like $LiNbO_3$:Cu:Ce [39], $LiNbO_3$:Tb:Fe [41] and $LiNbO_3$:Ce:Mn [42] were also investigated. However, there are a few efforts on the optimization of the method. Liu *et al.* presented the optimization for *M/#* in two-center recording with UV (the sensitizing beam) and red (the recording beams) and in $LiNbO_3$:Fe:Mn [36, 40]. They considered the variation of only one parameter at a time. They used approximate formulas for readout phase and the UV absorption was ignored in their analysis. The bulk photovoltaic effect of the Mn traps at the sensitizing wavelength was ignored. Also, the same recombination coefficient was used for electron recombination from the conduction band to either Mn or Fe traps. Adibi *et al.* preformed optimization on $LiNbO_3$:Fe:Mn with UV and red beams for sensitizing and recording, respectively [33]. They used a reliable set of material parameters and considered the absorption of the sensitizing beam in their simulations. Using the numeric method supported by experimental results, they investigated the variation of the *M/#* with only one parameter at a time while all other parameters were fixed. None of the previous efforts [33, 36, and 40] considered the optimization of the sensitivity or its dependence on the design parameters. The absorption of the recording beams was neglected in all the reports. A complete and accurate optimization of the two-center holographic recording is still needed to obtain the best performance.

In this Chapter we present the global optimization of both the *M/#* and sensitivity for two-center recording. Accurate analytic formulas as well as complete numerical simulations will be used. We will also consider the absorption inside the crystal for both recording and sensitizing beams. A main feature of this work is that the simultaneous variation of all design parameters is considered in the optimization process. The theoretical limit of the performance for two-center recording in $LiNbO_3$:Fe:Mn is also presented.

In Section 2.2 we discuss the two-center model we used for the analysis of two-center recording. Performance measures are evaluated in Section 2.3. The procedure for optimization and also the effect of the different design parameters on *M/#* and sensitivity are discussed in Section 2.4. Optimum results are presented in Section 2.5. Final conclusions are made in Section 2.6.

2.2 Two-center model

In general, the two-center holographic recording can be described by the modified Kukhtarev's equations for doubly doped crystals [33, 46]. The system of non-linear partial differential equations consists of two rate equations for shallower and deeper traps, the current continuity equation, the current equation, and the Poisson equation for the space-charge field. These equations are summarized in the following:

$$\frac{\partial N_D^-}{\partial t} = -\left(q_{D,L} s_{D,L} I_L + q_{D,H} s_{D,H} I_H\right) N_D^- + \gamma_D n\left(N_D - N_D^-\right), \tag{2.1}$$

$$\frac{\partial N_S^-}{\partial t} = -\left(q_{S,L} s_{S,L} I_L + q_{S,H} s_{S,H} I_H\right) N_S^- + \gamma_S n\left(N_S - N_S^-\right), \tag{2.2}$$

$$\frac{\partial j}{\partial x} = e\left(\frac{\partial N_D^-}{\partial t} + \frac{\partial N_S^-}{\partial t} + \frac{\partial n}{\partial t}\right), \tag{2.3}$$

$$j = e\mu nE + k_B T\mu \frac{\partial n}{\partial x} + \left(\kappa_{D,L} I_L + \kappa_{D,H} I_H\right) N_D^- + \left(\kappa_{S,L} I_L + \kappa_{S,H} I_H\right) N_S^-, \tag{2.4}$$

$$\frac{\partial E}{\partial x} = -\frac{e}{\varepsilon\varepsilon_0}\left(N_D^- + N_S^- + n - N_A\right), \tag{2.5}$$

with all variables and parameters defined in Table 2.1. By assuming the sinusoidal variation of the recording intensity, *i.e.*, $I_L = I_{L0}[1 + m\cos(Kx)]$, and considering the first two terms in the spatial Fourier series of all variables, *i.e.* $N_D = N_{D0}^- + N_{D1}^- \exp(-iKx)$, we can find two sets of zeroth and first order equations as the following [33]:

$$\begin{cases} \dfrac{dN_{D0}^-}{dt} = -\left(q_{D,L} s_{D,L} I_{L0} + q_{D,H} s_{D,H} I_H\right) N_{D0}^- + \gamma_D n_0 \left(N_D - N_{D0}^-\right) & (2.6) \\ \dfrac{dN_{S0}^-}{dt} = -\left(q_{S,L} s_{S,L} I_{L0} + q_{S,H} s_{S,H} I_H\right) N_{S0}^- + \gamma_S n_0 \left(N_S - N_{S0}^-\right) & (2.7) \\ 0 = N_{D0}^- + N_{S0}^- + n_0 - N_A & (2.8) \end{cases}$$

$$\begin{cases} \dfrac{dN_{D1}^{-}}{dt} = -\left(q_{D,L}s_{D,L}I_{L0} + q_{D,H}s_{D,H}I_H\right)N_{D1}^{-} - q_{D,L}s_{D,L}mI_{L0}N_{D0}^{-} \\ \qquad\qquad + \gamma_D n_1\left(N_D - N_{D0}^{-}\right) - \gamma_D n_0 N_{D1}^{-} \end{cases} \tag{2.9}$$

$$\begin{cases} \dfrac{dN_{S1}^{-}}{dt} = -\left(q_{S,L}s_{S,L}I_{L0} + q_{S,H}s_{S,H}I_H\right)N_{S1}^{-} - q_{S,L}s_{S,L}mI_{L0}N_{S0}^{-} \\ \qquad\qquad + \gamma_S n_1\left(N_S - N_{S0}^{-}\right) - \gamma_S n_0 N_{S1}^{-} \end{cases} \tag{2.10}$$

$$\frac{-iK}{e}j_1 = \left(\frac{dN_{D1}^{-}}{dt} + \frac{dN_{S1}^{-}}{dt} + \frac{dn_1}{dt}\right) \tag{2.11}$$

$$\begin{cases} j_1 = e\mu n_0 E_1 - ik_B T\mu K n_1 + \left(\kappa_{D,L}I_{L0} + \kappa_{D,H}I_H\right)N_{D1}^{-} + \kappa_{D,L}mI_{L0}N_{D0}^{-} \\ \qquad + \left(\kappa_{S,L}I_{L0} + \kappa_{S,H}I_H\right)N_{S1}^{-} + \kappa_{S,L}mI_{L0}N_{S0}^{-} \end{cases} \tag{2.12}$$

$$\frac{iK}{e}E_1 = \frac{N_{D1}^{-} + N_{S1}^{-} + n_1}{\varepsilon\varepsilon_0} \tag{2.13}$$

Note that in deriving these equations, the derivative with respect to space variable ($\partial/\partial x$) is replaces by $-iK$. Further assumptions can simplify these equations. The variation of the electron concentration in the conduction band (n) is assumed to be instantaneous compared to the variation of the other variables (adiabatic approximation). We also assume that the electron concentration in the conduction band is negligible compared to the electron concentrations in the shallower and the deeper traps. The DC electric field (E_0) has also been neglected in the above equations [33].

The above eight equations should be solved simultaneously to find the space-charge field in the crystal. The space-charge field is then used to calculate hologram strength, *M/#*, and sensitivity. The hologram strength is defined by $A = \pi n^3 r E_1 d \,/\, [2\lambda_r \cos(\Theta)]$, where all the parameters are defined in Table 2.1. The relation between diffraction

efficiency (η) and hologram strength is given by Kogelnik's formula [9] [*i.e.* $\eta = \sin^2(A)$].

Table 2.1. Description of the parameters used in the equations.

Notation	Description
$q_{X,Y}\, s_{X,Y}$	Absorption cross section for absorbing a photon of beam Y and exciting an electron from trap X
$\kappa_{X,Y}\, s_{X,Y}$	Bulk photovoltaic coefficient of trap X at the wavelength of beam Y
$N^{-}_{X,l}$	Concentration of ionized dopant X
N_X	Total concentration of a dopant X
N_A	Concentration of positive compensator charge
n_l	Electron concentration
I_Y	Total intensity of beam Y
E	Electron charge
j_l	Current density
k_B	Boltzmann constant
γ_X	Recombination rate of the electrons to trap X
ρ	Total charge density
$\boldsymbol{K}$	Magnitude of grating vector
μ	Electron mobility in the conduction band
m	Modulation depth
T	Crystal temperature
t	Time
$\varepsilon\varepsilon_0$	Permittivity of the crystal
λ_r	Recording wavelength
Θ	Half the angle between the recording beams in the medium
n	Refractive index
R	Electro-optic coefficient
d	Crystal thickness

Note l is an integer and can be 1 referring to the first order terms and 0 referring to the zeroth order terms.
X, Y are variables and can get different indices as following:
X=S: Shallower traps
X=D: Deeper traps
Y=L: Lower frequency (longer wavelength) beam
Y=H: Higher frequency (shorter wavelength) beam

2.3 Derivation of the performance measures

In general, two-center holographic recording consists of three phases: sensitizing, recording, and readout. For a complete two-center recording process, the crystal is first sensitized with the sensitizing beam. In the recording phase the hologram is recorded by the use of signal and reference beams (two coherent longer wavelength beams) with the sensitizing beam (a shorter wavelength beam) illuminating the crystal. During the readout phase, the reference beam reads the hologram, and no other beam is present.

There are three measures that are used widely to describe the holographic recording process. The dynamic range, or the *M/#*, is a measure of the total refractive index modulation that can be achieved for multiplexed holograms. If M holograms are multiplexed appropriately [47], the diffraction efficiency of each hologram is $\eta=[(M/\#)/M]^2$. For recording weak holograms, an approximate measure for the *M/#* is the square root of the saturation diffraction efficiency [33]. The sensitivity (*S*) is a measure of the speed of recording and is defined as:

$$S = \frac{1}{I_L d} \times \left. \frac{d\sqrt{\eta}}{dt} \right|_{t=0}, \tag{2.14}$$

where I_L and d represent the total recording intensity and the crystal thickness, respectively. The persistence, or *R/#*, is a measure of the number of times a hologram can be read with acceptable diffraction efficiency [48]. During the readout in two-center recording, the hologram strength drops rapidly and then saturates at a nearly fixed value (Figure 2.1). We refer to this value as the final hologram strength (A_F). The ratio of A_F to

the saturation value of the hologram strength during recording (A_0) is denoted by β in this article. In the absence of an external electric field, β is between zero and one.

The definition of common performance measures for normal (single-center) holographic recording should be slightly modified to describe the two-center holographic recording. For example *M/#* and *S* calculated using recording dynamics should be multiplied by β for the two-center recording to account for the partial erasure during readout.

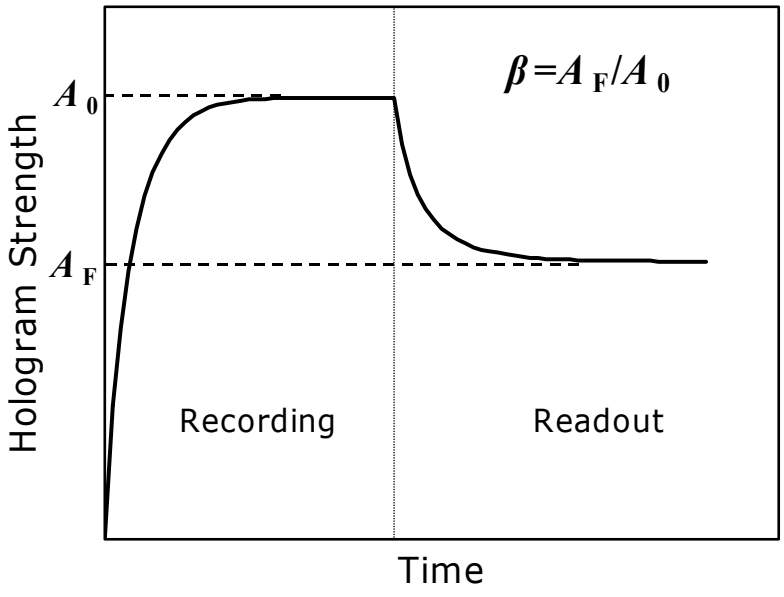

Figure 2.1. A typical recording readout curve for two-center holographic recording. During the readout, the hologram is partially erased. The remaining hologram persists against further readout.

2.3.1 Analytic solution for the recording phase

In the recording phase, we should solve the differential Equations (2.6)-(2.13) while the sensitizing and the recording intensities are not zero. The *M/#* is proportional to the saturation space-charge field, and the sensitivity is proportional to the slope of the space-charge field at the beginning of recording. Therefore, if we find a complete solution for

the variation of the space-charge field with time, we can easily calculate *M/#* and *S*. This solution can be found by approximating the recording curve by a mono-exponential function of time. Therefore, the space-charge field is expressed by

$$E_1 \approx E_{SC}\left(1-\exp(-t/\tau_r)\right), \tag{2.15}$$

where E_{SC} (saturation space-charge field during recording) and τ_r (recording time constant) are derived in Appendix A (Equations (A1) and (A10), respectively). Knowing E_{SC}, we can find *M/#* by

$$M\# = \frac{\pi n^3 r\, d}{2\lambda_r \cos(\Theta)} E_{SC}\beta\,, \tag{2.16}$$

where all the parameters are defined in Table 2.1. The value of β can be found from the analysis of readout phase (Section 2.3.2). A typical recording curve for hologram strength obtained from the analytic formula of space-charge field and the accurate curve resulting from the numerical simulation for $LiNbO_3$:Fe:Mn with 365 nm sensitizing wavelength and 633 nm recording wavelength are shown in Figure 2.2. In the case, when the Fe concentration is much larger than the Mn concentration and the sensitizing intensity is one order of magnitude less than the recording intensities, the expression for E_{SC} and τ_r can be simplified to Equations (A13) and (A15), respectively (shown bellow for simplicity).

$$E_{SC} \approx \frac{\kappa_{Fe,R} N_{Fe0}^{-}}{e\mu n_0} m I_{R0} \times CF\,,$$

$$\tau_r \approx \left(\frac{\varepsilon\varepsilon_0}{e\mu n_0}\right) + \left[\frac{\gamma_{Fe}\left(N_{Fe} - N_{Fe0}^{-}\right) + \gamma_{Mn}\left(N_{Mn} - N_{Mn0}^{-}\right)}{H}\right].$$

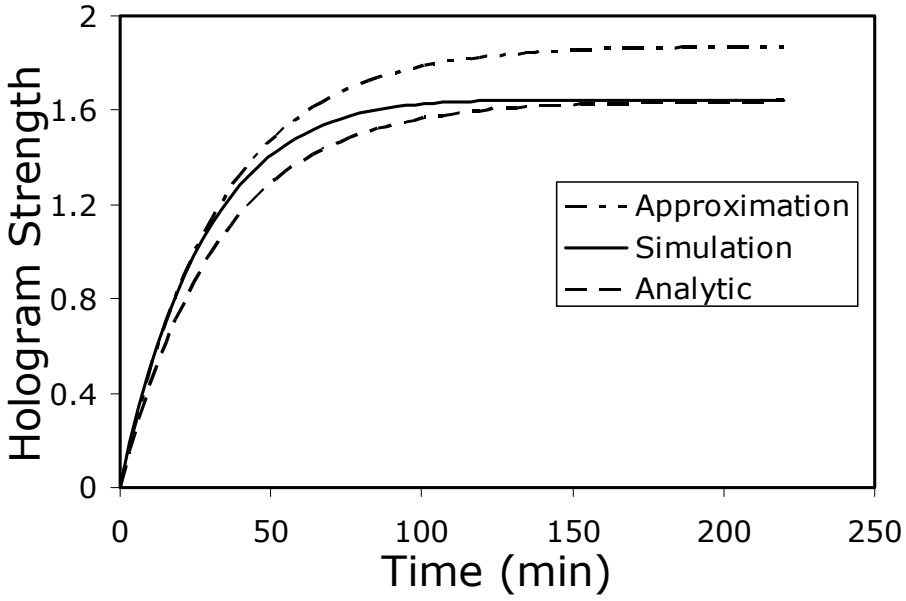

Figure 2.2. Hologram strength versus time for a typical recording in a 1 mm thick $LiNbO_3$ crystal doped with 0.15 wt. % Fe_2O_3 and 0.002 wt. % MnO using transmission geometry with Θ=27°. Initially, 80% of the Mn traps are filled with the electrons. Sensitizing and recording intensities are 20 mW/cm^2 and 250 mW/cm^2, respectively. The absorption of both recording and sensitizing beams is neglected in this simulation. The polarization of the recording beams is ordinary.

The recording curve obtained from this approximation is also shown in Figure 2.2. The expression for the saturation field (E_{CS}) is the same as the approximate expression for saturation field in the normal holographic recording [16, 49] in singly doped $LiNbO_3$ except that a correction factor (*CF*) is multiplied to include the effect of two-center recording. The recording time constant (τ_r) given in Equation (A15) is the sum of the time constants for the normal recording with an additional term because of two-center effects. Since the additional term is always positive, it is concluded that the time constant for two-center recording is always larger than that for normal recording under similar conditions.

A straightforward method to find sensitivity (S) is to calculate the initial recording slope using the approximate formula for the hologram strength as a function of time. But, as is seen in Figure 2.3, this is not a good approximation for the sensitivity in two-center recording. The reason is that the actual two-center recording dynamics is not optimally represented by a mono-exponential function of time. Therefore, we should use the initial differential equations and find the derivative of the space-charge field at the beginning of the recording (t=0). Finding the derivative with respect to time of both sides of Equation (2.13), then using Equations (2.11) and (2.12) and also noting that N_{Fe1}^{-}, N_{Mn1}^{-}, n_1, and E_{sc} are zero at $t=0$, we find:

$$S = \frac{1}{\varepsilon\varepsilon_0}\frac{\pi n^3 r}{2\lambda_r \cos(\Theta)}\left(\kappa_{D,L}N_{D0}^{-}\Big|_{t=0} + \kappa_{S,L}N_{S0}^{-}\Big|_{t=0}\right)m\beta\,, \tag{2.17}$$

where N_{D0}^{-} and N_{S0}^{-} are average electron concentrations in deeper and shallower traps, respectively (and are derived in Appendix A), and the other parameters are defined in Table 2.1. Again, β will be found in Section 2.3.2. Note that N_{S0}^{-} and N_{D0}^{-} are at steady-state when the sensitizing beam and recording beams are present. The intensities of the beams must be equal to the average sensitizing and recording intensities during the recording phase, respectively. In hologram multiplexing, each hologram (except the first hologram) is recorded after the material is illuminated long enough by sensitizing and recording beams (during the recording of previous holograms) to reach the steady-state values of N_{S0}^{-} and N_{D0}^{-}. In the definition of sensitivity in two-center recording, β is used to account for the partial erasure of the hologram at the beginning of readout. The sensitivity calculated from Equation (2.16) agrees very well with the numerical analysis.

Since the values of N_{D0}^{-} and N_{S0}^{-} are almost independent of the bulk photovoltaic coefficients of the shallower and the deeper traps, it is seen that having dopants with higher photovoltaic constants results in higher sensitivity. It is exactly in accordance with the experimental results reported in [37]. Considering the expressions for *M/#* and *S* [Equations (2.16) and (2.17)] we have all the analytic results for the recording phase

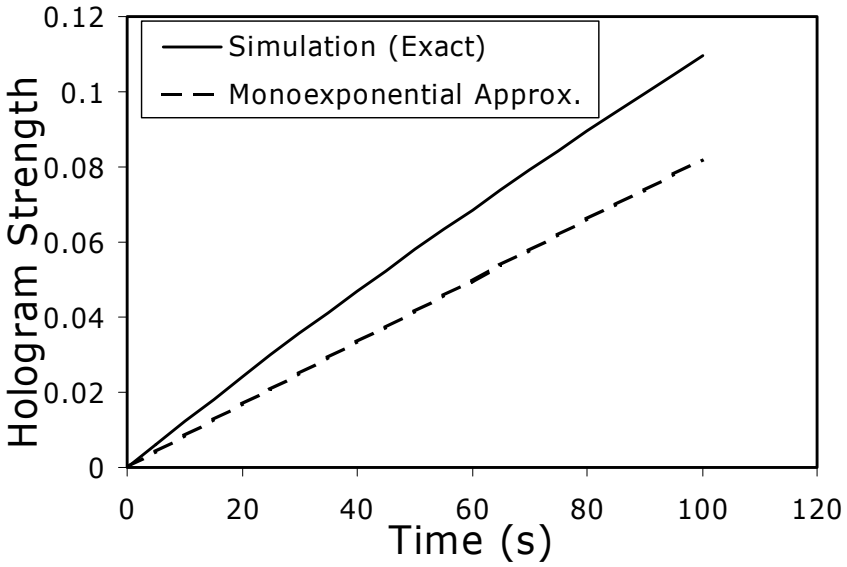

Figure 2.3. Hologram strength at the beginning of recording used to show the difference between mono exponential approximation and the accurate numerical solution. Sensitivity, by definition, is the initial slope of each curve. The parameters of recording are the same as those in the caption of Figure 2.2.

2.3.2 Analysis of the readout phase

During readout, only the reference beam is present. The reference beam excites the electrons from the shallower traps to the conduction band. All electrons will be eventually re-trapped in the deeper traps since the sensitizing beam is not present during readout, and the reading beam cannot excite electrons from the deeper traps to the conduction band. Therefore, the final persistent hologram will be stored in the deeper

traps. Finding an analytic solution for this phase is very difficult since the average electron concentrations in the two traps (N_{D0}^{-} and N_{S0}^{-}) are considerably varying with time. Numerical analysis for this phase shows that the intensity of the reference beam during readout has no effect on the final value of the space-charge field or hologram strength (Figure 2.4). Note that modifying the dynamics of readout intensity modifies the dynamics of readout, but the final hologram strength (and therefore, β) remains the same. Since the performance measures depend on β and not on the readout dynamics, we can choose an appropriate variation of the readout intensity with time to simplify the calculation of β (and other performance measures). The detail of our method is summarized in Appendix B. The result is a second order differential equation for the space-charge field:

$$P(W)\frac{d^2E_1}{dW^2} + Q(W)\frac{dE_1}{dW} + R(W)E_1 = 0, \tag{2.18}$$

where

$$W = N_D - N_A + N_{S0}^{-}(t), \tag{2.19}$$

and $P(W)$, $Q(W)$ and $R(W)$ are given in Appendix B for the case of $LiNbO_3$:Fe:Mn crystals. The final value of the space-charge field is found by solving Equation (2.18) at $W=N_D-N_A$ (or $N_{S0}^{-}=0$), which corresponds to the case that all the shallower traps are empty. Although this equation must be solved numerically, it is much easier and faster to solve this equation rather than a set of five nonlinear differential equations that provides almost the same result for the final space-charge field. It is also easier to find the final value of E_1 ($E_{1,Final}$) since this value is calculated at finite W ($W=N_D-N_A$) instead of at

$t=\infty$. This reduces the computation time since the numerical solution at infinity is not needed. After finding the final value of the space-charge field, we can calculate $\beta = E_{1,Final}/E_{SC}$, which will be used in finding the overall $M/\#$ and S [Equations (2.16) and (2.17)].

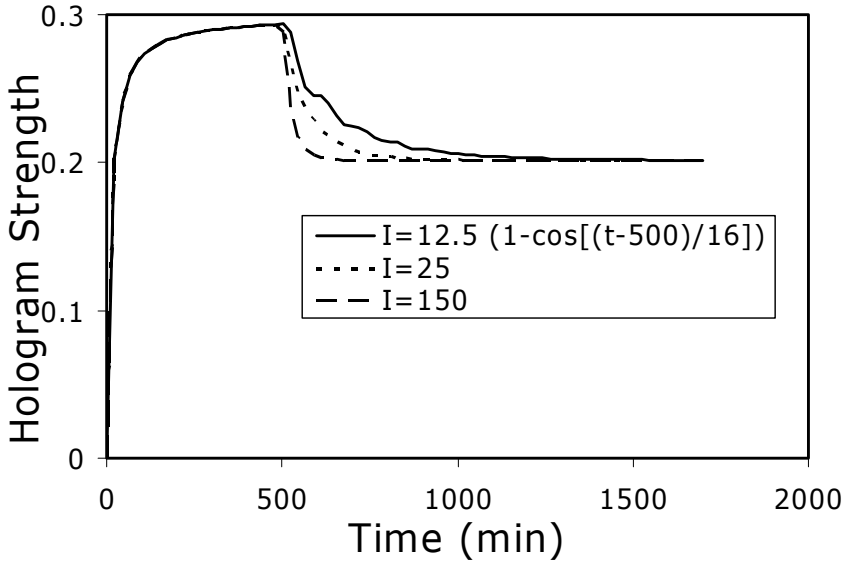

Figure 2.4. Effect of readout intensity on the hologram strength during the readout phase. The hologram is recorded in a 1 mm thick $LiNbO_3$ crystal doped with 0.075 wt. % Fe_2O_3 and 0.01 wt. % MnO. Initially, 90% of the Mn traps are filled with the electrons. Sensitizing and recording intensities are 20 mW/cm^2 and 500 mW/cm^2, respectively. Recording dynamics is the same in all cases. The three curves correspond to the readout intensities of 150 mW/cm^2 (constant with time), 25 mW/cm^2 (constant with time), and 12.5×{1-cos[(*t*-500)/16]} mW/cm^2 where *t* represents time in minutes.

2.3.3 Effect of the absorption of sensitizing and recording beams

In most applications, the crystal used for two-center recording exhibits a high absorption at the sensitizing wavelength. The absorption is stronger when the energy of the sensitizing photons is close to the energy band gap of the crystal or when the total electron concentration in the traps is large. In such cases, we should consider the absorption of the sensitizing beam as it goes through the crystal. Furthermore, when the

electron concentration in the shallower traps becomes high during recording we should also consider the absorption of the recording beam inside the crystal. To include these absorptions in the calculation of *M/#*, we first divide the crystal into several thin slices of thickness Δz (typically 50-100 slices for a 1 mm thick crystal). Assuming constant sensitizing and recording intensities within each slice, we solve for the $(M/\#)_i$ in each slice Δz. Then, we calculate the total *M/#* using the following sum:

$$(M/\#)_{total} = \sum_{all\ i} (M/\#)_i \ , \tag{2.20}$$

Equation (2.20) simply states that the total *M/#* of the crystal is the sum of the *M/#*'s of the thin portions of the crystal with different sensitizing and recording beams. The idea of analyzing the thin slices is also applied to find the sensitivity when the absorption of both sensitizing and recording intensities are taking into account. Therefore, the total sensitivity is found using

$$S_{total} = \frac{\Delta z}{d} \sum_{all\ i} S_i \ . \tag{2.21}$$

2.4 Optimization procedure

In this section we consider the role of each design parameter in the variation of *M/#* and *S*. In the simulations, we use congruently melting $LiNbO_3$:Fe:Mn with different doping concentrations as the recording material. The sensitizing beam is a 365 nm UV beam with an intensity-absorption coefficient in the order of 9 mm^{-1} [33]. Two coherent recording beams with equal intensities are used at 633 nm (red) wavelength. These

wavelengths are chosen since a reliable set of all material parameters exists for $LiNbO_3$:Fe:Mn at 365 nm and 633 nm [33]. The hologram is recorded in a 1 mm thick sample using symmetric transmission geometry. The angle between two recording beams is 43.5º. We assume ordinary polarization for recording and reading beams. The resulting grating vector is parallel to the **c**-axis of the crystal.

Since the numerical solution for the readout phase is a time consuming process, we consider the practical range for the design parameters and make a table of β for each set of parameters. Using the expressions found in the previous section for the recording phase [*i.e.* Equations (2.16), (2.17) and (A1)] and also the complete table of β, we consider the behavior of the holographic measures as the design parameters vary. The variation of *M/#* with single design parameters (while other parameters are fixed at non-optimal values) have been reported previously [33, 36]. Here we show the variation of *M/#* with individual design parameters around its global optimum. We also explain these variations based on some simple approximate formulas. To the best of our knowledge, the variation of *S* with the design parameters around its global optimum is presented here for the first time. To study the variation of *M/#* (or *S*) with a single design parameter, we fix all other design parameters at their global optimum values which result in a global maximum for *M/#* (or *S*). The details of the global optimization are discussed in Section 2.5.

2.4.1 Role of Fe concentration

In normal recording in a singly-doped $LiNbO_3$ crystal, both *M/#* and sensitivity grow with increasing trap concentration. In two-center recording, also, both *M/#* and sensitivity

increase with increasing shallower trap concentration (Fe concentration). Figure 2.5 shows the variation of *M/#* and sensitivity with Fe concentration for a 1 mm thick $LiNbO_3$:Fe:Mn crystal. Figure 2.5 shows that to achieve the maximum *M/#* and sensitivity, we must use the highest possible Fe concentration. We know that the maximum value for Fe concentration in normal recording in $LiNbO_3$:Fe is about 0.05 wt. % [50]. For higher Fe concentrations, electron tunneling between iron traps prevents recording stronger holograms [50]. However, for two-center recording, we choose the maximum concentration of 0.15 wt. % Fe_2O_3 ($N_{Fe}=5\times10^{25}$ m^{-3}). In normal recording this concentration has the potential to show the tunneling effect, but in a doubly doped crystal we accept such a concentration for two reasons. First, the final hologram will be stored in the Mn traps, and all Fe traps will eventually be empty. Therefore, electron tunneling between Fe traps is not important. The second reason is that the tunneling between Fe traps during recording and readout tends to increase the hologram strength. The total space-charge field is due to two strong and almost 180° out of phase charge patterns in Fe and Mn traps [33]. Erasing one of the charge patterns by tunneling, results in increasing the total electric field. Such an increase in the space-charge field will increase the barrier against tunneling to avoid further increase in the field. Therefore, the Fe concentration is not limited by tunneling in two-center recording. Knowing that electron tunneling between Mn traps is harder than that between Fe traps [51], we assume $N_{Mn}=3.7\times10^{25}$ m^{-3} (which approximately corresponds to 0.1 wt. % MnO) as the maximum practical Mn concentration.

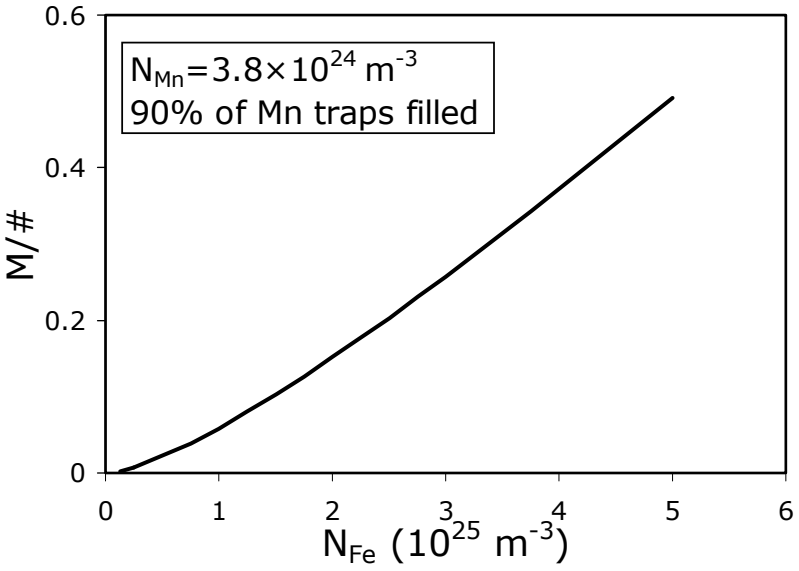

(a)

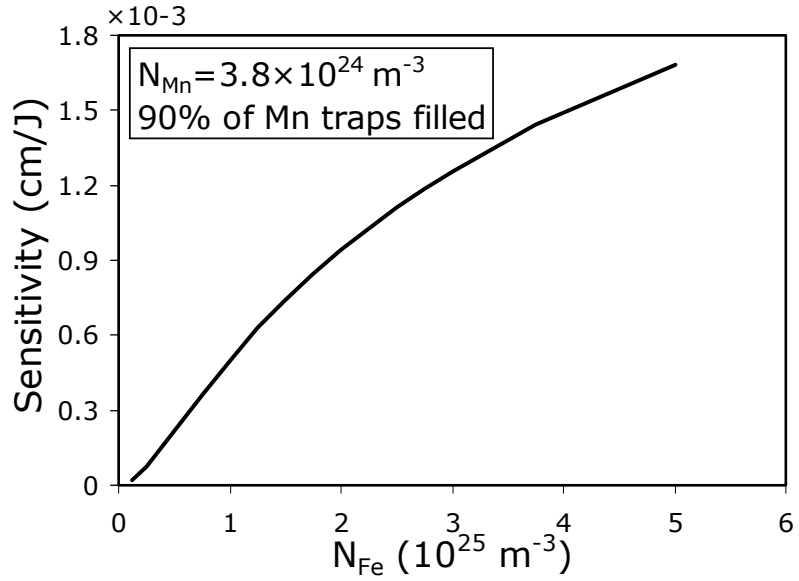

(b)

Figure 2.5. Variation of (a) *M/#* and (b) sensitivity with Fe concentration in a 1 mm thick $LiNbO_3$:Fe:Mn crystal. The Mn concentration is fixed at 3.8×10^{24} m^{-3}. Initially, 90% of the Mn traps are filled with the electrons. 365 nm (UV) and 633 nm (red) are sensitizing and recording wavelengths, respectively. The intensity ratio (I_R/I_{UV}) is 25 for both cases.

2.4.2 Role of sensitizing and recording intensities

Careful consideration of the expressions for the *M/#* and sensitivity in the recording phase shows that both of them are functions of intensity ratio (I_R/I_{UV}) and not the absolute intensities [Equations (2.16) and (2.17)]. Also noting that β is independent of the intensities yields that the *M/#* and sensitivity for two-center recording depend only on the intensity ratio (I_R/I_{UV}) and not on the absolute intensities. The dependence of the *M/#* on the intensity ratio was theoretically proposed and experimentally shown in [33], but there has been no previous report on the dependence of sensitivity on the intensity ratio. To our best knowledge, this is the first time the dependence of the sensitivity on the intensity ratio is reported. Figure 2.6 shows this dependency more clearly. To explain this variation of *S*, we can use the energy band diagram in Figure 2.7. Sensitivity depends mainly on the bulk photovoltaic current density in the conduction band, which is proportional to average electron concentration in the Fe traps (N_{Fe0}^{-}). This concentration depends on the excitation and recombination rates shown in Figure 2.7. Excitation of the electrons from Fe traps tends to reduce N_{Fe0}^{-} while excitation from the Mn traps tends to populate Fe traps (via the conduction band) and increase N_{Fe0}^{-}. When we increase both intensities by the same factor (so that I_R/I_{UV} is fixed), all excitation rates (proportional to light intensities) are increased in the same way. However, the relative strengths of these excitations remain intact. Thus, the average electron concentrations in both Fe and Mn traps depend on the intensity ratio only and not on the absolute intensities. This intuitive point can be theoretically verified by Equations (A6) and (A7) derived in Appendix A.

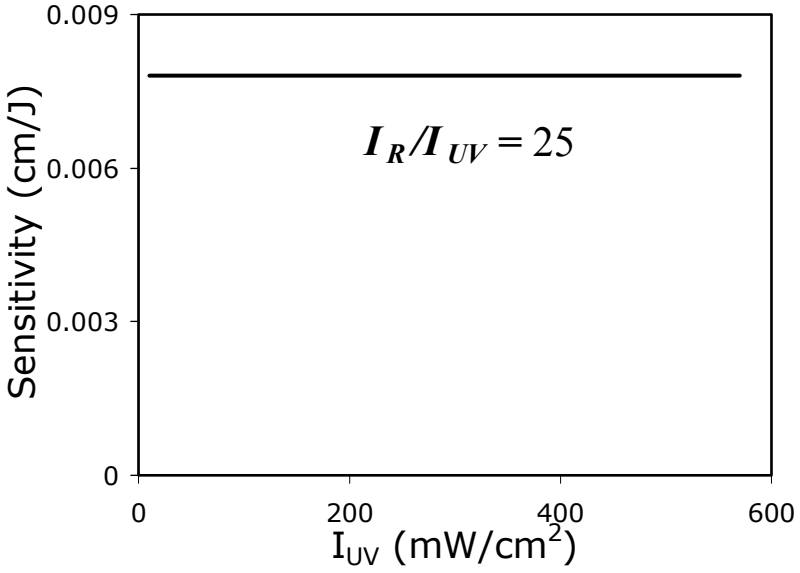

Figure 2.6. Variation of sensitivity with sensitizing intensity for a 1 mm thick $LiNbO_3$:Fe:Mn crystal doped with 0.075 wt. % Fe_2O_3 and 0.01 wt. % MnO. Initially, 90% of the Mn traps are filled with electrons. 365 nm (UV) and 633 nm (red) are sensitizing and recording wavelengths, respectively. The intensity ratio is fixed and both the sensitizing and recording intensities are varying.

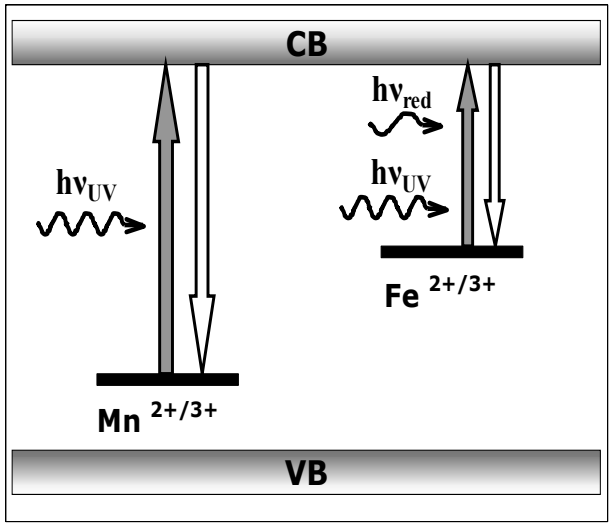

Figure 2.7. Energy band diagram for a typical $LiNbO_3$ crystal doped with Fe and Mn. CB and VB are conduction band and valence band, respectively.

The dependence of both *M/#* and *S* on the intensity ratio reduces one independent parameter (the design parameter is I_R/I_{UV} instead of both I_R and I_{UV}). With N_{Fe} already

selected, three remaining parameters for optimization are Mn concentration (N_{Mn}), oxidization/reduction state (N_A) and the intensity ratio (I_R/I_{UV}).

2.4.3 Role of Mn concentration

Figure 2.8 shows the variation of *M/#* and sensitivity with the Mn concentration while Fe concentration and intensity ratio are fixed. For the calculation of *M/#* we assume 85% of the Mn traps are initially filled with electrons, since the *M/#* reaches its global maximum when $N_A = 0.85\ N_{Mn}$. On the other hand, the maximum of *S* occurs when about 90% of the Mn traps are initially filled with electrons. As Figure 2.8 shows, *M/#* reaches the global maximum when the Mn concentration is much lower than the Fe concentration, and then decreases as the Mn concentration increases further. On the other hand, *S* increases by increasing Mn concentration in the practical range of concentrations used for the simulations. The results shown in Figure 2.8 can be understood by using the formulas (2.16) and (2.17).

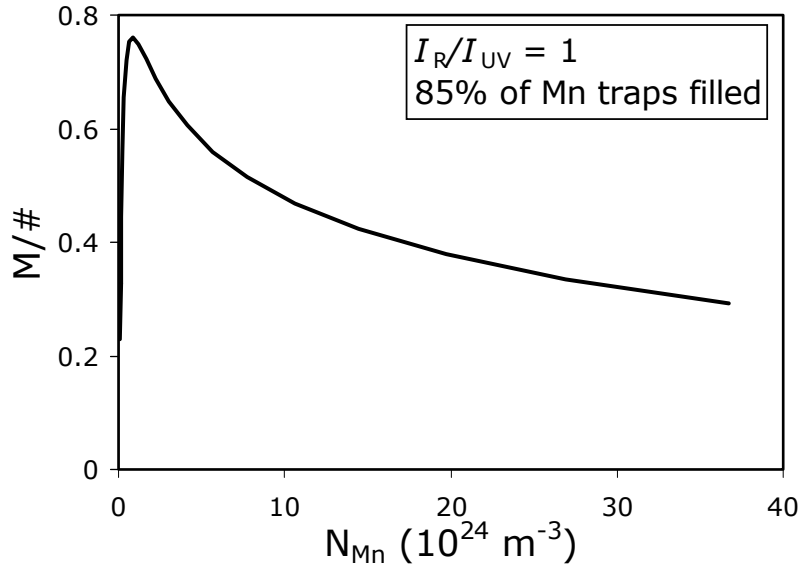

(a)

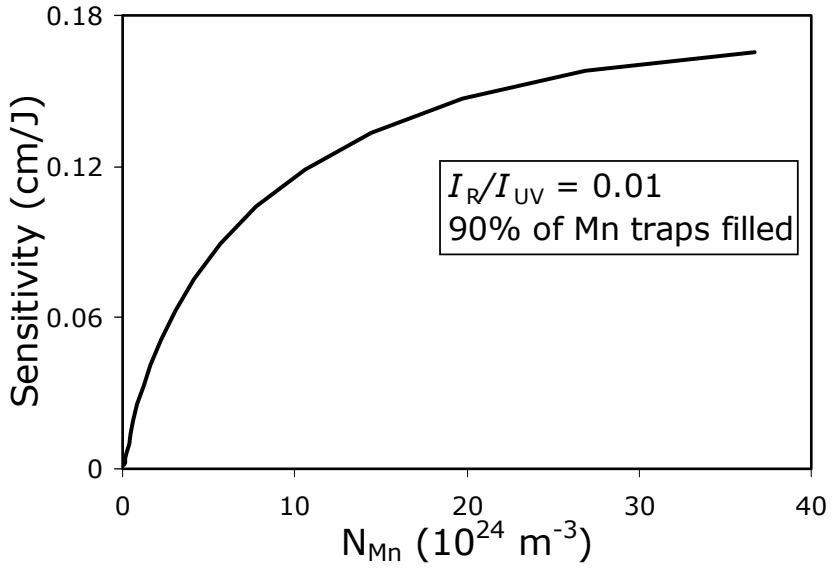

(b)

Figure 2.8. Variation of (a) *M/#* and (b) sensitivity with Mn concentration for a 1 mm thick $LiNbO_3$:Fe:Mn crystal doped with 0.15 wt. % Fe_2O_3. 365 nm (UV) and 633 nm (red) are sensitizing and recording wavelengths, respectively. For *M/#* in (a) the intensity ratio (I_R/I_{UV}) is 1 and initially 85% of the Mn traps are filled with electrons. For sensitivity in (b) the intensity ratio (I_R/I_{UV}) is 0.01 and initially 90% of the Mn traps are filled with electrons. These parameter values are selected to include the optimum *M/#* and *S* in the figures.

With $N_{Mn} \approx 0$ no hologram can be recorded since all Fe traps are initially empty. Therefore, by increasing N_{Mn}, hologram strength (and *M/#*) is quickly increased. For small N_{Mn}, space-charge limitation occurs and the approximate formulas are not useful. At larger values of N_{Mn}, we can use approximate Equation (A13) for E_{SC} to substitute in Equation (2.16) for *M/#*. Therefore:

$$M/\# \propto \frac{N_{Fe0}^{-}}{n_0} CF \tag{2.22}$$

where *CF* varies slowly with N_{Mn}. Increasing N_{Mn} results in increasing both N_{Fe0}^{-} and n_0. However, the increase in n_0 is stronger than that in N_{Fe0}^{-}, for values of N_{Mn} above the optimal value. Therefore *M/#* decreases as N_{Mn} is increased. The actual position of the peak depends strongly on the intensity ratio.

For sensitivity, since the photovoltaic constant of the Mn traps at the recording wavelength ($\kappa_{D,L}$) is negligible, we can assume that $S \propto N_{S0}^{-} = N_{Fe0}^{-}$. By increasing the Mn concentration (with 90% of them filled), we increase the excitation rate of electrons from the Mn traps to the conduction band (proportional to N_{Mn}). Increasing the concentration of the Mn traps will increase the recombination rate of electrons from the conduction band (proportional to N_{Mn}; note that 10% of the Mn traps are empty). The combination of these two competing effects results in variation of *S* with N_{Mn} as:

$$S \propto N_{Fe0}^{-} \propto \frac{N_{Mn}}{N_{Mn} + \xi}\ , \tag{2.23}$$

where ξ is a constant representing the recombination rate for the Fe traps. The plot of Equation (2.23) with N_{Mn} is the same as Figure 2.8(b). It is obvious from Figure 2.8 that

the maximum values for *M/#* and *S* cannot be achieved simultaneously. Therefore, There is a trade-off between *M/#* and *S*.

2.4.4 Role of oxidization/reduction state

The variations of *M/#* and sensitivity with the initial electron concentration in the Mn traps (*i.e.* N_A) are shown in Figure 2.9, while other parameters are fixed. The initial electron concentration in Mn traps (N_A) can be varied by annealing (or oxidation/reduction). Figure 2.9 shows that both *M/#* and *S* reach their maximum values when $N_A \approx (0.8\text{-}0.9)\times N_{Mn}$. The optimum values of N_A for maximizing *M/#* and *S* depend on the actual doping concentrations and on the intensity ratio. With $N_A=0$, all traps (Mn and Fe) are empty and no hologram can be recorded. With $N_A= N_{Mn}$, all the Mn traps are initially filled with electrons. Although a strong hologram can be recorded in this case, readout process is destructive (*i.e.* β=0). All electrons will eventually be trapped in the Mn sites with no empty Mn traps remaining to hold the final hologram [34]. Therefore, there must be an optimum value of N_A at $0<N_A< N_{Mn}$ that results in maximum *M/#* or maximum *S*. The maximum for *M/#* and *S* usually do not occur at the same N_A, but the optimum values of N_A in the two cases are close.

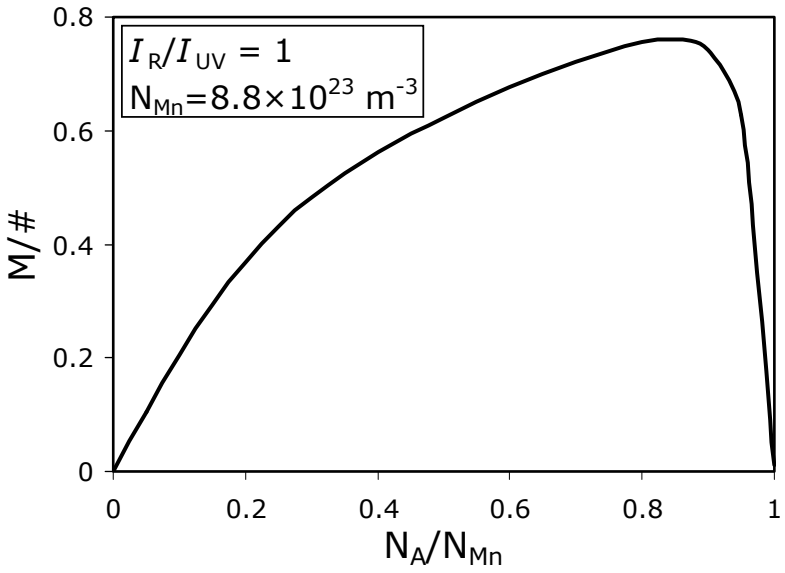

(a)

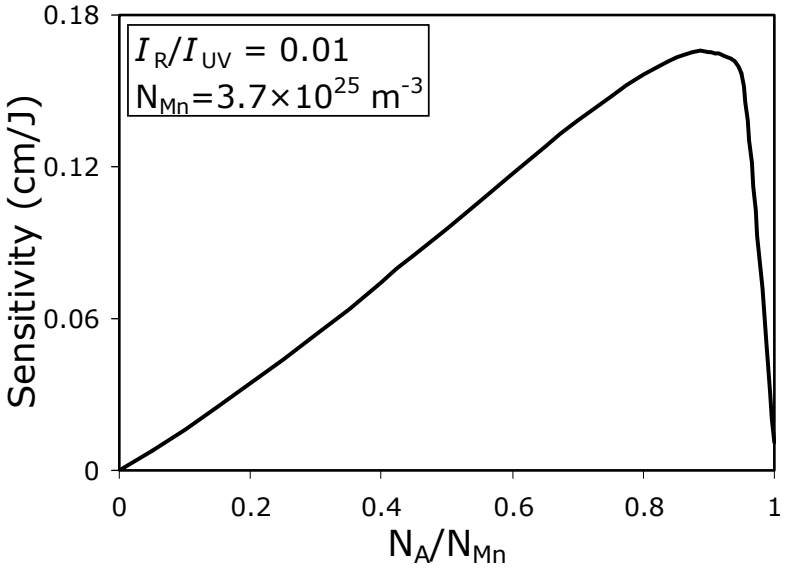

(b)

Figure 2.9. Variation of (a) M/# and (b) sensitivity with initial oxidization/reduction state for a 1 mm thick $LiNbO_3$:Fe:Mn crystal doped with 0.15 wt. % Fe_2O_3. 365 nm (UV) and 633 nm (red) are sensitizing and recording wavelengths, respectively. For M/# in (a) the intensity ratio and the Mn concentration are 1 and 8.8×10^{23} m^{-3}, respectively. For sensitivity in (b) the intensity ratio and the Mn concentration are 0.01 and 3.7×10^{25} m^{-3}, respectively. The parameter values are chosen to include the optimum M/# and S in the figures.

2.4.5 Role of intensity ratio (I_R/I_{UV})

For any crystal, there is an optimum value for the intensity ratio (I_R/I_{UV}) that results in the best performance. A typical variation of *M/#* and *S* versus the intensity ratio is shown in Figure 2.10. Figure 2.10 shows that the maximum sensitivity can be achieved with high sensitizing intensity, while the maximum *M/#* is obtained when the sensitizing and recording intensities are of the same order. Note that N_{Mn} and N_A/N_{Mn} in Figure 2.10(a) and Figure 2.10(b) are chosen to result in the global optima. Therefore, the global maxima of *M/#* and sensitivity occur at different values of the intensity ratio. The variation of *M/#* with intensity ratio, when other parameters are fixed at non-optimal values, has been already reported and explained [36, 33]. We can simply understand this variation by using Equation (2.22). Both N_{Fe0}^{-} and n_0 depend on I_R and I_{UV}. Too strong I_{UV} results in an acceptable N_{Fe0}^{-} (I_{UV} excites electrons from both Fe and Mn) and a very strong n_0 ($n_0 \propto I_{UV}$). Too weak I_{UV} (compared to I_R) cannot populate the Fe traps since strong I_R tends to depopulate them. Therefore, *M/#* is maximum at an intermediate I_R/I_{UV}. The actual optimum intensity ratio depends on N_{Fe}, N_{Mn}, and N_A. The variation of *S* with the intensity ratio [Figure 2.10(b)] reported here completely agrees with the experimental results of the variation of sensitivity with sensitizing and recording intensities reported in Ref. [52] for $LiNbO_3$:Cu:Ce crystals. It can be easily understood by using Equation (2.17) (*i.e.*, $S \propto N_{Fe0}^{-}$). The role of I_{UV} is to excite electrons from the Mn traps (and from the Fe traps). Its overall role is to populate the Fe traps to some degree. On the other hand, the role of I_R is only to depopulate the Fe traps. Therefore, N_{Fe0}^{-} becomes larger at smaller

I_R/I_{UV} and larger N_{Fe0}^{-} results in larger *S*. So, maximum *S* is obtained at small I_R/I_{UV} (or large I_{UV}/I_R).

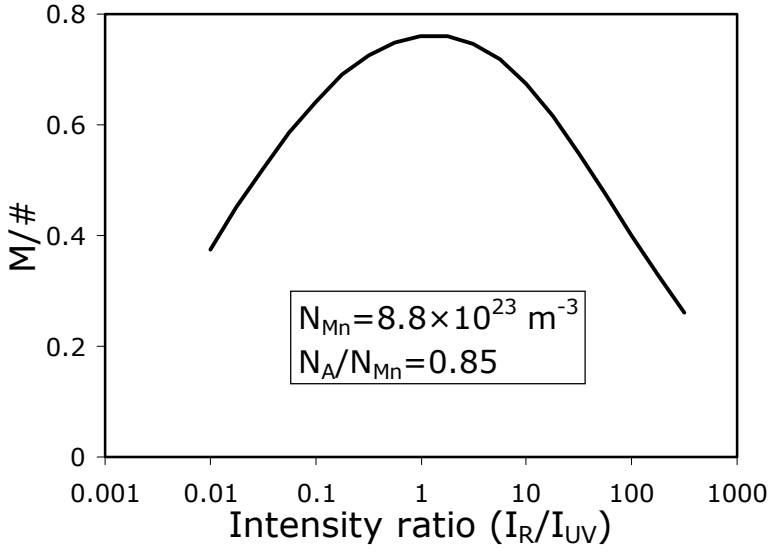

(a)

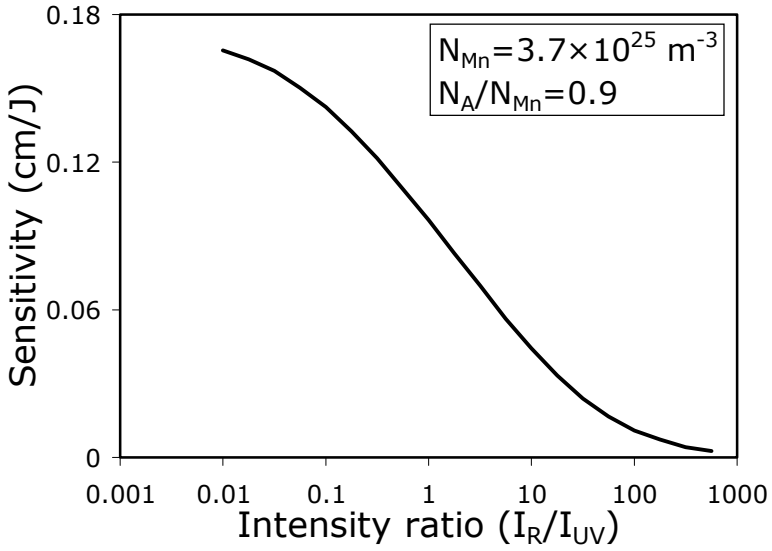

(b)

Figure 2.10. Variation of (a) *M/#* and (b) sensitivity with intensity ratio for a 1 mm thick $LiNbO_3$:Fe:Mn crystal doped with 0.15 wt. % Fe_2O_3. 365 nm (UV) and 633 nm (red) are sensitizing and recording wavelengths, respectively. For *M/#* in (a) the Mn concentration and acceptor concentration (N_A) are 8.8×10^{23} m^{-3} and 7.5×10^{23} m^{-3}, respectively. For sensitivity in (b) the Mn concentration and acceptor concentration (N_A) are 3.7×10^{25} m^{-3} and 3.3×10^{25} m^{-3}, respectively. The parameter values are chosen to include the optimum *M/#* and *S* in the figures.

2.5 Global optima

In Section 2.4 we observed the effect of the variation of the individual design parameters on *M/#* and *S*. The optimum obtained for each individual parameter (*i.e.*, N_A) depends on the other design parameters. In general, the treatment of Section 2.4 cannot yield the set of parameters for the global maximum *M/#* (or maximum *S*). A global optimization scheme is required in which all design parameters are allowed to vary simultaneously.

In this optimization procedure, we use the accurate analytic formulas we derived for the recording phase [Equations (2.16), (2.17) and (A1)] along with the table of β versus the design parameters calculated by numerical simulation of the readout phase. The absorption of sensitizing and recording beams is considered in our calculation as explained in Section 2.3.3. We let all the parameters (N_{Mn}, N_A and I_R/I_{UV}) vary and find the maximum *M/#* and *S*. The value of N_{Fe} is chosen at $N_{Fe}=5\times10^{25}$ m^{-3} which corresponds to 0.15 wt. % of Fe_2O_3.

In these simulations we used a 1 mm thick $LiNbO_3$:Fe:Mn crystal. Sensitization and recording wavelengths are 365 nm and 633 nm, respectively. Ordinary polarization is used for recording and reading beams. We also calculated the optima for the more recently proposed set of wavelengths (404 nm for sensitization and 514 nm for recording) [37]. For these wavelengths, the set of material parameters can be estimated from the literature [33, 53-54]. The estimated parameters we used are summarized in Table 2.2.

Table 2.3 summarizes the optimum design parameters needed for maximizing *M/#* and *S*. It is obvious that the sensitivity and *M/#* reach their maxima at different values of the design parameters, so there is always a trade-off in finding the best set of parameters.

Table 2.2. Crystal parameters for $LiNbO_3$ at 514 nm and 404 nm wavelengths.

Notation	Description	Value
$q_{Fe,404}\, s_{Fe,404}$ (m^2/J)	Absorption cross section for absorbing a photon at wavelength 404 and exciting an electron from Fe traps to the conduction band	3.3×10^{-5}
$q_{Fe,514}\, s_{Fe,514}$ (m^2/J)	Absorption cross section for absorbing a photon at wavelength 514 and exciting an electron from Fe traps to the conduction band	1×10^{-5}
$q_{Mn,404}\, s_{Mn,404}$ (m^2/J)	Absorption cross section for absorbing a photon at wavelength 404 and exciting an electron from Mn traps to the conduction band	1.25×10^{-5}
$q_{Mn,514}\, s_{Mn,514}$ (m^2/J)	Absorption cross section for absorbing a photon at wavelength 514 and exciting an electron from Mn traps to the conduction band	1×10^{-8}
$-\kappa_{Fe,404}$ (m^3/V)	Bulk photovoltaic coefficient for Fe at 404 nm	13×10^{-33}
$-\kappa_{Fe,514}$ (m^3/V)	Bulk photovoltaic coefficient for Fe at 514 nm	3.8×10^{-33}
$-\kappa_{Mn,404}$ (m^3/V)	Bulk photovoltaic coefficient for Mn at 404 nm	2.9×10^{-33}
$-\kappa_{Mn,514}$ (m^3/V)	Bulk photovoltaic coefficient for Mn at 514 nm	5×10^{-36}
A (mm^{-1})	Absorption coefficient at 404 nm	≈1

Table 2.3. Optimum design parameters and optimum *M/#* and sensitivity for $LiNbO_3$:Fe:Mn. The hologram is recorded in transmission geometry. The crystal thickness is 1 mm. The polarization of recording beams is ordinary.

Measure	Recording WL	Sensitizing WL	N_{Fe} (m^{-3})	N_{Mn} (m^{-3})	N_A (m^{-3})	I_R/I_{UV}	M/#	*S* (cm/J)
Optimum *M/#*	633 nm	365 nm	5×10^{25}	8.8×10^{23}	7.5×10^{23}	1	0.76	0.016
Optimum *M/#*	514 nm	404 nm	5×10^{25}	2.2×10^{24}	1.9×10^{24}	10	2.13	0.13
Optimum *S*	633 nm	365 nm	5×10^{25}	3.7×10^{25}	3.3×10^{25}	0.01	0.17	0.17
Optimum *S*	514 nm	404 nm	5×10^{25}	2.0×10^{25}	1.7×10^{25}	0.01	0.01	0.43

For sensitizing beam at 365 nm, the crystal has a significant absorption coefficient in the order of 9 mm^{-1}. Therefore, for a thick crystal, the intensity of the sensitizing beam drops dramatically as it passes through the crystal, and the intensity ratio deviates far

from the optimum. If the absorption is decreased, a larger portion of the crystal will experience the intensity ratio close to the optimum value, and both *M/#* and *S* will increase. Therefore, using a longer sensitizing wavelength (which has lower absorption) can result in higher sensitivity and *M/#*. In addition, Fe traps are more sensitive to 514 nm than 633 nm, i.e., the bulk photovoltaic coefficient of the Fe traps is larger at 514 nm [37]. Therefore, recording with 514 nm results in higher *M/#* and *S*. The main disadvantage of using 514 nm is that the reading beam can slightly excite electrons from Mn traps. Therefore, a hologram recorded with recording beams at 514 nm will have a smaller value of *R/#* [37].

To our best knowledge, the maximum experimental values for *M/#* and *S* in a 1 mm thick $LiNbO_3$:Fe:Mn crystal, with 365 nm sensitizing and 633 nm recording with ordinary polarization in transmission geometry, are 0.25/mm and 0.003 cm/J [33]. From Table 2.3 it is seen that for 633 nm and 365 nm beams, the maximum values of *M/#* = 0.76/mm and *S* = 0.17 cm/J can be achieved by using the optimum design parameters. By changing the recording and sensitizing beams to the new set of 514 nm and 404 nm, further improvement is obtained. Note that by using extraordinary polarization for recording beams, both *M/#* and *S* can be further improved by a factor of 3 because of the larger electro-optic coefficient of $LiNbO_3$ for extraordinary polarization.

Table 2.3 also represents the theoretical limit for *M/#* and *S* in $LiNbO_3$:Fe:Mn due to material specification. These limits are *M/#* = 2.13/mm and *S* = 0.43 cm/J both obtained with sensitization at 404 nm and recording at 514 nm. With extraordinary polarization, *M/#* = 6.4/mm and *S* = 1.3 cm/J can be obtained. Further improvements might be

obtained by application of a strong electric field [42] or by finding more appropriate dopants.

As explained earlier, the strong trade-off between *M/#* and *S* must be considered in designing doubly doped crystals. For example, the maximum *S* is obtained when I_R/I_{UV} =0.01, $N_{Mn} = 3.7\times10^{25}$, and $N_A/N_{Mn} = 0.9$. For this set of parameters, *M/#* is low. The large I_{UV} compared to I_R does not allow strong holograms to build up. On the other hand, optimum *M/#* is obtained when *S* is very low. For practical applications where very low *M/#* or *S* is undesirable, the design parameters should be selected appropriately to result in a desired set of *M/#* and *S*.

2.6 Conclusion

We presented a global optimization scheme for two-center holographic recording in doubly-doped crystals. Our method is based on a combination of analytic formulas derived here with numerical simulations. We considered both *M/#* and sensitivity in our method. The global optimum set of design parameters was found by varying all parameters simultaneously. We implemented the method for $LiNbO_3$:Fe:Mn crystals and found the optimum set of parameters for maximizing *M/#* and *S* at different reading and sensitizing wavelengths.

Our results show that the best *M/#* and *S* that can be obtained in two-center recording in $LiNbO_3$:Fe:Mn crystals are 2.13/mm and 0.43 cm/J, respectively, using ordinary polarization. With extraordinary polarization for recording and reading beams, *M/#* = 6.4/mm and *S* = 1.3 cm/J can be achieved. These results are obtained when sensitizing and recording wavelengths are 404 nm and 514 nm, respectively. The maximum of *M/#*

can be achieved when N_{Fe} is as large as possible, when N_{Mn} is more than one order of magnitude smaller than N_{Fe}, when about 85% of Mn traps are initially filled, and when the recording and sensitizing intensities are of the same order. On the other hand, the optimum value of S is obtained when both the N_{Fe} and N_{Mn} are as large as possible, when about the 90% of the Mn traps are initially occupied by electron, and when the sensitizing intensity is about 100 times larger than the recording intensity. Note that the optimum set of parameters for maximizing $M/\#$ and S are different. The maximum values of $M/\#$ and S cannot be achieved simultaneously and a trade-off exists.

We also presented here for the first time the complete dependence of sensitivity on the different design parameters. We theoretically showed that S is a function of the ratio between recording and sensitizing intensities (I_R/I_{UV}), and not the absolute intensities.

Chapter 3

Software Based Stabilized Holographic Recording System

3.1 Introduction

For fully characterizing the material, reliable recording for long period of time is needed. Successful recording of holograms strongly depends on the stability of the recording setup. Outside influences such as mechanical vibrations, temperature variation, or perturbations due to airflow will cause movement in the optical beam path that modifies directly affects the recording of the hologram. This limitation becomes more evident when attempting long holographic exposures; therefore, an active stabilizer is an integral factor in accurate characterization of the material.

The basic operation of an active stabilizer is to monitor any movement in the fringe pattern during a holographic recording session and compensate that movement by changing the phase of one of the recording beams. It is evident that the stability is in proportion to the preciseness of the measurement and the accuracy of the compensation; as such, eliminating background noise is a key factor for stabilization. Two such hardware components that satisfy the mentioned requirements are a lock-in amplifier (LIA) and a piezo-shifting mirror (PZM) [55-56]. A lock-in amplifier takes a periodic reference signal covered in a noisy input and uses a phase-sensitive detection to extract only that part of the output signal whose frequency and phase match the reference [57]. A piezo mirror-shifter is used for ultra-fine axial positioning with sub-micron resolution to

change the phase of the beam. It can be also used for modulating the phase of the beam at high resonance frequencies for lock-in detection [58]. The combination of these two components (LIA and PZM) into an interferometric setup allows for the ability to modulate a fringe pattern with minute amplitude, negligible to the recording session, and through beam coupling, extract the developing diffracted beam to stabilize the setup [59]. Disadvantages to this implementation are the experiment specific properties and the high costs of hardware components such as: PZM, LIA, function generator, and integrator.

In this Section, we present a simple and cost-effective approach to active stabilization that provides results comparable to those found in conventional hardware-based setups. The primary advantage of the proposed software-based technique is the replacement of the functionality of the previously mentioned hardware devices with the signal processing capabilities in the LabVIEW software [60-61] that is available in almost all optics labs. The software-based stabilizer system is used to perform several holographic experiments as explained in this chapter. Also with minimal modifications, the system is used for other experiments that are presented in the following chapters.

The concept of the stabilizer system is explained in Section 3.2. The experimental results from the software based stabilizer setup are discussed in Section 3.3. The setup is used to characterize a doubly doped lithium niobate crystal that is designed based on the theoretical optimization presented in Chapter 2. In particular, the results of the sensitivity variation in two-center recording in the designed crystal are presented in Section 3.4. The conclusion remarks are made in Section 3.5.

3.2 Software-based stabilizer setup

Figure 3.1 shows the setup for the stabilized system. The setup consists of two parts. The first part that is based on Mach-Zender Interferometry is primarily used for stabilization [56, 59]. The other part is used for recording the holograms in transmission geometry independent of the recording material. Note that these two parts are implemented using the same beams by placing the recording material (i.e. crystal) on top of the non-polarizing beam splitter (NPBS) as shown in Figure 3.1.

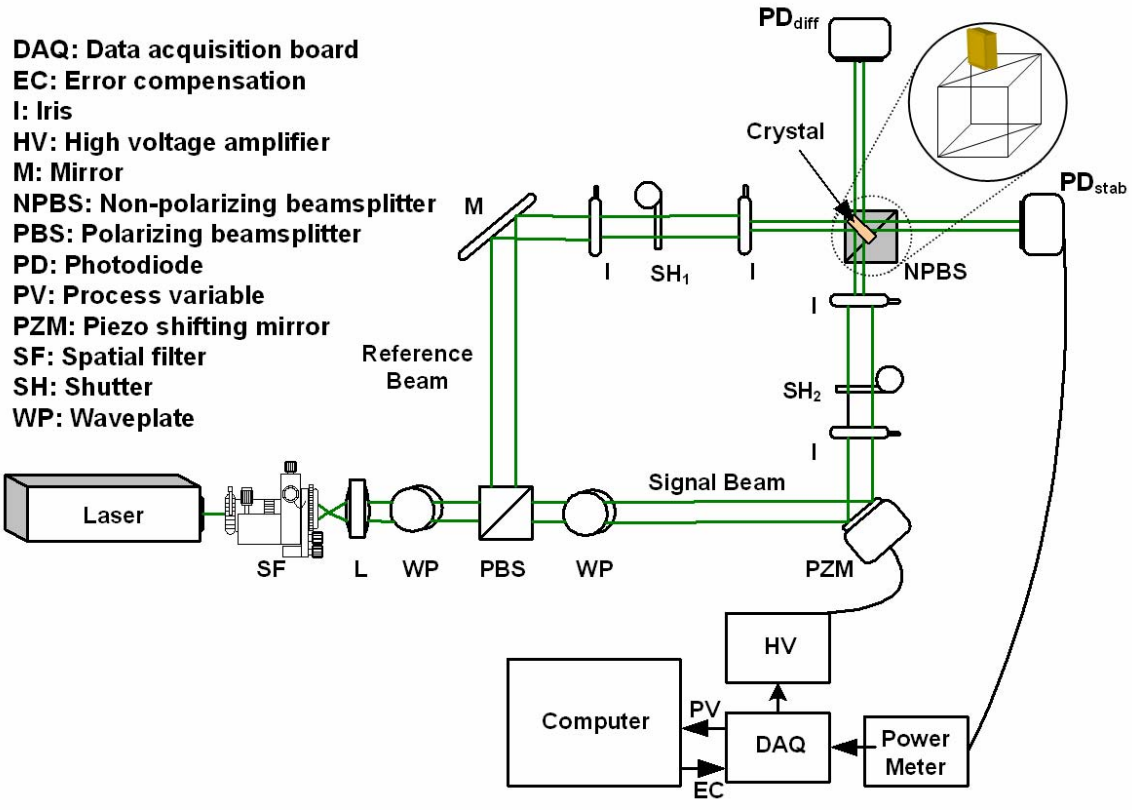

Figure 3.1. A Mach-Zender based interferometer stabilized by monitoring the movement of the interference pattern with a photodetector. The movement of the interference pattern is interpreted as a voltage and is sent through a DAQ card into a computer as a process variable (PV) which is then processed in software and returned as an error-compensation (EC) value through a DAQ card to the PZM through a high voltage amplifier. Note that the holographic recording material (shown by crystal) is mounted on top of the beam splitter (NPBS).

A continuous-wave solid-state laser generates light at λ = 532 nm. The beam is spatially filtered, expanded, collimated, and split into two beams. If the cross sections of the split beams are not large enough to encompass both the crystal and the beam splitter (NPBS), extra lenses (not shown in Figure 3.1) should be used to expand the beams. The lower portion of the signal beam is partially reflected by the non-polarizing beam splitter and overlaps with the partially transmitted reference beam. Since these two beams are collinear, large fringes can be formed at the photodetector, PD_{diff}, (Figure 3.2). The crystal is placed on the top of the beam splitter as shown in the inset of Figure 3.1. The upper portions of the reference and the signal beams overlap and form an interference pattern inside the crystal to record the hologram.

A PZM is placed in the path of the signal beam. Irises are used for alignment and to adjust the size of the beams that reach the crystal. The shutters, controlled in LabVIEW, are used for holographic recording and read out only. A photodetector, PD_{diff}, is placed in the signal beam path aligned with the height of the crystal to measure the intensity of the diffracted light, during read-out. The photodetector, PD_{stab}, placed in the reference beam path, is aligned below the crystal but in line with the beam splitter to monitor fringe movement.

Figure 3.2 shows the interference pattern observed in the location of PDstab. An extra lens might be used in front of PD_{stab} to magnify the image of the fringes on the detector. A black cardboard having a very small pinhole in the middle covers the photodetector. The size of the pinhole with respect to the fringe spacing should be small enough to measure fringe movement of $\lambda/50$. The fringe spacing depends on the alignment of the two beams after the NPBS, which can be adjusted by varying the

position of the beam splitter. It should be noted that the performance of the stabilizer depends on the accurate detection of the fringe movement that is in part a function of the diameter of the pinhole, the resolution of the detector, and the noise power at the detector. If the small change in the detected power corresponding to the fringe movement is less than the resolution of the detector or is comparable to the power of the noise, the fringe movement will not be detected correctly and the stability of the system will be less.

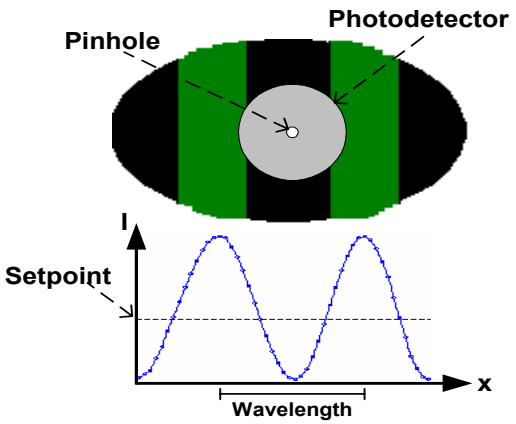

Figure 3.2. Illustration of a photodetector, with a pinhole, placed in the path of a magnified interference pattern. The reading from the photodetector is the process variable. The intensity (I) vs. distance (x) graph illustrates the quantitative position of the set point in relation to the intensity pattern.

To obtain a large contrast for the fringes and a high modulation depth for holographic recording, the intensity of the two beams should be the same. The first half wave-plate (WP1) is used to adjust the relative intensity of the reference and the signal beams. The second half wave plate (WP2) is used to rotate the polarization of the signal beam and make it the same as that of the reference beam.

The stabilization principle of this setup is rather straightforward: an arbitrary set point, corresponding to an arbitrary phase between the interfering beams is chosen (Figure 3.2). The fringe movement monitored by PD_{stab} is sent into a power meter whose

analog output was acquired by the computer via a data acquisition card (DAQ). The reading value from PD_{stab} photodetector is subtracted from the set point to produce an error signal, which is passed into two PID (proportional, integral, and derivative) controllers that are in series to compensate for the poles and zeroes of the unstable system and to make a closed loop stable one. The processed error is then passed to the PZM, which is used to compensate the phase perturbation in the fringe pattern. The PID gains are carefully set to obtain a good stability. The software part of the system is completely implemented using LabVIEW. Using this system, we were able to achieve the stability better than $\lambda/25$ (at recording wavelength $\lambda = 532$ nm) for intervals of at least two hours.

3.3 Stabilized holographic recording

Figure 3.3 shows the output of the photodetector (PDstab) for two measurements. In the first measurement, Figure 3.3(a), the stabilizer system is off. The measured power is the actual fluctuation in the fringe pattern of the system. Reasons for such erratic behavior may be attributed to vibration from laser cooling fans, shutters, motors, thermal gradients, air motion (both convective and random), ambient temperature changes, humidity changes, and aging optics. In the second measurement, Figure 3.3(b), the stabilizer system is active and keeps the system stable around the set point corresponding to 10 mW/cm^2. Comparing these two figures clearly shows the importance of the active stabilizer system.

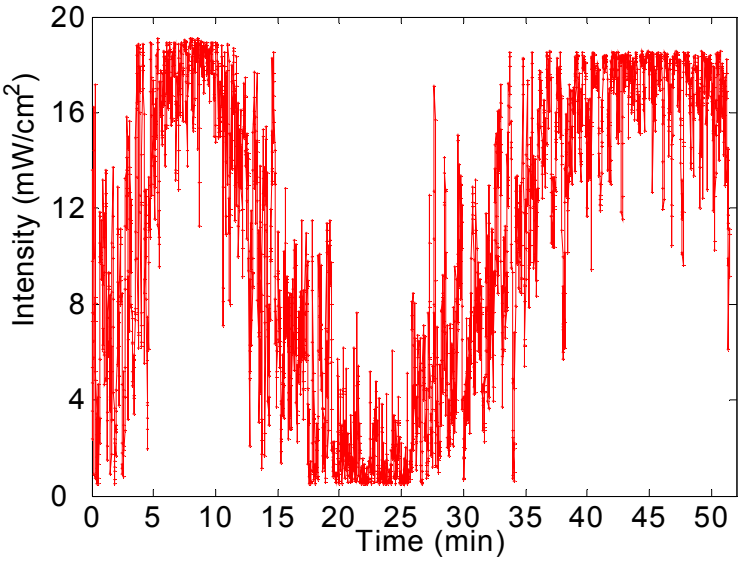

(a)

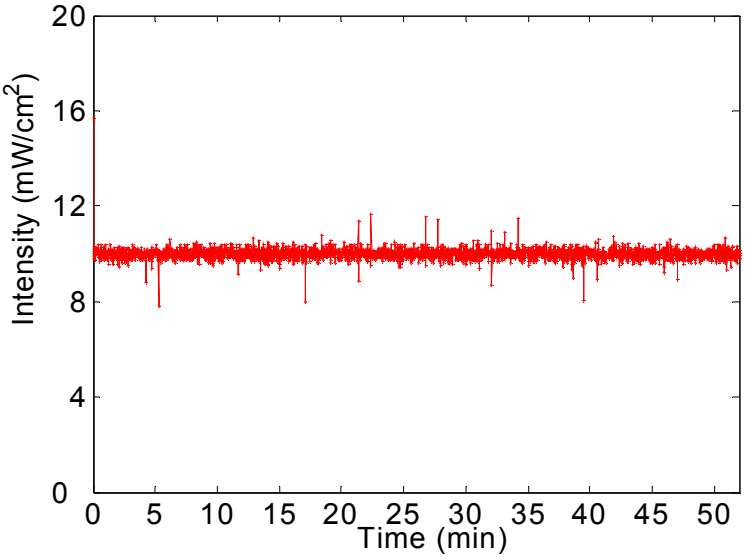

(b)

Figure 3.3. Intensity monitored by stabilizer photodetector (PD_{stab}) over 50 minutes interval for two cases, (a) without active stabilizer and (b) with active stabilizer.

To show the importance of using the stabilizer system for holographic recording, we performed two similar experiments with and without the operation of the stabilizer. For two-center holographic recording, a 2 mm thick congruent $LiNbO_3$ crystal doped with

0.15 wt. % Fe_2O_3 and 0.02 wt. % MnO is first oxidized at 1070 ºC for 48 hours in an oxygen environment and then placed into the setup with recording intensities of the signal beam, I_{sig} = 43 mW/cm^2, and the reference beam, I_{ref} = 43 mW/cm^2. The two beams have ordinary polarization (*i.e.*, the electric field is perpendicular to the plane of incident) and the grating is formed in the direction of the c-axis of the crystal. During the recording, the crystal is sensitized by a blue laser at wavelength λ = 404 nm (not shown in Figure 3.1). The intensity of the sensitizing beam is 38 mW/cm^2. Figure 3.4 shows the development of the diffraction efficiency (with time) under stabilized and non-stabilized conditions.

Under non-stabilized conditions, Figure 3.4(a), the hologram exhibits patterns of erasure and re-recording, which is the indication of the instability of the recording fringe pattern. In contrast, Figure 3.4(b) illustrates continuous recording of the volume hologram to its saturation level, which is an indication of excellent fringe stability provided by the stabilizer. Figure 3.4 suggests that without the stabilizer, the holographic recording setup would not provide reliable measurements for accurate characterization of doubly doped crystals for two-center recording.

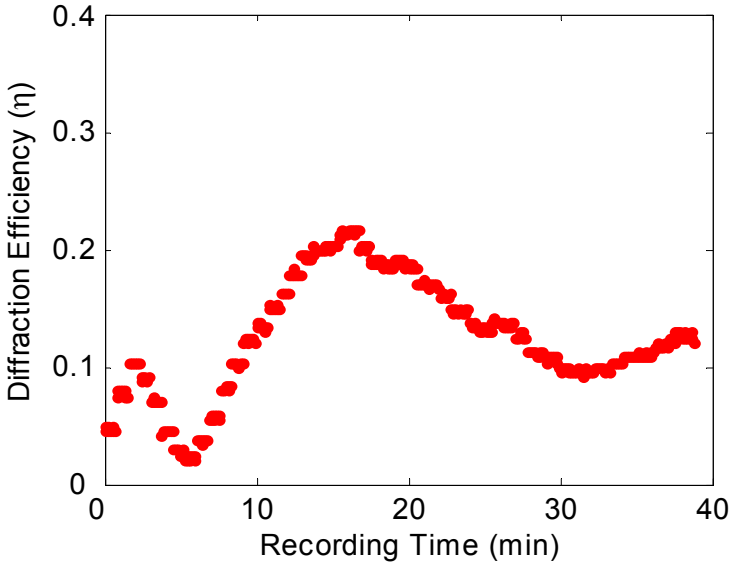

(a)

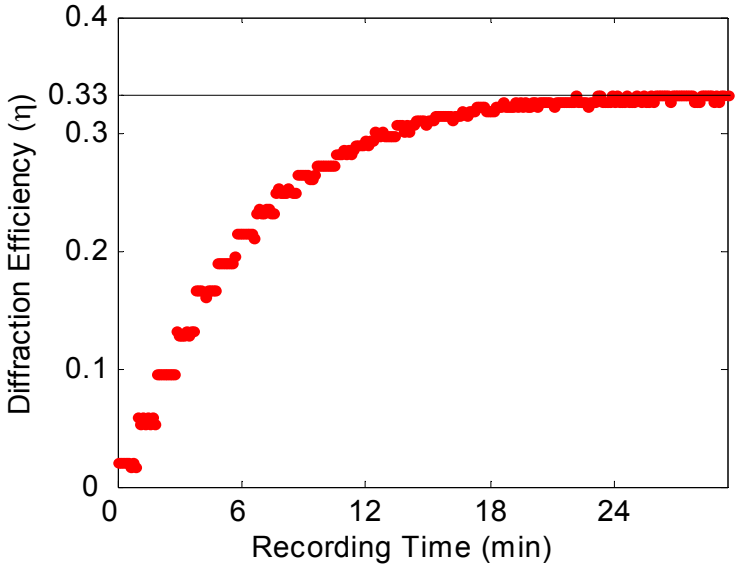

(b)

Figure 3.4. Development of the grating as illustrated by the diffraction efficiency versus the recording time for a two-center hologram recoded in a 2 mm thick $LiNbO_3$:Fe:Mn crystal (a) under non-stabilized conditions, and (b) under stabilized conditions. Total recording beam intensity and the sensitizing intensity were 86 mW/cm^2 and 38 mW/cm^2, respectively, and sensitization and recording wavelengths are 532 nm and 404 nm, respectively.

3.4 Sensitivity variation in two-center recording

Despite extensive research on the properties and improvement of the *M*/# in two-center recording, there have been only a few reports (especially experimental) on the properties of the sensitivity in this technique [37, 52]. In this section, we report for the first time, a detailed experimental study of the role of recording and sensitizing intensities in the sensitivity in two-center recording. All experiments reported in this section were performed using a modified stabilized recording system shown in Figure 3.5.

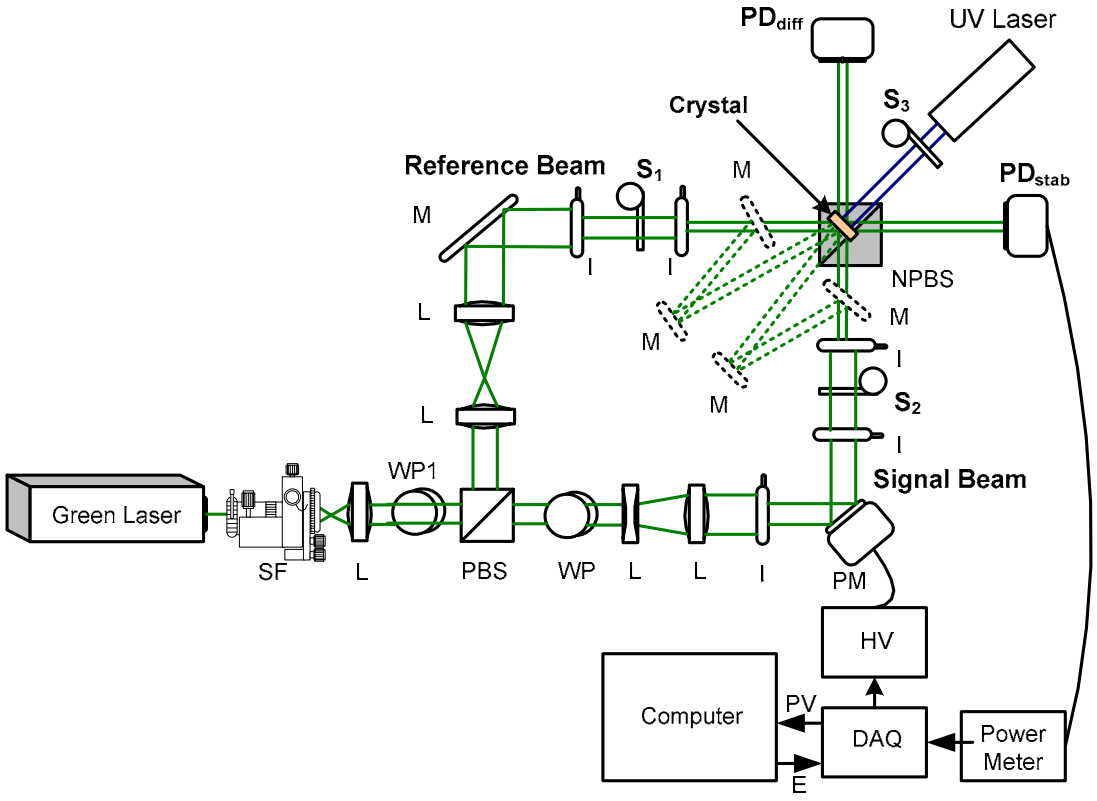

Figure 3.5. Experimental setup for sensitivity measurement based on software-based stabilized setup. DAQ, data acquisition card; HV, high voltage amplifier; I, iris; L, lens; M, mirror; NPBS, non-polarizing beam splitter; PBS, polarizing beam splitter; PD, power detector; PM, piezo-driven mirror; S, shutter; SF, spatial filter; WP: half waveplate.

The crystal used for the experiments is a 2 mm thick $LiNbO_3$:Fe:Mn crystal doped with 0.15 wt.% Fe_2O_3 and 0.02 wt.% MnO. The crystal is oxidized at 1070 ºC for 48 hours in an oxygen environment. The absorption spectrum of the crystal is measured in two different cases; after sensitizing the crystal and after bleaching the crystal. For the sensitizing experiment, the crystal is sensitized using a beam from a blue laser with a wavelength of 404 nm and a power of 5 W for an hour. In the bleaching experiment, the crystal is bleached using a 20 W He-Ne laser (wavelength 633 nm) for 45 minutes. The absorption spectrums in both cases are shown in Figure 3.6. When the crystal is bleached, all the electrons are trapped in the Mn traps and the Fe traps are empty. Therefore, the absorption of the crystal at the wavelength of 470 nm and up is very small. After sensitizing the crystal, the Fe traps are partially filled and, therefore, the absorption in the longer wavelength of the spectrum is increased.

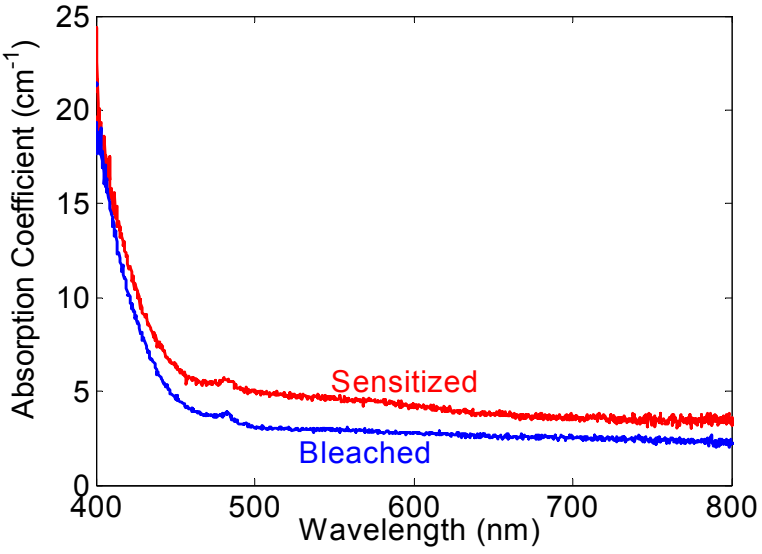

Figure 3.6. Absorption spectrum for sensitized and bleached crystal. The crystal is a 2 mm thick $LiNbO_3$:Fe:Mn crystal doped with 0.15 wt.% Fe_2O_3 and 0.02 wt.% MnO.

To study the variation of the sensitivity in two-center recording, different holograms were recorded using different sets of recording and sensitizing intensities. Before any experiment, the crystal was illuminated with the UV beam to erase the existing holograms. Then, a two-center hologram is recorded to saturation for a long time (1 hour or more) using two beams (shown by the dashed lines in Figure 3.5), which are Bragg-mismatched with the reference and signal beams of the desired hologram. This process is added to obtain a steady state electron concentration in the Fe and the Mn traps before recording the desired hologram in order to have a reliable measurement of the sensitivity. Then, the desired hologram is recorded using the reference and signal beams as shown in Figure 3.5 for at least 3 minutes and the diffraction efficiency is monitored in 30 seconds intervals. After each recording, the hologram was illuminated by the two Bragg-mismatched beams (shown by dashed lines in Figure 3.5) and the sensitizing beam for at least 30 minutes to erase the previous hologram before recording the next desired hologram while the average electron concentrations in the two traps were kept at their steady-state value during recording. For each set of recording and sensitizing intensities, the same experiment was repeated at least four times and the recording time in the forth experiment was chosen long enough to make sure the hologram reached the saturation. The hologram was then illuminated using one of the Bragg-mismatched beams to partially erase the hologram and to find the persistent diffraction efficiency. Figure 3.7 shows a typical reading and readout curve with total recording intensity I_{rec} = 50 mW/cm^2 and sensitizing intensity I_{sen} = 18 mW/cm^2. The hologram was recorded for 20 minutes. Then, the hologram was under the illumination of a Bragg-mismatched beam with 25

mW/cm^2 intensity for 80 minutes. The erasure rate of the hologram is very small after 80 minutes and the persistent diffraction efficiency is shown by η_2 in this figure.

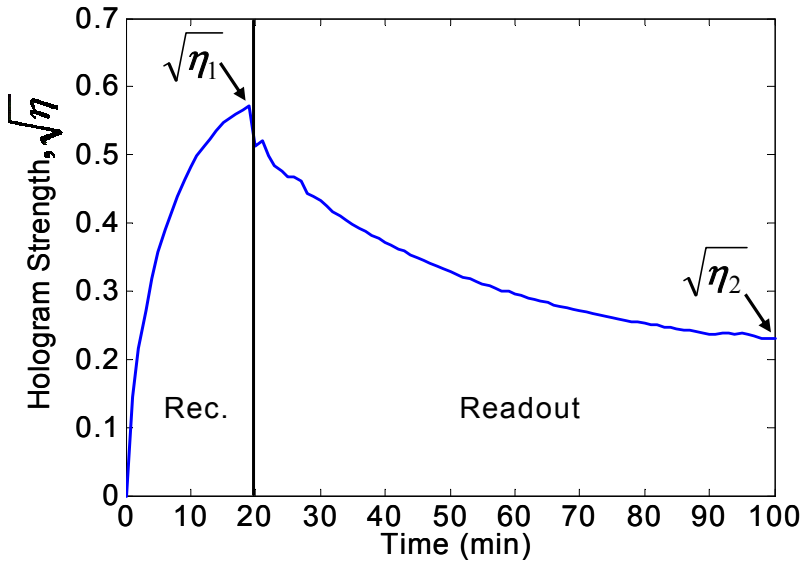

Figure 3.7. A typical reading and readout curve for the $LiNbO_3$:Fe:Mn crystal described in the text with I_{rec} = 50 mW/cm^2 and I_{sen} = 18 mW/cm^2. The hologram was recorded for 20 minutes. Then, the hologram was under the illumination of a Bragg-mismatched beam with 25 mW/cm^2 intensity for 80 minutes.

The sensitivity (S) is calculated using Equation (2.14). The persistent sensitivity in two-center recording is defined as

$$S' = S\beta = \frac{\beta}{I_{rec}L} \times \left. \frac{d\sqrt{\eta}}{dt} \right|_{t=0}, \tag{3.1}$$

where β is the persistent ratio and defined earlier. The values of S and S' were calculated for all four experiments and then averaged to find the sensitivity for each set of intensities.

Figure 3.8 shows the variation of S with the recording intensity when the ratio of the recording and sensitizing intensities is kept constant at I_{rec}/I_{sen} = 3.1. As it is seen in

Figure 3.8, the sensitivity is almost constant for a fixed intensity ratio. It should be noted that only S is shown in Figure 3.8. We know that the saturated and the persistent hologram strengths are functions of the intensity ratio (I_{rec}/I_{sen}) (from the analysis in Chapter 2). Therefore, the persistent factor β and the persistent sensitivity (S') are function of I_{rec}/I_{sen} and not the absolute intensities. This is exactly in agreement with the theoretical results obtained in Chapter 2. Therefore, to obtain the complete variation of sensitivity with respect to recording and sensitizing intensities, we only need to find S (or S') as a function of I_{rec}/I_{sen}.

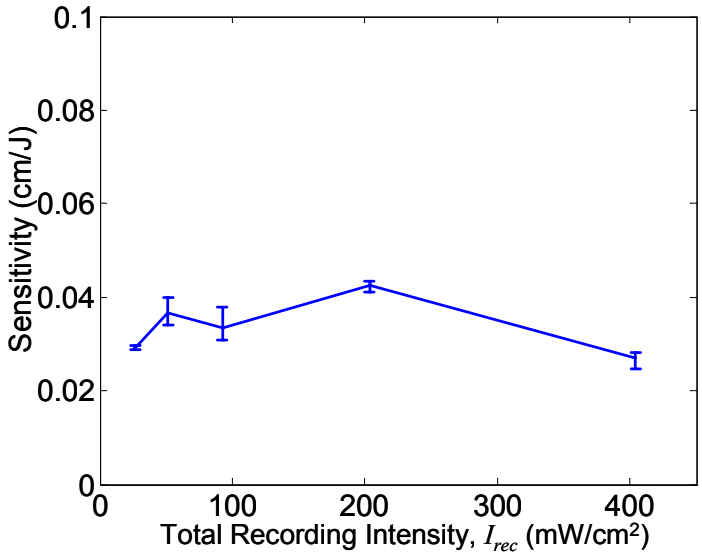

Figure 3.8. Sensitivity (S) in two-center recording as a function of total recording intensity (I_{rec}) while the recording to sensitizing intensity ratio is fixed at I_{rec}/I_{sen} = 3.1. The properties of the recording material are described in the text.

The variation of sensitivity (S) with I_{rec}/I_{sen} is shown in Figure 3.9. From Figure 3.9 it is clear that S decreases as the intensity ratio increases. Similar variation for S was seen using the theoretical analysis. Another important result is that the maximum sensitivity (S), which is 0.15 cm/J, is obtained with the intensity ratio of I_{rec}/I_{sen} = 0.54. This suggests that for achieving high sensitivity, we need to use a sensitizing beam with higher

intensity compared to the recording intensities. At I_{rec}/I_{sen} = 0.54 (which results in highest value of S = 0.15 cm/J), we measured $M/\#$ = 0.08 mm^{-1}. As known from the theoretical analysis, maximum value of S and maximum value of $M/\#$ cannot be obtained in the same crystal as the design conditions for the two maxima are considerably different.

The variation of persistent sensitivity (S') with I_{rec}/I_{sen} is also shown in Figure 3.9. As it is clear in this figure, the persistent (S') reaches its maximum value of S' = 0.08 cm/J around the intensity ratio of 0.54. Further decrease of the intensity ratio will result in the reduction of S'. On the other hand, for high intensity ratios, the difference between S and S' becomes smaller because of larger values of β at higher I_{rec}/I_{sen}. The variation of S' with the I_{rec}/I_{sen} is also in good agreement with the theoretical results in Chapter 2. Note that, the thickness of the crystal used in our experiments was 2 mm. Because of high absorption of the crystal (we measured α = 15 cm^{-1} at λ = 404 nm), the sensitizing beam intensity has a strong variation over the crystal thickness. Thus, the contributions of different slices of the crystal to the sensitivity are different and only a small portion of the crystal can observe the optimum value of I_{rec}/I_{sen}. Using a thinner crystal or sensitizing from both sides of the crystal, we can obtain higher values for sensitivity ($S \approx 0.3$ cm/J). Nevertheless, S = 0.15 cm/J is the highest sensitivity that has reported to date for a $LiNbO_3$:Fe:Mn crystal.

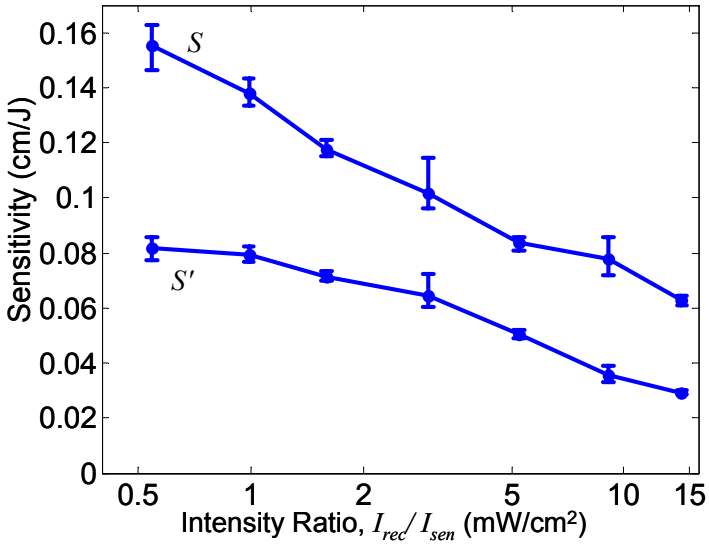

Figure 3.9. Sensitivity (*S*) and persistent sensitivity (*S'*) in two-center recording as functions of the ratio of recording to sensitizing intensities (I_{rec}/I_{sen}) with I_{sen} = 36 mW/cm^2 for the $LiNbO_3$:Fe:Mn crystal described in the text. The persistent sensitivity (*S'*) is equal to $\beta \cdot S$.

3.5 Conclusion

Problems such as random air motion and fluctuations in the ambient temperature result in changes in the optical path length that severely affect the recording of the holograms. Since disturbance in the optical path length can be detected in the form of the phase variation and the interference phenomenon, monitoring the phase variations of the interference pattern provides an accurate method to stabilize the holographic setup. We reported here, the implementation of this by a simple technique in software using LabVIEW. The software-basis of this design greatly reduces the cost of the stabilized holographic recording setup at minimal compromise in system stability. Our setup provides an overall stability of λ/25 for periods of up to six hours, at a significantly reduced cost when compared to conventional hardware-based setups. The only elements needed in our design are: computer, LabVIEW software, piezo shifting mirror,

photodetector, and data acquisition card with A/D and D/A conversion. It should be mentioned that these elements, apart from the piezo mirror, are available in almost all optical laboratories. Based on these relatively standard requirements and the ease of replication with software, it is conceivable that a software-based stabilizer may be placed in every lab that requires long time holographic exposures with excellent stability at minimal cost.

We used the stabilized system to experimentally investigate the sensitivity variation in two-center recording. We showed the complete experimental variation of sensitivity in two-center recording as a function of recording and sensitizing intensities. The results are in good agreement with the theoretical predictions. Our results show that the sensitivity in two-center recording is a function of the ratio of the recording to sensitizing intensities and not the absolute intensities. Also, in recording at 532 nm wavelength and sensitizing at 404 nm wavelength, using high intensity UV sources is a key element for fast recording in doubly doped crystals.

Chapter 4

Two-Center Holographic Recording in Highly Doped $LiNbO_3$ Crystals

4.1 Introduction

In Chapter 2, we investigated the complete variation of dynamic range and sensitivity in $LiNbO_3$:Fe:Mn crystals. We showed that increasing the Fe concentration would result in an increase in the diffraction efficiency. This is similar to what had been reported for singly doped $LiNbO_3$:Fe crystals. However, the maximum concentration for Fe is limited in the singly doped crystals since the hologram will be erased, even in dark, because of the tunneling between adjacent Fe sites [50].

As mentioned in Chapter 2, high Fe concentrations in doubly doped crystal would not necessarily result in the erasure of the stored hologram. In two-center recording, the hologram is eventually stored in the deeper trap (Mn trap). The electron tunneling between Fe traps will not affect the final hologram that is stored in Mn traps. Furthermore, the tunneling between Fe traps during recording and at the beginning of the readout may result in an increase of the diffraction efficiency of the hologram. From the analysis in Chapter 2, we know that In two-center recording, the modulated electron concentrations in Fe and Mn traps are almost equal with 180º-phase shift. Therefore, the two concentrations almost cancel each other except for a small net electron concentration that stores as the hologram. In this case, partial erasure of the electron concentration in Fe

due to tunneling will result in an increase in net electron concentration and, therefore, strengthens the hologram.

In this chapter, we investigate two-center recording in highly doped $LiNbO_3$:Fe:Mn. In Section 4.2, we present the experimental evidence of tunneling in a $LiNbO_3$:Fe:Mn crystal doped with high Fe concentration. We present the experimental results for both enhancement and erasure of the hologram after the recording and in the absence of any external excitation. We believe this effect is because of the electron tunneling between the traps. We develop a theoretical model for tunneling in two-center recording based on the two-center model in Section 4.3. Also, the theoretical results are presented and discussed in this section. Final conclusions are made in Section 4.4.

4.2 Electron tunneling in highly doped $LiNbO_3$:Fe:Mn

In $LiNbO_3$:Fe crystals, the tunneling effect has been observed for Fe concentrations above 0.05 wt.% Fe_2O_3 [50]. The tunneling effect is also observed in $LiNbO_3$ crystals doped with Mn for dopant level of more than 0.5 wt.% $MnCO_3$ [62]. In $LiNbO_3$:Mn the tunneling effect occurs at higher dopant concentrations compared to that in $LiNbO_3$:Fe. The Mn dopant provides a deeper trap compared to Fe dopant, thus, the electrons are confined by a larger barrier in Mn traps and the probability of tunneling is lower [62]. To the best of our knowledge, there is no report on the observation of the electron tunneling in doubly doped $LiNbO_3$.

To investigate the evidence of tunneling in two-center recording, we used a congruently grown $LiNbO_3$:Fe:Mn crystal with 0.15 wt.% Fe_2O_3 and 0.02 wt.% MnO. The Fe concentration in this crystal is more than the threshold concentration for electron

tunneling in $LiNbO_3$:Fe. Since the hologram is eventually stored in Mn traps, the Mn concentration is selected to be lower than the concentration needed for observing electron tunneling. A sample with the size of 10 mm × 10 mm × 2 mm was cut so that the c-axis lies in the larger face and is parallel to one of the edges. Initially, the sample was oxidized in oxygen atmosphere at 1070º C for 48 hours.

The sample was used in the stabilized recording system of Figure 3.1. Two green beams at the wavelength of 532 nm and with equal intensities were used to record the holograms in symmetric transmission geometry. A beam at the wavelength of 404 nm from a CW diode laser was used as the sensitizing beam. The diffraction efficiency is defined as the ratio of the diffracted beam intensity to the reading beam intensity and was measured using the reference beam. The polarization of the recording beams was TE (*i.e.* electric field perpendicular to the plane of incident).

Figure 4.1 shows the diffraction efficiency for a hologram recorded for 30 minutes and immediately read for 3 hours. Total recording intensity and the sensitizing intensity were 23 mW/cm^2 and 10 mW/cm^2, respectively. Before the recording phase, the hologram was sensitized with the sensitizing beam for 1 hour. After recording, the hologram was illuminated by a Bragg mismatched beam at 532 nm with an intensity equal to the intensity of each of the recording beams. The diffraction efficiency of the hologram was monitored every minute using the reference beam. As seen in Figure 4.1, the dynamic of the recording phase is similar to two-center recording we observed in the previous chapters. However, the readout portion of the curve shows a new behavior not being observed before. The diffraction efficiency does not decrease at the beginning of the readout (corresponding to the partial erasure of the hologram). Instead, the diffraction

efficiency increases first and then decreases. To reduce the possible experimental uncertainty, the experiment was repeated several times and the same behavior was observed in all the attempts. Note that the hologram was illuminated with a Bragg mismatched beam during the readout, therefore, this effect is not because of two-wave coupling that is responsible for self-enhancement of the diffraction efficiency during the Bragg-matched readout in some applications [63].

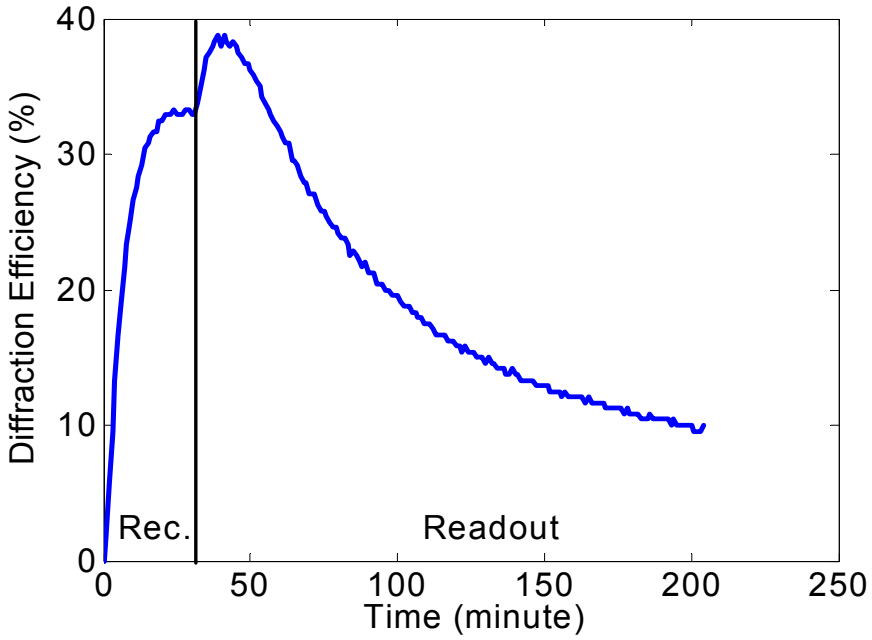

Figure 4.1. Recording-readout curve for $LiNbO_3$:Fe:Mn doped with 0.15 wt. % Fe_2O_3 and 0.02 wt. % MnO. A 2 mm thick sample is used. The sensitizing and recording wavelengths are 404 nm and 532 nm, respectively. Sensitizing intensity and the total recording intensity are 10 mW/cm^2 and 23 mW/cm^2, respectively. The polarization of the recording beams is ordinary. Readout is performed while the crystal is illuminated using a Bragg mismatched green (λ = 532 nm) beam with an intensity of 10 mW/cm^2. The total angle between the recording beams outside the crystal is 90^o in transmission geometry. Recording time is 30 minutes.

To investigate the increase in diffraction efficiency after recording, another experiment was performed, in which, after the recording, the hologram was kept in the dark and the diffraction efficiency was monitored from time to time using a weak reading beam. Total exposure of the reading beam was kept small to minimize the possible

affects on the hologram. After reading in the dark, the hologram was read in the presence of Bragg-mismatched beam, similar to the one used in the previous experiment, to observe the partial erasure of the hologram. Figure 4.2 shows the experimental results for recoding the hologram for 30 minutes followed by dark monitoring for 145 minutes. The readout in the presence of Bragg-mismatched illumination was performed after the dark monitoring phase for another 150 minutes. As it is seen in Figure 4.2, the diffraction efficiency keeps increasing after the recording while being in the dark without any external excitation. This is the first observation of enhancement in the diffraction efficiency of a hologram recorded in $LiNbO_3$ crystals without the presence of any illumination or heating. As we will explain in the following sections, this effect is an indication of electron tunneling in our sample.

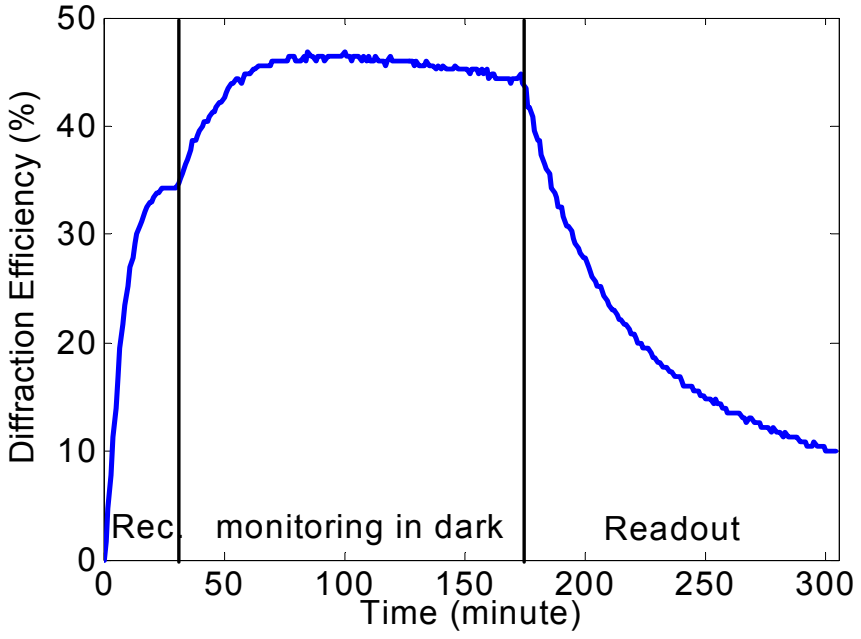

Figure 4.2. Dynamics of the diffraction efficiency for Recording, dark monitoring, and readout for $LiNbO_3$:Fe:Mn doped with 0.15 wt. % Fe_2O_3 and 0.02 wt. % MnO. After the recording phase the crystal is kept in the dark while the diffraction efficiency is monitored from time to time. All other parameters are the same as those in the caption of Figure 4.1.

To investigate the effect of the recording conditions, we perform a similar experiment using recording beams at the wavelength of 633 nm. As before, the experimental setup is based on Figure 3.1 while the half wave plates (WP's) are replaced with the ones operating at the wavelength of 633 nm. The variation of the diffraction efficiency as a function of time is shown in Figure 4.3. First, the hologram is recorded using two red beams with total recording intensity of 200 mW/cm^2 and a sensitizing beam with intensity of 18 mW/cm^2. The hologram was recorded for 30 minutes. Immediately after the recording, the intensity of the reference beam was reduced to 5.1 mW/cm^2. The diffraction efficiency was then monitored for 110 minutes using the low intensity reference beam when the crystal was kept in dark. The low intensity beam shined the hologram for at most 1.5 seconds for every 2 minutes; therefore, the effect of monitoring on the diffraction efficiency is minimal. It is clear from Figure 4.3 that the diffraction efficiency decreases in the dark without any external excitation. This effect is similar to the dark erasure observed for singly doped $LiNbO_3$:Fe that is because of electron tunneling [50]. We expect that the dark erasure, observed in Figure 4.3, is also from the electron tunneling in the Fe traps. However, the effect observed for recording the hologram using the red beams is totally different from that for recording using green beams. When the hologram was recorded with the green beams, the diffraction efficiency was enhanced in the dark. However, recording with red beams caused the erasure of the hologram in the dark. We have repeated the experiments for several sets of recording and sensitizing intensities. In all the experiment using the green recording beams, after recording the hologram, the diffraction efficiency was enhanced or remained unchanged

in dark. For recording with the red beams, we always observed the erasure of the hologram in dark.

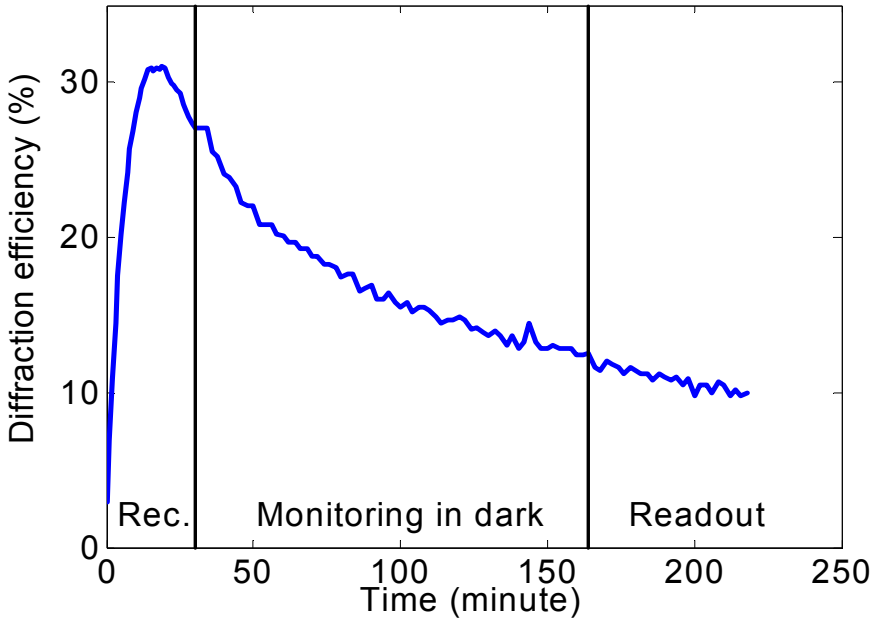

Figure 4.3. Dynamics of the diffraction efficiency for Recording, dark monitoring, and readout for a hologram recorded using two red beams. The sensitizing and recording wavelengths are 404 nm and 633 nm, respectively. Sensitizing intensity and the total recording intensity are 18 mW/cm^2 and 200 mW/cm^2, respectively. The intensity of the reading beam during the dark monitoring is 5.1 mW/cm^2. During the readout, the hologram is under the illumination of a Bragg-mismatched beam with the intensity of 100 mW/cm^2. All the other parameters are the same as those in the caption of Figure 4.1.

For the electron tunneling in $LiNbO_3$:Fe, it is easy to understand the physics of the process. The electrons tunnel between Fe sites and try to redistribute uniformly. The hologram is gradually erased in this process till it is completely vanished when the electrons are uniformly distributed. However, the tunneling process in two-center recording is more complicated. In the next section, we develop a model for the electron tunneling in two-center recording. Based on the model, we explain the different observations of the variations of the diffraction efficiency monitored in dark for recording with red and green beams.

4.3 Modeling of electron tunneling in two-center recording

The electron tunneling between the dopant sites for holographic recording in $LiNbO_3$ crystals is a complicated process. Previous reports provide only the experimental evidences of the tunneling in $LiNbO_3$:Fe and $LiNbO_3$:Mn [50, 62]. Because of the difficulty of the accurate modeling of the electron tunneling, no theoretical analysis is available in the literature. In this section we develop a model for the overall effect of the tunneling in two-center recording.

We start by investigating the possibility of existence of the electron tunneling in our sample. The concentration of Fe in the $LiNbO_3$:Fe:Mn crystal doped with 0.15 wt.% Fe_2O_3 and 0.02 wt.% MnO is 5.0×10^{25} m^{-3}. Therefore, the average distance between the Fe sites in this crystal is about 2.7 nm. The probability of electron tunneling (p) through a barrier with the width w, and the height V is [62]

$$p = \frac{16E(V-E)}{V^2}\exp\left[\frac{-4\pi w}{h}\sqrt{2m(V-E)}\right] \tag{4.1}$$

where, h is the Plank's constant, and m and E are the mass and the energy of the electron, respectively. It is clear that the probability of the electron tunneling increases exponentially when the width of the barrier (w) decreases. The average distance between the Fe sites in our sample is small enough to have significant probability for electron tunneling. Also, the electron tunneling from Fe traps to Mn traps is possible in this crystal. The Fe traps form a three-dimensional grid with an average distance of 2.7 nm in each direction. Therefore, for any empty Mn site there might be a filled Fe site at an

average distance of 2.7 nm or less. The tunneling from the Fe sites to the Mn sites is an indirect tunneling since the energy of the electron is changed during this process. This tunneling requires exchanging energy with the structure using phonons. However, the tunneling from Mn sites to Fe sites is highly unlikely. The Mn traps are deeper in the band diagram of the crystal compared to Fe traps, therefore, the potential barrier is larger for electrons trapped in Mn sites. Also, electron tunneling from deeper Mn sites to shallower Fe sites requires absorption of energy from phonons, which is unlikely to happen. We can conclude that the electron tunneling can happen between the Fe sites and also from Fe sites to Mn sites. The electron has a probability for tunneling if the adjacent site (the Fe site or the Mn site) is empty and it is not already occupied by another electron.

When the hologram is recorded inside the crystal, the space-charge electric field is built up, which produces an electric potential. This electric potential modifies the electron energy levels and affects the tunneling process. To understand this better, the energy levels of the conduction band (CB), the valence band (VB), and the Fe dopants for a typical hologram recorded in the $LiNbO_3$:Fe:Mn crystal are shown in Figure 4.4(a). The variation of the energy levels is shown in the direction of the grating vector. The grating period (Λ) is calculated for a hologram recorded using two green beams in the arrangement of Figure 3.1. The energy level corresponding to Mn traps has a similar variation as Fe traps and is not shown in this figure. For the modified energy levels, the electron tunneling would have a higher probability when the tunneling is from a dopant site at higher energy to a site at lower energy. On average, electrons tend to occupy the lower energy states. However, as the electrons, on average, go to lower energy levels by

tunneling, they change the charge distribution and modify the space-charge electric field. As a result, the energy levels in the direction of the grating vector are changed. Figure 4.4(b) shows the modulated electron concentration in Fe and Mn traps in the direction of the grating vector in a hologram recorded with two plane waves at the wavelength of 532 nm. All the parameters are the same as those used in the experiment corresponding to Figure 4.1. The numerical simulation for the recording is obtained based on the two-center model presented in Chapter 2 without considering the tunneling effect. The data is for a hologram recorded for 30 minutes. It is seen in Figure 4.4(b) that the modulated electron concentrations in Fe and Mn have a phase shift of about 180º with respect to each other. The electric potential has a phase shift (about -90º) with respect to the Fe concentration. Therefore, the overall effect of tunneling in the Fe sites would be to shift the modulated Fe concentration in a way to occupy the lowest energy states. Also, in the tunneling process, the amplitude of the modulated electron concentration in Fe might change since the electrons in regions with higher concentration tend to go to the region with lower concentration. Considering these two changes in the modulated electron concentration in Fe, we can relate the large-scale effect of the electron tunneling as drift and diffusion currents in Fe traps only.

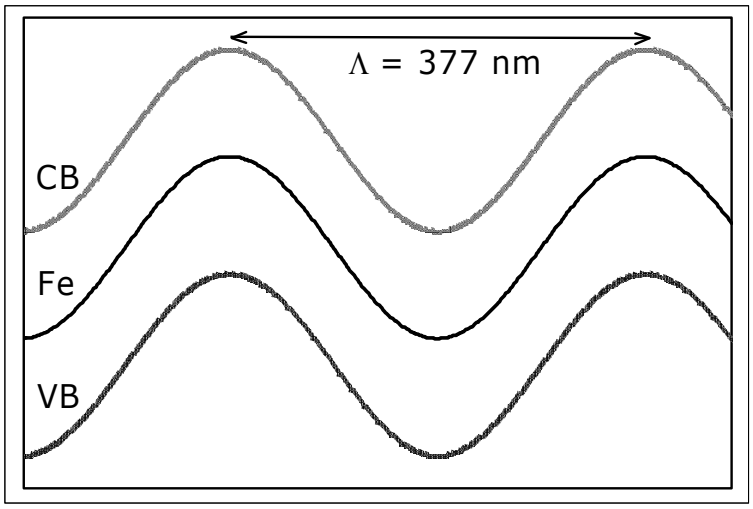

(a)

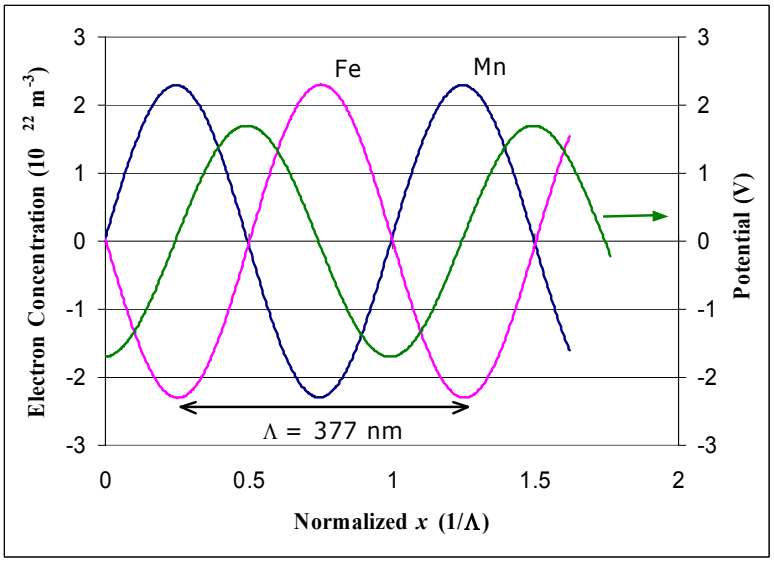

(b)

Figure 4.4. (a) The energy levels of the conduction band (CB), the valence band (VB), and the Fe dopants in the presence of the space-charge electric field and (b) the modulated electron concentration in Fe and Mn traps in the direction of the grating vector for a hologram recorded in the $LiNbO_3$:Fe:Mn crystal. The numerical simulation for the recording is obtained based on the two-center model presented in Chapter 2 without considering the tunneling effect. All the parameters are the same as those used in the experiment corresponding to Figure 4.1. The data is for a hologram recorded for 30 minutes.

The effect of the tunneling from Fe sites to Mn sites is more complicated, but it has significantly lower probability compared to the tunneling between Fe sites as we will be discussed later in this chapter. The electron tunneling from Fe sites to Mn sites can also

result in the movement of the electrons to lower states of the energy. We expect a higher probability of tunneling at the regions where we have more electrons in Fe traps. At the regions with more electrons in Fe traps, the electron concentration in Mn is lower. Therefore, the electron tunneling from Fe sites to Mn sites has an overall effect similar to that for the tunneling between Fe sites and we can use the same model to represent both effects. However, we assume a lower rate for the tunneling from Fe site to the Mn sites compare to that between Fe sites.

In both of the tunneling processes, the vacancy of the neighboring states in the probability of the tunneling should be considered. For example, for electron tunneling between Fe traps, this dependency can be simply included in the tunneling probability as a factor proportional to the ratio of concentration of empty Fe sites to the total Fe concentration.

We now modify the model for two-center holographic recording using the assumptions we have made so far to include the effect of tunneling. We consider the electron tunneling to change the modulated electron concentrations in the traps and do not affect the average concentration of electrons in Fe and Mn traps. The tunneling would change the modulated electron concentrations that are very small compared to the average concentration of electrons in both traps. The change in the average electron concentration in Mn and Fe traps is negligible since the probability of electron tunneling from the Fe sites to the Mn sites is very small. Also, electron tunneling between the Fe sites does not change the average electron concentration in Fe.

Similar to the approach used in Section 2, we assume a sinusoidal variation of the recording intensity, *i.e.* $I_L=I_{L0}[1+m\cos(Kx)]$, and consider the first two terms in the

spatial Fourier series of all variables, *i.e.* $N_D = N_{D0}^- + N_{D1}^- \exp(-iKx)$. We can find two sets of zeroth and first order equations based on the two-center model as

$$\begin{cases} \dfrac{dN_{D0}^-}{dt} = -\left(q_{D,L}s_{D,L}I_{L0} + q_{D,H}s_{D,H}I_H\right)N_{D0}^- + \gamma_D n_0\left(N_D - N_{D0}^-\right) & (4.2) \\ \dfrac{dN_{S0}^-}{dt} = -\left(q_{S,L}s_{S,L}I_{L0} + q_{S,H}s_{S,H}I_H\right)N_{S0}^- + \gamma_S n_0\left(N_S - N_{S0}^-\right) & (4.3) \\ 0 = N_{D0}^- + N_{S0}^- + n_0 - N_A & (4.4) \end{cases}$$

$$\begin{cases} \dfrac{dN_{D1}^-}{dt} = -\left(q_{D,L}s_{D,L}I_{L0} + q_{D,H}s_{D,H}I_H\right)N_{D1}^- - q_{D,L}s_{D,L}mI_{L0}N_{D0}^- \\ \quad + \gamma_D n_1\left(N_D - N_{D0}^-\right) - \gamma_D n_0 N_{D1}^- + \zeta_D N_{S1}^- + \zeta'_D\left(N_{S1}^- + N_{D1}^-\right) & (4.5) \\ \dfrac{dN_{S1}^-}{dt} = -\left(q_{S,L}s_{S,L}I_{L0} + q_{S,H}s_{S,H}I_H\right)N_{S1}^- - q_{S,L}s_{S,L}mI_{L0}N_{S0}^- \\ \quad + \gamma_S n_1\left(N_S - N_{S0}^-\right) - \gamma_S n_0 N_{S1}^- - \zeta_S N_{S1}^- - \zeta'_S\left(N_{S1}^- + N_{D1}^-\right) & (4.6) \\ \dfrac{-iK}{e} j_1 = \left(\dfrac{dN_{D1}^-}{dt} + \dfrac{dN_{S1}^-}{dt} + \dfrac{dn_1}{dt}\right) & (4.7) \\ j_1 = e\mu n_0 E_1 - ik_B T\mu K n_1 + \left(\kappa_{D,L}I_{L0} + \kappa_{D,H}I_H\right)N_{D1}^- + \kappa_{D,L}mI_{L0}N_{D0}^- \\ \quad + \left(\kappa_{S,L}I_{L0} + \kappa_{S,H}I_H\right)N_{S1}^- + \kappa_{S,L}mI_{L0}N_{S0}^- & (4.8) \\ \dfrac{iK}{e}E_1 = \dfrac{N_{D1}^- + N_{S1}^- + n_1}{\varepsilon\varepsilon_0} & (4.9) \end{cases}$$

where all the parameters are defined in Table 2.1 with shallower and deeper traps referring to Fe and Mn traps, respectively. We have modified Equation (4.5) and

Equation (4.6) from their original form in two-center recording by adding two terms to each equation corresponding to the electron tunneling effect. For example in Equation (4.6), the first term added ($-\zeta_S N_{S1}^-$) represents the redistribution of the electrons from the regions with higher concentration to the regions with lower concentration. This term models the large-scale effect of the tunneling as an extra diffusion term in Equation (4.6). The second term [$-\zeta'_S (N_{S1}^- + N_{D1}^-)$] in Equation (4.6) represents the redistribution of the electron concentration in Fe traps by the means of electron tunneling in the presence of an electrical potential. This corresponds to the large-scale drift effect of the tunneling in the presence of the electric field. The space-charge electric field is proportional to the summation of the electron concentrations in the two traps [Equation (4.8)]. Therefore, the electric potential is also proportional to the total electron concentration as represented in Equation (4.6). The proper sign is considered to model the movement of the electrons to a lower energy states. The constants ζ_S and ζ'_S are proportional to the tunneling probability of electrons in the Fe traps. For the crystals with lower Fe concentrations, the probability of tunneling is negligible, and therefore, these constants are zero. Also, these constants can be functions of recording parameter. For example, the effect of the existence of vacant neighboring sites for tunneling can be considered as a proportional factor of $(1 - N_{S0}^- / N_{Fe})$ in ζ_S and ζ'_S, where N_{Fe} is the total Fe concentration.

The two terms added to Equation (4.5) are similar to those added to Equation (4.6) and they represent the diffusion and the drift effects of the electron tunneling from the Fe traps to the Mn traps. Different constants (ζ_D and ζ'_D) are used for these terms since the probability of tunneling from Fe sites to Mn sites is lower than that for tunneling between Fe sites. We assume the relation between the tunneling constants for the two traps to be

$$\zeta_D = \frac{(N_{Mn} - N_{D0}^-)}{(N_{Fe} - N_{S0}^-)} \zeta_S , \tag{4.10}$$

$$\zeta'_D = \frac{(N_{Mn} - N_{D0}^-)}{(N_{Fe} - N_{S0}^-)} \zeta'_S , \tag{4.11}$$

where N_{Mn} is the total Mn concentration. In the Equations (4.10) and (4.11) we simply assume the probability of tunneling is proportional to the vacant neighboring sites as mentioned before.

We now solve the set differential equations using numerical method in Mathematica with the initial conditions of $N_{D0}^-(t=0) = N_{Mn}/2$, $N_{S0}^-(t=0) = 0$, $N_{D1}^-(t=0) = 0$, and $N_{S1}^-(t=0) = 0$. Half of the Mn traps are assumed to be filled with electrons at the beginning of the recording while all the Fe traps are empty. We assume the variation of the electron concentration in the conduction band (n) is instantaneous compared to the variation of the other variables (adiabatic approximation). We also assume that the electron concentration in the conduction band is negligible compared to the electron concentrations in Fe and Mn traps. Figure 4.5 shows the diffraction efficiency as a function of time when we solve the equations for the experimental condition used to obtain Figure 4.1. The values used for ζ_S and ζ'_S are 2.5×10^{-4} sec^{-1} and 2.1×10^{-3} sec^{-1}, respectively, and are obtained by parameter fitting to match the experimental data. As it is seen in the figure, the diffraction efficiency increases after the recording when the hologram is kept in dark. This increase is in agreement with the experimental results observed in Figure 4.2.

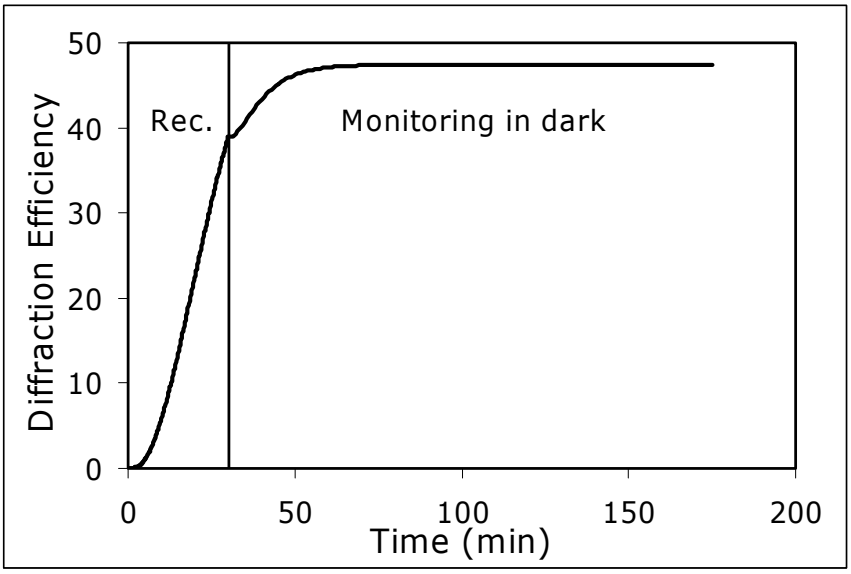

Figure 4.5. Simulation results for the dynamics of the diffraction efficiency during recording and monitoring in dark when the hologram is recorded using the green beams. The model used in the simulation is explained in the text. All the parameters for the simulation are chosen from experimental parameters used to obtain of Figure 4.1.

Figure 4.6 shows the results when the hologram is recorded using two red beams. All the other parameters are the same as those used to obtain the experimental results of Figure 4.3. In this case the diffraction efficiency of the hologram is reduced after the recording when it is kept in the dark. For this simulation we used the values 2×10^{-5} sec^{-1} and 1×10^{-4} sec^{-1} for ζ_S and ζ'_S, respectively. In this case the tunneling effect tends to reduce the diffraction efficiency after the recording. It should be noted that exact simulation of the results presented in Figure 4.2 and 4.3 is not pursued here. Instead, we have developed a model that can predict different phenomena we observed in the experiments with reasonable assumptions.

The different behaviors observed for recording with green and red beams are caused by the difference between the tunneling processes in these two cases. The space-charge field that is built up during the recording and the average concentration of the vacant

neighboring sites are different in these two cases, so is the probability of electron tunneling. This change results in an increase or a decrease in the diffraction efficiency of the hologram when it is monitored in dark after the recording. The exact change of the tunneling probability for recording at different wavelengths is very complicated and cannot be modeled easily. We have considered this effect as the change in the constants ζ_D and ζ'_D in our model.

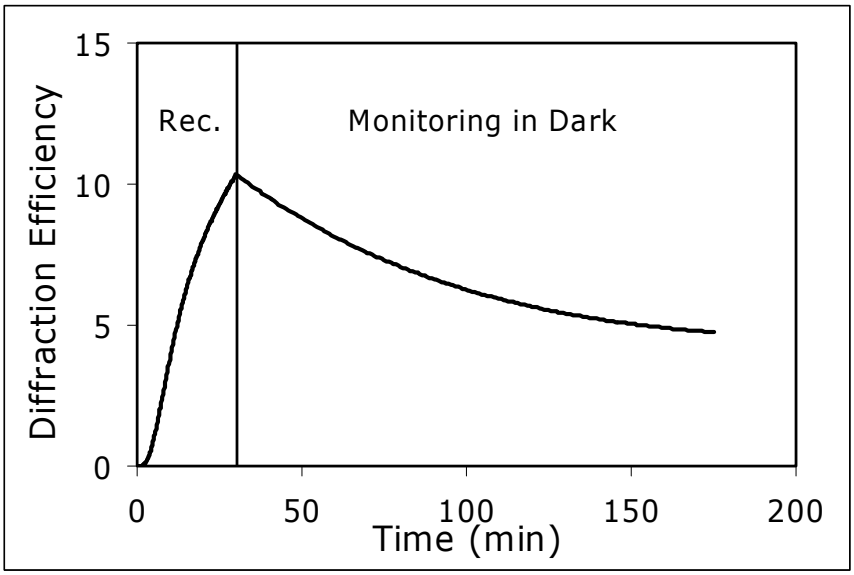

Figure 4.6. Simulation results for the dynamics of the diffraction efficiency during recording and monitoring in dark when the hologram is recorded using the red beams. The model used in the simulation is explained in the text. All the parameters for the simulation are chosen from experimental parameters used to obtain of Figure 4.1.

It should be mentioned that the effect of the tunneling in two-center recording is completely different from that in one-center recording. The space-charge field in two-center recording is built up from the electron concentration in the two traps (N_{S1}^{-} and N_{D1}^{-}). The tunneling effect redistributes the modulated electron concentration in the Fe traps (N_{S1}^{-}) in a way that the electrons move to the lower energy states. During this

process, the modulated electron concentration in Mn traps (N_{D1}^{-}) is almost unchanged. As the N_{S1}^{-} changes, the total space-charge field and the electric potential change in a way that the electrons in Fe traps are redistributed to occupy the lower energy state. In this movement the relative phase shift between N_{S1}^{-} and the electric potential reaches 180º, at which the probability of tunneling reduces considerably. However in one-center recording, the space-charge field is built up only by the modulate electron concentration in the Fe traps. As the tunneling effect redistributes the electrons, the modulated electron concentration changes but its phase shift relative to the phase to the space-charge electric field and the electric potential remains unchanged. Therefore, the tunneling process continues to eventually erase the hologram completely.

4.4 Conclusion

The two-center holographic recording in highly doped $LiNbO_3$:Fe:Mn was investigated in detail in this section. The evidence of electron tunneling in a $LiNbO_3$:Fe:Mn crystal doped with high Fe concentration was presented for the first time. We experimentally showed that the electron concentration in $LiNbO_3$:Fe:Mn can increase the diffraction efficiency even when the hologram is kept in dark. This effect has not been reported to date for any hologram recorded in lithium niobate crystals. Based on the physical phenomena involved in the process, we modeled the electron tunneling in two-center recording. The set of Kukhtarev's equations for two-center recording was modified to include the electron tunneling. In this model, we consider the electron tunneling between the Fe sites and from Fe sites to Mn sites, while the latter has a smaller probability. The large-scale effect of the tunneling is represented as drift and diffusion terms in the two-

center model that mostly modifies the electron distribution in Fe traps. This effect can result in either an increase in the diffraction efficiency or a decrease when we change the tunneling probabilities for recording at different wavelengths. We also observed different tunneling behavior in the experiments when we used red beams and green beams to record the hologram. The exact variation of the tunneling probability with different recording condition is difficult to obtain and can be a topic of further research in this area.

While the electron tunneling in one-center recording always causes the dark erasure of the holograms, as we mentioned, the effect in two-center recording can either erase or enhance the hologram after the recording without any external illumination. In one-center recording the space charge electric field is built up only from the electron distribution in Fe. When the tunneling changes this distribution, the electric field is also changed accordingly and the hologram is erased completely. However, in two-center recording, the space-charge electric field is a function of the electron distribution in both Fe and Mn traps. During the tunneling, the electron distribution in Fe traps is changed while the electron distribution in Mn is almost fixed. Therefore, the relative phase between the modulated electron concentration in Fe and the electric potential can have a completely different variation in two-center recording compared to that in one-center recording. This is the main reason that electron tunneling can result in an increase in the diffraction efficiency in two-center recording. This unique feature of the tunneling effect in two-center recording might be found useful for some applications of photorefractive material.

Chapter 5

Thermal Fixing in Two-Center Holographic Recording

5.1 Introduction

Thermal fixing is a well-known fixing process that can be used for extending the dark storage time of holograms recorded in photorefractive crystals [16, 18-20]. In general, the complete thermal fixing process consists of two main steps: fixing and developing. Fixing is accomplished during or after the holographic recording by heating the crystal to a higher temperature (usually above 100 °C for $LiNbO_3$:Fe). The mobility of positive ions (usually H^+) in the photorefractive crystals is a function of temperature and by raising the temperature the ionic mobility increases. Thus, the ions move to compensate the electron distribution at high temperature. In the developing phase, the crystal is cooled down to room temperature and then illuminated with a uniform developing beam. At room temperature, the mobility of protons (H^+) decreases by several orders of magnitude compare to that at high temperature. Therefore, the ionic pattern remains fixed at room temperature. During the development, homogenous illumination excites the modulated concentration of electrons and generates modulated currents [16, 18-20]. The modulated electronic pattern is reduced and, therefore, the space charge field is built up. We refer to this process as low-high-low thermal fixing or simply L-H-L process. Figure 5.1 shows temporal variation of the space-charge field during a typical L-H-L thermal fixing in a singly doped $LiNbO_3$:Fe. The hologram is first recorded for t_1 second. Then, the hologram is kept at high temperature to let the protons move and compensate the

distribution of electronic grating. At last, the temperature is reduced and the hologram is developed using a beam with uniform intensity. Developing ratio is defined as the ratio of the electric field at the end of the developing phase to that value at the end of the recording phase (E_1/E_2).

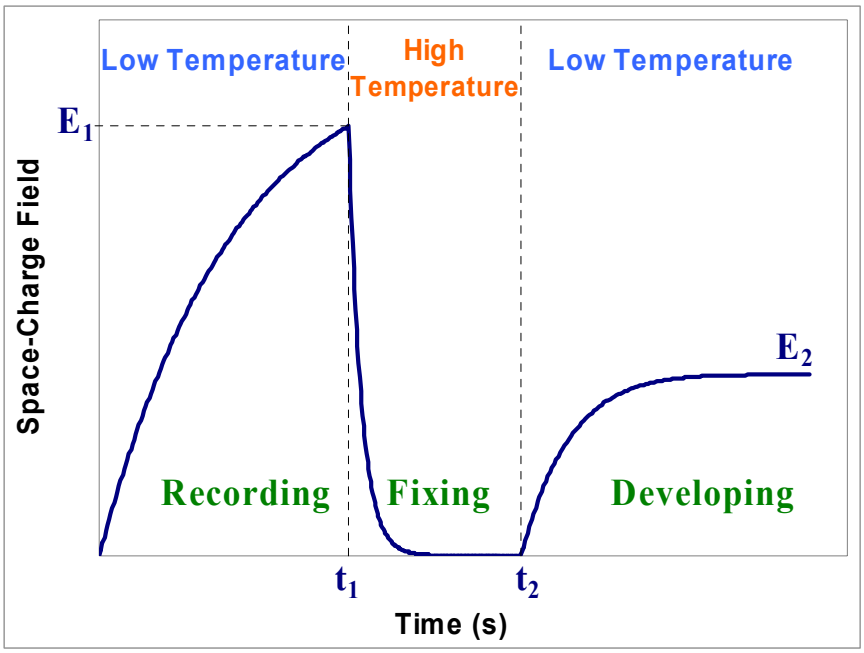

Figure 5.1. Temporal behavior of the space-charge field during a typical L-H-L thermal fixing in a singly doped $LiNbO_3$:Fe crystal. At low temperature the hologram is recorded until the space charge field reaches the value E_1. The hologram is then heated in dark and the protons compensate the electron distribution resulting in a very small space-charge electric field. The hologram is then illuminated with a beam with uniform intensity at low temperature to reveal the hologram stored by the proton distribution. The developing ratio is defined as E_1/E_2.

The thermal fixing is based on the idea that the proton migration occurs at high temperatures, while the protons are not mobile at low temperature. On the other hand, the electron grating can be recorded at either low or high temperature [16, 64]. In $LiNbO_3$:Fe the dominant recording mechanism is the bulk photovoltaic effect that moves electrons in the conduction band to redistribute the electronic pattern. As soon as the modulated electronic concentration is formed in the crystal, an electric field builds up that induces a drift current. The drift current is in the opposite direction compared to the bulk

photovoltaic current. Therefore, the space-charge field tends to reduce the effective recording current in the conduction band. If the recording is performed at high temperature, the protons migrate to compensate the electronic charge pattern during the recording. As a result, the space-charge field will be reduced. Therefore, the preventing force will decrease and the hologram can be recorded up to a higher strength. When the crystal is cooled to the room temperature, the illumination with a beam with uniform intensity (developing beam) reveals a fixed hologram formed by the protons, which can have high diffraction efficiency. We refer to this process as High-Low thermal fixing or in the short from H-L process. The success of the H-L thermal fixing depends on stability of the recording process at high temperature, successful compensation of the electron charge distribution by protons at high temperature, and efficient developing process at low temperature.

Although the L-H-L thermal fixing process provides a longer dark decay for the recorded holograms, it is not very interesting for two-center recording. Two-center recording, by itself, provides persistent storage of the holograms. We only use the L-H-L process to investigate the properties of the fixing and the developing phases of thermal fixing in two-center recording. The results will be used for designing the parameters in the H-L thermal fixing, which can potentially improve the dynamic range of the material, especially for applications requiring fixed (non-erasable) holograms. Examples of these applications are holographic add-drop filters and diffractive optical elements. The reason that we use the H-L process with the two-center recording and not with the one-center recording is that particular applications can be achieved only using two-center recording. For example, the localized recording that has applications in holographic storage and

pattern recognition [35, 65] can be only realized in two-center recording. Therefore, the H-L thermal fixing is potentially useful for such applications.

We use the two-center model of Chapter 2 and modify it to theoretically investigate the thermal fixing process in $LiNbO_3$:Fe:Mn in Section 5.2. In Section 5.3 we present the theoretical results and discuss the possible improvement obtained using H-L process. In Section 5.4 we introduce our experimental setup to perform thermal fixing in $LiNbO_3$:Fe:Mn. Some experimental results are also presented and discussed in this section. The concluding remarks are made in Section 5.5.

5.2 Theoretical model for thermal fixing in two-center recording

We use the two-center model in Section 2 and modify it to include the effect of movement of the protons. The effect of temperature and the contribution of proton migration are added to the set of two-center equations similar to the method used from one-center recording in Ref. [16]. Again, we assume a sinusoidal variation of the recording intensity, *i.e.* $I_L=I_{L0}[1+m\cos(Kx)]$, and consider the first two terms in the spatial Fourier series of all variables, *i.e.* $N_D = N_{D0}^- + N_{D1}^- \exp(-iKx)$. We can write the two sets of zeroth and first order equations as

$$\begin{cases} \dfrac{dN_{D0}^-}{dt} = -\left(q_{D,L}s_{D,L}I_{L0} + q_{D,H}s_{D,H}I_H + \beta_D\right)N_{D0}^- + \gamma_D n_0\left(N_D - N_{D0}^-\right) & (5.1) \\ \dfrac{dN_{S0}^-}{dt} = -\left(q_{S,L}s_{S,L}I_{L0} + q_{S,H}s_{S,H}I_H + \beta_S\right)N_{S0}^- + \gamma_S n_0\left(N_S - N_{S0}^-\right) & (5.2) \\ 0 = N_{D0}^- + N_{S0}^- + n_0 - N_A - n_{i0} & (5.3) \end{cases}$$

$$\frac{dN_{D1}^{-}}{dt} = -\left(q_{D,L}s_{D,L}I_{L0} + q_{D,H}s_{D,H}I_H + \beta_D\right)N_{D1}^{-} - q_{D,L}s_{D,L}mI_{L0}N_{D0}^{-} + \gamma_D n_1\left(N_D - N_{D0}^{-}\right) - \gamma_D n_0 N_{D1}^{-} \tag{5.4}$$

$$\frac{dN_{S1}^{-}}{dt} = -\left(q_{S,L}s_{S,L}I_{L0} + q_{S,H}s_{S,H}I_H + \beta_S\right)N_{S1}^{-} - q_{S,L}s_{S,L}mI_{L0}N_{S0}^{-} + \gamma_S n_1\left(N_S - N_{S0}^{-}\right) - \gamma_S n_0 N_{S1}^{-} \tag{5.5}$$

$$\frac{dn_{i1}}{dt} = \frac{iK}{e}\left(e\mu_i n_{i1}E_0 + e\mu_i n_{i0}E_1 + ik_B T\mu_i K n_{i1}\right) \tag{5.6}$$

$$\frac{-iK}{e}j_1 = \left(\frac{dN_{D1}^{-}}{dt} + \frac{dN_{S1}^{-}}{dt} + \frac{dn_1}{dt}\right) \tag{5.7}$$

$$j_1 = e\mu n_0 E_1 - ik_B T\mu K n_1 + \left(\kappa_{D,L}I_{L0} + \kappa_{D,H}I_H\right)N_{D1}^{-} + \kappa_{D,L}mI_{L0}N_{D0}^{-} + \left(\kappa_{S,L}I_{L0} + \kappa_{S,H}I_H\right)N_{S1}^{-} + \kappa_{S,L}mI_{L0}N_{S0}^{-} \tag{5.8}$$

$$\frac{iK}{e}E_1 = \frac{N_{D1}^{-} + N_{S1}^{-} + n_1 - n_{i1}}{\varepsilon\varepsilon_0} \tag{5.9}$$

where n_i is the total concentration of protons (or ions) and has an average of n_{i0} and a modulated component of n_{i1}, μ_i is the mobility of the protons, β_D and β_S are thermal excitation rates for electron excitation from deeper and shallower traps, respectively, and all the parameters are defined in Table 2.1.

The changes that we made in the original set of two-center equation are as follows. Thermal excitation of the electrons from the deeper and the shallower traps is considered in Equations (5.1), (5,2), (5.4) and (5.5). Equation (5.6) is added to include the drift and the diffusion currents for protons. The Poisson equations [Equation (5.3) and (5.9)] are modified to also include the contribution of protons. The other equations are not changed

from their original forms. We can solve the set differential equations using numerical method in Mathematica with a set of initial conditions of $N_{D0}^{-}(t=0)=N_A$, $N_{S0}^{-}(t=0)=0$, $N_{D1}^{-}(t=0)=0$, $N_{S1}^{-}(t=0)=0$, and $n_{i1}=0$.

5.3 Analysis of thermal fixing in $LiNbO_3$:Fe:Mn

For thermal fixing in $LiNbO_3$:Fe:Mn, we use the model we developed in the last section, while the mobility of the protons and electrons is assumed to be a function of temperature. The values for the mobility at different temperatures are found from the literature [64, 66]. We only include the thermal excitation terms at high temperature and use the values from Ref. [64]. Before doing the analysis of thermal fixing in two-center recording, we verify the model by putting the concentration of the Mn dopants equal to zero and compare the results with thermal fixing in one-center holographic recording [16, 66]. After testing the model, we use it to find the variation of the developing ratio with different parameters of the model. Also we use the model to investigate the improvement we can expect in the dynamic range when we use H-L thermal fixing.

In two-center recording, we consider two different cases for the developing phase. In the first case, the developing beam is one of the recording beams and can excite electrons mainly from the shallower trap (*e.g.* red beam). In the second case, the developing beam is the sensitizing beam and can excite electrons from both shallower and deeper traps (*e.g.* UV beam). We also assume that the developing beam is at a single frequency to simplify the analysis. We found that the developing intensity affects the speed of the developing process and does not affect the developing ratio in both the cases. Also, for the practical range of the parameters, we found that a high developing ratio can be

achieved by using a beam that can excite from both traps (*e.g.* UV intensity). However, for an actual set of parameters, the developing ratio might be small and it would be more efficient if we use the beam that excites from the shallower traps only. Figure 5.2 shows the variation of the developing ratio with the ratio of the electron concentration to the Mn concentration (N_A/N_{Mn}) for UV and red developing beams. It is seen in this figure that for the small values of N_A/N_{Mn} we can achieve developing ratios more than 50%. However, for the practical cases, the value of N_A/N_{Mn} is usually more than 0.5 and using the red developing beam results in a larger developing ratio.

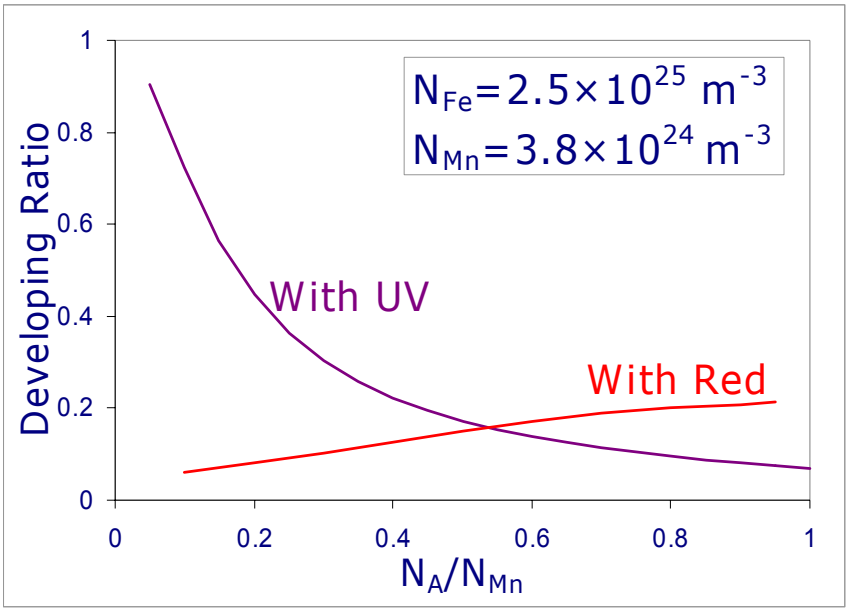

Figure 5.2. Variation of developing ratio with the total electron concentration normalized to Mn concentration. The concentration of Fe and Mn dopant are 2.5×10^{25} m^{-3} and 3.8×10^{24} m^{-3}, respectively. The developing ratio is for developing beams at UV and red.

We can find an analytic formula for developing ratio for the case that the developing beam can excite from both traps (*e.g.* UV beam) based on the model for thermal fixing. We assume that the beam is at wavelength λ, and the total electron concentration (N_A)

and Mn concentration (N_{Mn}) are much less than Fe concentration. The developing ratio would be

$$\frac{E_2}{E_1} = \frac{i\left(\frac{\kappa_{Fe,UV} I_{UV}}{e\mu n_0}\right)}{\left[\frac{e}{\varepsilon\varepsilon_0 K} + i\left(\frac{\kappa_{Fe,UV} I_{UV}}{e\mu n_0}\right)\right]} \tag{5.10}$$

where κ_{Fe} is bulk photovoltaic coefficient for Fe at UV, I_{UV} is the total intensity of the developing beam, N_A is the total electron concentration, e is the electron charge, μ is the electron mobility, n_0 is the average electron concentration in the conduction band, $\varepsilon\varepsilon_0$ is the primitivity of the material, K is the grating vector, and E_1 and E_2 are the space charge fields before the fixing phase and after the developing phase, respectively. Since n_0 is proportional to I_{UV}, the developing efficiency is independent of the intensity of the developing beam as we mentioned before. Also, n_0 is proportional to the total electron concentration (N_A). Decreasing N_A will decrease n_0, and therefore, increase the developing ratio. This is in agreement with the result of the simulation for UV developing beam shown in Figure 5.2. Also, from Equation (5.10) it is found that the wavelength of the developing beam should be selected in a way that the photovoltaic constant of Fe (κ_{Fe}) becomes as large as possible.

Figure 5.3 shows the L-H-L thermal fixing dynamics in two-center recording. The concentration of Mn and Fe are 5.0×10^{25} m^{-3} and 6.5×10^{23} m^{-3}, respectively. Initially, 80% of the Mn traps are filled with electrons and all the Fe traps are empty. The total concentration of ions is assumed to be 10^{24} m^{-3}. The total intensity of the recording beams is the same as the intensity of the sensitizing beam ($I_{Red}/I_{UV} = 1$). The thickness of the

crystal is 1 mm. The polarization of the recording beams is ordinary. Since the developing efficiency is about 0.27, the final efficiency is below the value that can be achieved without thermal fixing (also shown in this figure). From Figure 5.3, it is clear that in general diffraction efficiency in two-center recording does not gain from L-H-L thermal fixing, as it is also the case in one-center recording.

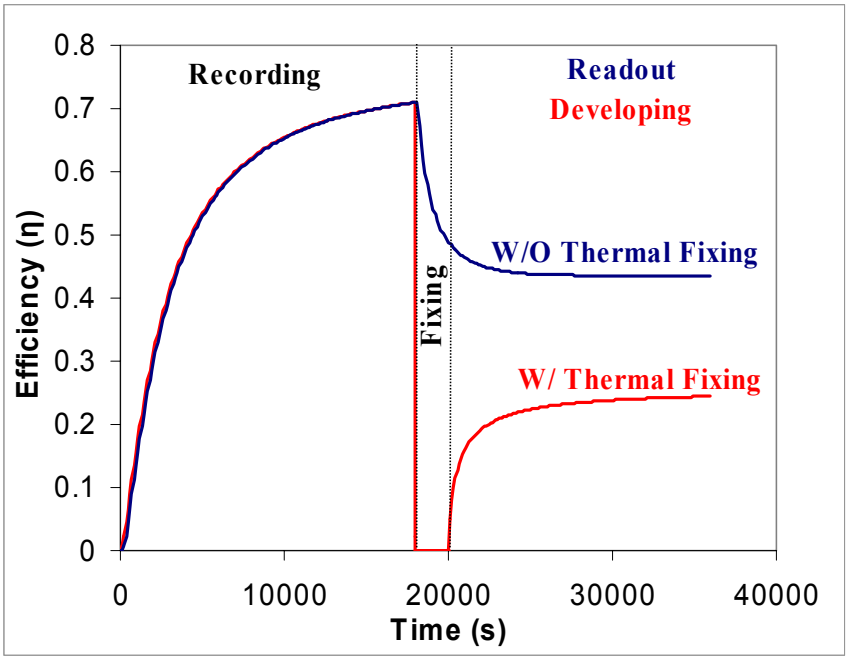

Figure 5.3. Diffraction efficiency with and without L-H-L thermal fixing in two-center recording. The recording is for a 1 mm thick $LiNbO_3$:Fe:Mn crystal. Fe and Mn concentrations are 5.0×10^{25} m^{-3} and 6.5×10^{23} m^{-3}, respectively. Initially 80% of the Mn traps are field. The ratio of the total recording intensity to the sensitizing intensity is one. Thermally fixed hologram is developed using UV 365 nm beam.

We repeat the same simulation for the H-L thermal fixing. All the parameters are the same as described above for the L-H-L case. The result is shown in Figure 5.4. During the recording, protons compensate the electronic pattern and the net space charge field would be almost zero. Therefore, there would be no effective hologram in this phase. During the developing phase, the space charge field is built up by uniformly redistributing the electron concentration. The final space-charge field would be more than

what can be achieved in recording at low temperature as shown in Figure 5.4. Therefore, there is a good potential of getting higher diffraction efficiency by recording the hologram at high temperature.

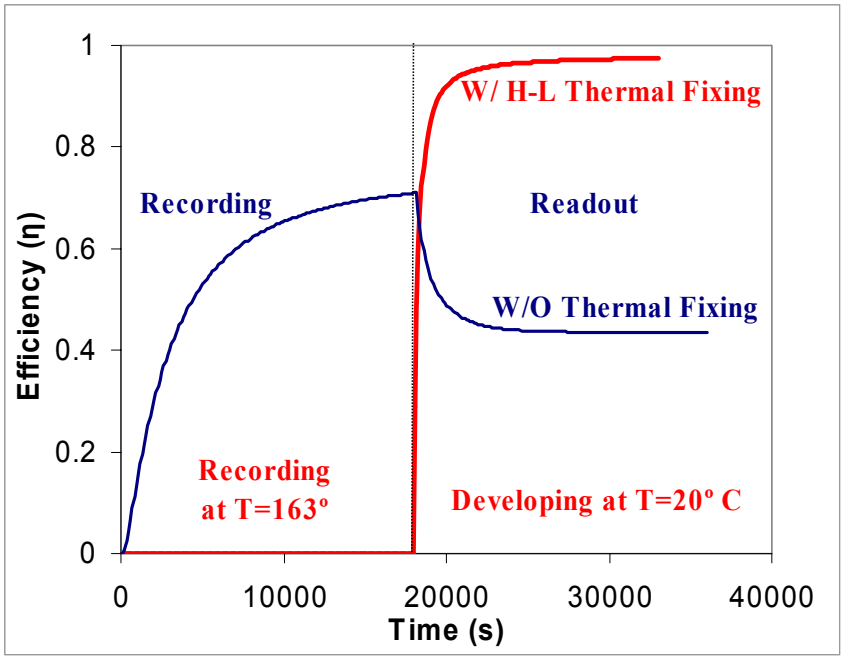

Figure 5.4. Diffraction efficiency with and without H-L thermal fixing in two-center recording. All the parameters are the same as described in the caption of Figure 5.3.

To find the improvement in the dynamic range (*M*/#) that can be gained by recording at high temperature we find the maximum value of the *M*/# using H-L thermal fixing and compare it with that value for ordinary two-center recording. We consider three sets of wavelengths for recording and sensitizing beams: recording at 633 nm and sensitizing at 365 nm; recording at 633 nm and sensitizing at 404 nm; and recording at 532 nm and sensitizing at 404 nm. In each case we develop the crystal at low temperature using a beam with the same wavelength as that of the sensitizing beam. The results are summarized in Table 5.1. The improvement factors of 1.4 or more are gained in all the cases.

Table 5.1. The improvement in dynamic range (*M*/#) using H-L thermal fixing.

Maximum *M*/# (mm^{-1})	Red (633 nm) and UV (365 nm)	Red (633 nm) and Blue (404 nm)	Green (514 nm) and Blue (404 nm)
Without Thermal Fixing	**0.76**	**0.89**	**2.14**
High-Low Thermal Fixing	**1.4**	**1.87**	**2.9**
Improvement Factor	**1.8**	**2.1**	**1.4**

It should be noted that for the results in Table 5.1, the sensitizing beam is used as the developing beam for H-L thermal fixing process. The optimum parameters for getting a high developing ratio are different than that for getting high hologram strength. Therefore, since we can choose the developing beam independent of the recording process, we can find a proper condition for the developing beam to get a high developing ratio for strong holograms. Simple calculations show that by using a developing beam at a proper wavelength, there would be at least a factor of two further improvement in *M*/# for high temperature recording. All these results suggest that recording at high temperature would increase the *M*/# in two-center recording while we get the advantage of storing a hologram formed by proton distribution and has a long dark decay.

5.4 Experiment

In this section we explain the experiments for thermal fixing in two-center recording. The thermal fixing setup is based on the setup of Figure 3.1, while the non-polarizing beam splitter (NPBS) and the crystal are placed inside a vacuum chamber (cryostat) as shown in Figure 5.5. The cryostat is an Optistat DNV from Oxford Instruments and is used to keep the crystal in a very low-pressure (less than 10 mbar) atmosphere when it is heated to high temperature. The low-pressure atmosphere suppresses the change in the beam

phase from the air convection around the crystal. Four glass windows around the cryostat provide access to the crystal.

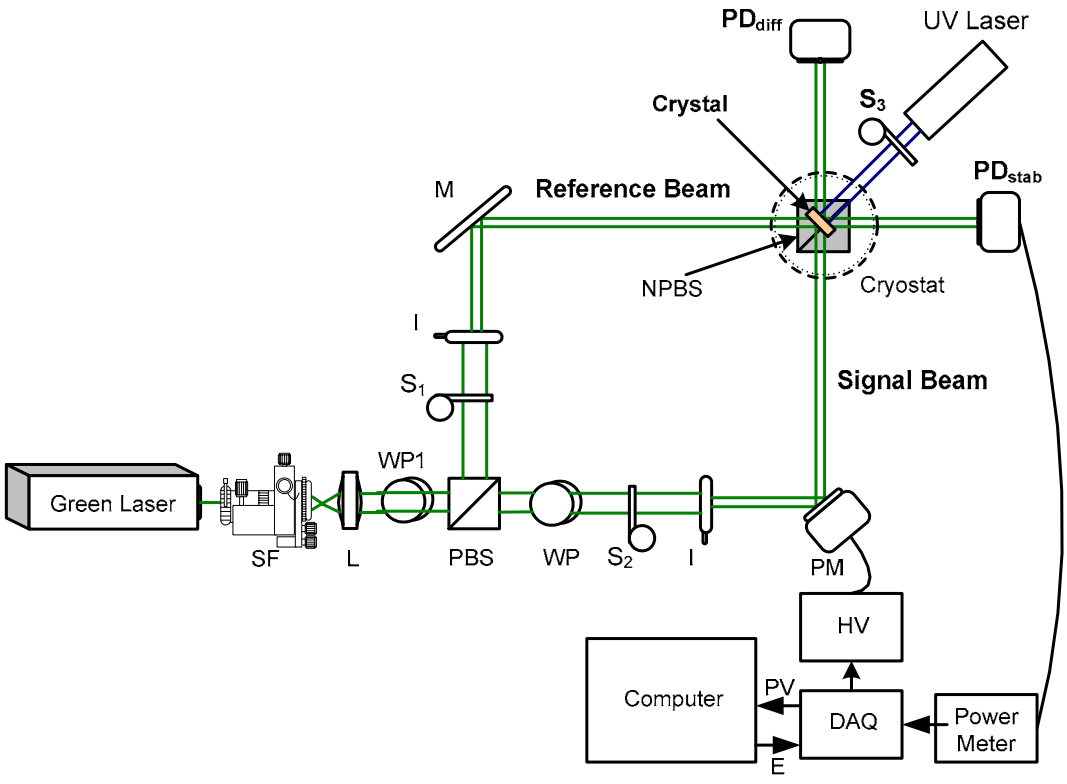

Figure 5.5. The stabilized recording setup used for thermal fixing experiments. The non-polarizing beam splitter (NPBS) and the crystal are placed inside a vacuum chamber (cryostat). The crystal is heated from the top using an electrode inside the cryostat. All the other parameters are the same as those explained in the caption of Figure 3.1.

The crystal is heated from the top using an electrode inside the cryostat. The crystal is completely attached to the electrode using thermal conducting compound (Arctic Silver 5). The beam splitter is separated from the crystal by isolating paper. This provides a firm connection between the two elements needed for stabilizer system while they are thermally isolated. The temperature of the crystal is controlled using an ITC 502 temperature controller from Oxford Instrument. Using this controller, the temperature can be set from 45 K to 495 K with a tolerance of less than 0.1 K. However, for low

temperature the cryostat should be connected to a liquid nitrogen source, which is not of interest in the context of this article.

Figure 5.6 shows the H-L-H thermal fixing using the 2 mm thick $LiNbO_3$:Fe:Mn crystal doped with 0.15 wt.% Fe_2O_3 and 0.02 wt.% MnO. Before the experiment, the crystal was oxidized in oxygen atmosphere at 1070º C for 48 hours. The wavelength of the recording beams was 532 nm. The blue sensitizing beam was at the wavelength of 404 nm. The total intensity of the recording beams and the sensitizing beam were 12 mW/cm^2 and 10 mW/cm^2, respectively. The hologram was recorded for 30 minutes and then was read at room temperature. After about 24 minutes the heating process was started while the hologram was still in Bragg condition. The maximum temperature was 130º C and the hologram was monitored during this process as shown in the figure. After that the crystal was cooled down to room temperature (22º C) and monitored in dark to make sure the Bragg condition is met. After 30 minutes the hologram was illuminated with the blue beam with the intensity of 10 mW/cm^2 for 60 minutes. As it is seen in the beginning of the developing phase, all the electrons in the heating process were not completely compensated; therefore, the blue beam erases the rest of hologram with a relatively fast rate. However, no hologram is developed as we kept illuminating the crystal with the blue beam.

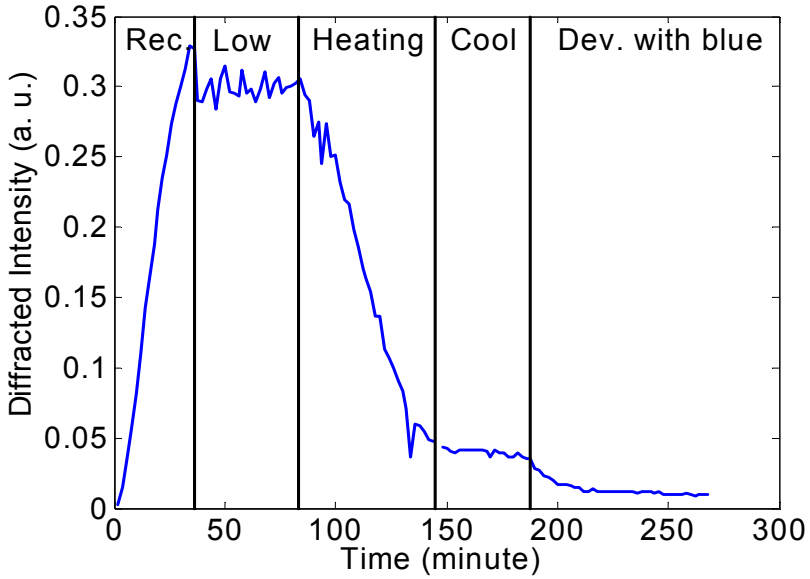

Figure 5.6. The H-L-H thermal fixing process in $LiNbO_3$:Fe:Mn crystal. The wavelength of the recording beams was 532 nm. The blue sensitizing beam was at the wavelength of 404 nm. The total intensity of the recording beams and the sensitizing beam were 12 mW/cm^2 and 10 mW/cm^2. The high temperature was 130º C. The hologram is developed at room temperature (22ºC) using the sensitizing blue beam.

The experiment was repeated using recording beams with the total intensity of 17 mW/cm^2. In this experiment, one of the recording beams (green beam) is used to develop the hologram. The result is shown in Figure 5.7. Again, the hologram was recorded for 30 minutes and then heated to 130º C after monitoring in dark for 10 minutes. The hologram was at high temperature for about 90 minutes. The crystal was then cooled down to room temperature and developed with the green beam for 80 minutes. Again, no significant developing ratio was observed in this experiment.

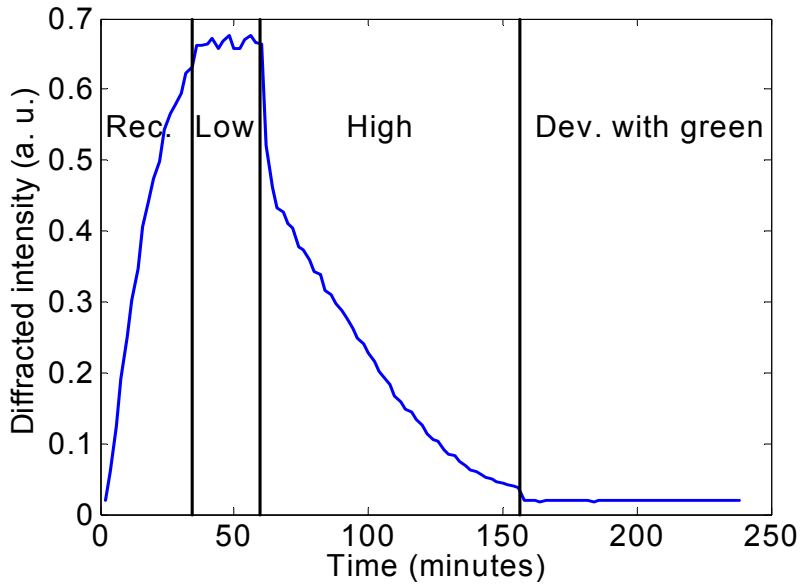

Figure 5.7. The H-L-H thermal fixing process in $LiNbO_3$:Fe:Mn crystal in the case that one of the recording beams is used to develop the hologram. The total intensity of the recording beam was 17 mW/cm^2. All the other parameters are the same as those in the caption of Figure 5.6.

We repeated the experiments several times and the same result for developing ratio was obtained. In another set of experiments, we performed H-L thermal fixing in the $LiNbO_3$:Fe:Mn sample. Again, no significant developing ratio was observed. We repeated both H-L-H and H-L thermal fixing using recording beams at the wavelength of 633 nm. We used both the blue beam and the red recording beam for developing the hologram. In these cases, we did not observe any significant development either. All the experiments, at different recording wavelengths, were repeated in another $LiNbO_3$:Fe:Mn sample. This sample was a 0.86 mm thick $LiNbO_3$:Fe:Mn doped with 0.075 wt.% Fe_2O_3 and 0.02 wt.% MnO with no oxidization treatment. Again, no significant value for developing ratio was obtained.

Based on all these experiments we conclude that some unknown effect might be present during the thermal fixing in the $LiNbO_3$:Fe:Mn that does not allow efficient developing at the end of the process. It should be mentioned a recent work on the thermal

fixing in $LiNbO_3$:Mn shows that the H-L-H process cannot be successfully performed on this material since the developing ratio is very small [62]. The developing ratio measured for thermal fixing in $LiNbO_3$:Mn in that work is 0.01. We believe the poor developing ratio we observed in our experiment and also in $LiNbO_3$:Mn is from the unknown properties of the Mn dopant. One possible effect can be the excitation of holes from the Mn traps to the valence band at high temperature. In this case, the hologram is erased before the protons have the chance to compensate it and there would be no hologram to be developed in the developing phase. The investigation of the actual cause of low developing ratio in the crystals having Mn dopant can be considered as a separate project and is explained in the future work in Chapter 9.

5.5 Conclusion

The idea of thermal fixing in two-center recording is investigated in this chapter. We developed the model for thermal fixing in two-center recording that can be used for theoretical investigation. We showed theoretically that recording at high temperature and then developing at low temperature can result in an improvement in the dynamic range of the material. During the recording at high temperature, the protons migrate to compensate the electronic charge pattern. Therefore, the space-charge field is reduced and the preventing force is decreased. As a result, the modulated electron concentration can be recorded with larger amplitude that results in a higher dynamic range for the hologram after the development. We found that a factor 1.4 or more improvement can be obtained in *M*/# using the high temperature recording in $LiNbO_3$:Fe:Mn.

Several thermal fixing experiments were performed in $LiNbO_3$:Fe:Mn. Two different samples were used. Also, different experiments were performed using recording beams at different wavelengths (532 nm and 633 nm). The developing phase was also investigated using the sensitizing beam and one of the recording beams for each experiment. In all the cases, very small developing ratio is observed. Also, the thermal fixing in $LiNbO_3$:Mn is reposted with very small developing ratio in literature [62]. The observation of inefficient developing phase in these cases cannot be explained based on the available models for thermal fixing. It might be related to an unknown property of the Mn dopant. Although the thermal experiment in $LiNbO_3$:Fe:Mn is not successful, the idea of high temperature recording and the model are general and can be used for other doubly doped crystal.

Chapter 6

Multi-Grating Method for Analysis and Design of Volume Holographic Elements

6.1 Introduction

In this Chapter, we describe an efficient model for the design and analysis of general volume holograms. This method is based on Born approximation and the plane wave expansion of a complicated recording beam. The method can be used to analyze and design a wide range of holographic elements and provides and in depth understanding of the properties of these components. While the numerical simulation can be easily implemented based on this method, closed form solution can be obtained in particular cases. The closed from solution further reduces the design time and effort and improves the understanding of the problem. Complex problems that cannot be analyzed numerically can be solved with the closed form solution.

In particular, we use the multi-grating method for designing holographic dispersive elements as spectral diversity filters (SDFs) in this chapter. A SDF maps a homogeneous but diffuse spectral source onto a spatially encoded pattern. Measuring the output light intensity over the output plane by a detector array (for example a CCD camera) and inverting the spectral-spatial mapping enables spectral estimation [67]. In contrast with conventional spectroscopy, however, throughput losses using SDFs may be independent of spectral resolution. We show the initial results for the design of the SDF based on a

spherical beam volume hologram (SBVH). The dispersion properties of the SBVH are derived based on our method and compared with the experimental results.

We first describe, in Section 6.2, multi-grating method for modeling volume holograms and their diffraction properties. While the method can be used for a hologram recorded with a plane wave and an arbitrary beam, we develop and explain it based on the SBVH as a practical case. Using the multi-grating method, we analyze the major properties of a new class of holographic SDFs in Section 6.3 and compare those results with experimental data in Section 6.4. Further discussions of the method and the holographic SDFs are presented in Section 6.5, and final conclusions are made in Section 6.6.

6.2 Analysis of volume holograms using multi-grating method

In general, the multi-grating method can be used for any hologram recorded by the interference pattern of an arbitrary coherent beam and a plane wave or even two arbitrary beams. This approach can be used for finding the diffracted beam from the hologram when read by a plane wave at any wavelength. The model can be further extended to analyze the case for an arbitrary reading beam. To understand and implement the method for a practical application, we explain it for diffraction analysis of a SBVH. The proof of this approach is presented in the Appendix C for a hologram recorded using a plane wave and an arbitrary coherent beam.

The interference pattern of a plane wave and a spherical beam (from a point source) records a SBVH as shown in Figure 6.1(a).

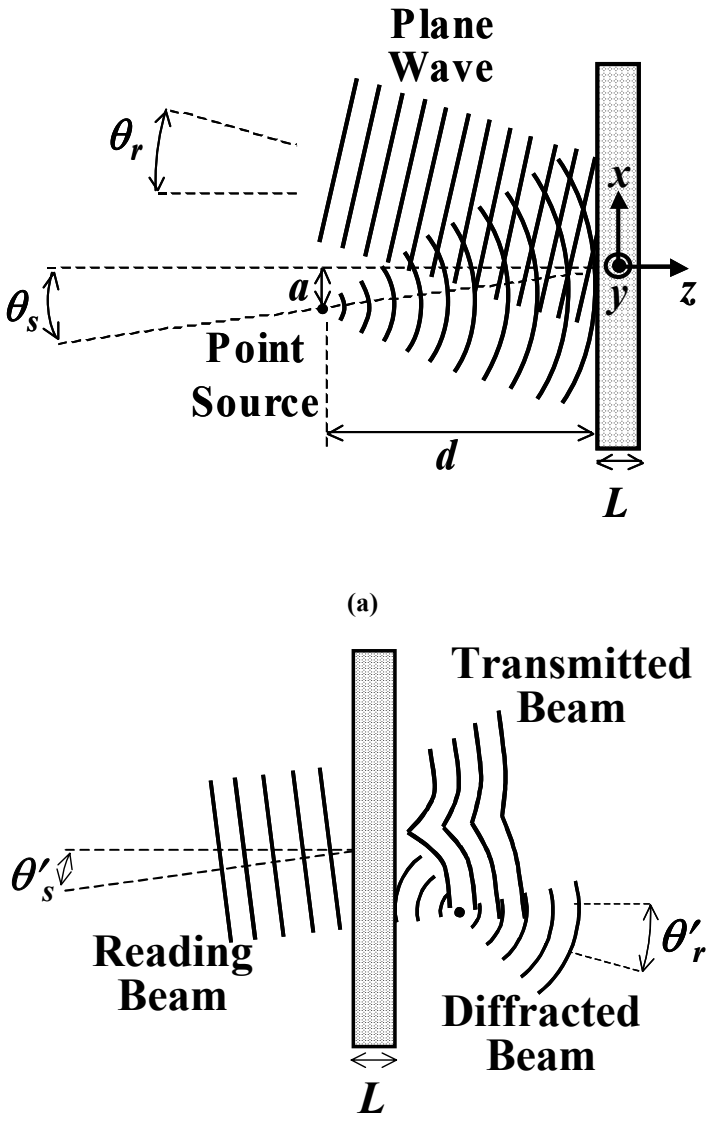

Figure 6.1. (a) Recording geometry for a spherical beam volume hologram. The point source is at distance *d* from the center of the crystal. The reference beam incident angle is θ_r. A line from the coordinate origin to the point source makes angle θ_s with the *z*-axis. (b) Reading configuration. A collimated beam reads the hologram with θ'_s incident angle. Note that the direction of the reading beam corresponds to the direction of the signal beam in recording configuration. The diffracted beam propagates in a direction that makes angle θ'_r with the *z*-axis. The thickness of the holographic material is *L* in both cases.

The recording medium has a thickness of L in the z-direction. It is assumed that the transverse dimensions of the recording material are very large compare to L. The point source located at $\mathbf{r}_0 = (-a, 0, -d)$ is formed using a lens with high numerical aperture

(NA). The vector $\mathbf{r}_0$ makes an angle θ_s with the z-axis. Therefore, a is equal to $d\cdot\sin(\theta_s)$ in Figure 6.1(a). The reference beam is a plane wave with an incident angle θ_r with respect to z-axis. Both recording beams are at wavelength λ with TE polarization (*i.e.* electric field normal to the incident x-z plane).

To analyze the SBVH recorded in the medium, we first expand the spherical beam at distance $\mathbf{r} = (x, y, z)$ from the point source at $\mathbf{r_0} = (-a, 0, -d)$ as a set of plane waves [68]:

$$\frac{1}{|\mathbf{r}-\mathbf{r}_0|}e^{jk|\mathbf{r}-\mathbf{r}_0|} = \frac{j}{2\pi}\iint\frac{1}{k_z}e^{jk_z(z+d)}e^{jk_x a}\ e^{j(k_x x+k_y y)}dk_x dk_y\ , \qquad (6.1)$$

where k_x, k_y, and k_z are the x-, y-, and the z-components of the wave vector $\mathbf{k}$, respectively. The magnitude of the wave vector is shown by k. In the expansion of Equation (6.1), each component is a plane wave propagating in the direction of unit vector $\hat{\mathbf{a}}_\mathbf{p}$ given by

$$\hat{\mathbf{a}}_\mathbf{p} = \frac{k_x}{k}\hat{\mathbf{x}} + \frac{k_y}{k}\hat{\mathbf{y}} + \frac{\sqrt{k^2-k_x^2-k_y^2}}{k}\hat{\mathbf{z}}\,, \qquad (6.2)$$

where, in general, $\hat{\mathbf{u}}$ indicates the unit vector in the u-direction. The constant amplitude and phase of each plane wave component are given by

$$A(k_x,k_y) = \frac{j}{2\pi\sqrt{k^2-k_x^2-k_y^2}}e^{jk_x a}e^{jk_z d}\ . \qquad (6.3)$$

Note that in Equation (6.1), the integrations are, in general, over all the possible values of k_x and k_y. However, for the values of $|k_x| > k$ or $|k_y| > k$, the z-component of the propagating vector becomes imaginary, which represents an evanescent wave. The

evanescent wave whose amplitude decades rapidly with z can be neglected in the estimation of the integral. Thus, the integrals in Equation (6.1) essentially take the same values whether they are performed over a circle of radius k (*i.e.*, $k_x^2 + k_y^2 \le k^2$) or over the entire k_x-k_y plane (*i.e.* from -∞ to +∞). Therefore, we omit the range of the integrals through this chapter.

The interference of each plane wave component (traveling in the direction $\hat{\mathbf{a}}_\mathbf{p}$) with the reference plane wave records a hologram inside the medium. If we represent the wave vector components of the spherical beam with (k_x, k_y, k_z) and the incident plane wave with (k_{rx}, 0, k_{rz}) = (k sin(θ_r), 0, k cos(θ_r)), the effect of the interference pattern on the dielectric constant of the medium can be represented as

$$\varepsilon(r) = \varepsilon_0 + \Delta\varepsilon(k_x, k_y)\, e^{j\mathbf{K}_g \cdot \mathbf{r}} + \text{c.c.}, \tag{6.4}$$

where the grating vector $\mathbf{K}_g = (k_{rx} - k_x)\hat{\mathbf{x}} + (-k_y)\hat{\mathbf{y}} + (k_{rz} - k_z)\hat{\mathbf{z}}$.

The modulation term, $\Delta\varepsilon$, is proportional to the amplitudes of the two recording plane waves (the reference beam and a plane wave component of the signal beam) and, therefore, it is proportional to $A(k_x, k_y)$. Note that in this analysis, we assume that the absorption of the recording and the reading beam is weak. Figure 6.1(b) shows the reading geometry that is used for holographic SDFs. Note that the reading beam replaces the spherical beam (and *not* the plane wave reference beam). We assume that during readout the hologram is illuminated with an approximately collimated beam at wavelength λ′. The direction of propagation of the reading beam makes an angle θ'_s with the z-axis as shown in Figure 6.1(b). The main direction of the propagation of the diffracted beam makes an angle θ'_r with the z-axis. In case λ = λ′ and $\theta_s = \theta'_s$ (*i.e.*, Bragg-

matched readout) the diffracted beam is in the direction of the reference beam as shown in Figure 6.1(b), *i.e.*, $\theta'_r = \theta_r$.

To find the diffracted beam from a SBVH, we have to add the diffracted beams from all different gratings. Since the wavelength of the reading beam is, in general, different from the recording wavelength, the dual wavelength method [24] can used to analyze the diffraction from each grating. The *k*-space representations of the recording and reading configurations are shown in Figures 6.2(a) and 6.2(b), respectively.

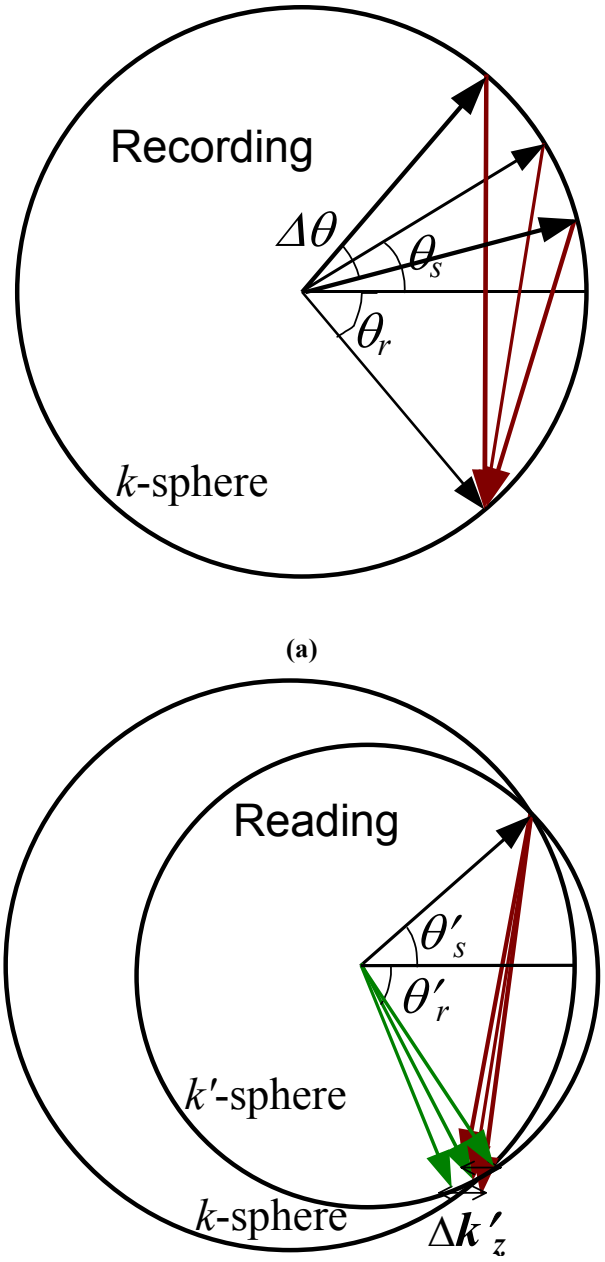

Figure 6.2. (a) Recording configuration represented in the *k*-domain. The major angular extent of the spherical beam is indicated by $\Delta\theta$ in the *k*-domain. (b) Reading configuration in the *k*-domain. In general, the reading wavelength is different from the recording one. $\Delta k'_z$ is a measure of partial Bragg-matched condition. All other parameters are the same as those in Figure 6. 1.

The amplitude of each diffracted beam component is found using Born's approximation as in Ref. [69] with reading wavelength (in general) different from the

recording wavelength. The validity of Born's approximation for these calculations is justified since each plane wave component causes a low index modulation. Also, we do not expect large and abrupt change in the index modulation in the space domain. Different components of the diffracted beam will be added to find the total output beam. Using Born approximation, the electric field of the diffracted beam from each hologram component is [69]

$$\widetilde{E}_d\left(k_x,k_y,z\right)=\frac{j\Delta\varepsilon k'^2 L}{2\varepsilon_0 k'_{dz}}e^{j(K_{gx}+k'_{sx})x}e^{j(K_{gy}+k'_{sy})y}e^{jk'_{dz}z}\mathrm{sinc}\left[\frac{L}{2\pi}\left(K_{gz}+k'_{sz}-k'_{dz}\right)\right], \quad (6.5)$$

where the propagation vector of the reading beam is assumed to be (k'_{sx}, k'_{sy}, k'_{sz}) with magnitude k', and $\mathrm{sinc}(u) \equiv \sin(\pi u)/(\pi u)$. In the configuration shown in Figure 6.2(b), the reading beam has a propagation vector of ($k'\sin(\theta'_s)$, 0, $k'\cos(\theta'_s)$). Note that in general $k' = 2\pi/\lambda'$ is different from $k = 2\pi/\lambda$, where λ and λ' are recording and reading wavelengths, respectively. The z-component of the diffracted beam, k'_{dz}, can be found from

$$k'_{dz}=\sqrt{k'^2-(K_{gx}+k'_{sx})^2-(K_{gy}+k'_{sy})^2}\ , \quad (6.6)$$

while substituting for K_{gx} results in

$$k'_{dz}=\sqrt{k'^2-(k_{rx}+k'_{sx}-k_x)^2-(k'_{sy}-k_y)^2}\ . \quad (6.7)$$

Note that each holographic grating is represented by one set of (k_x, k_y) in the plane-wave expansion of the recording signal beam. Combining all the diffraction beam components, the output (diffracted beam) is given by

$$E_d(x,y,z) = \iint \widetilde{E}_d\left(k_x,k_y,z\right)dk_x dk_y \,. \tag{6.8}$$

Let's define $\widetilde{E}'_d(k_x,k_y,z)$ as

$$\begin{aligned}\widetilde{E}'_d\left(k_x,k_y,z\right) &= 4\pi^2\widetilde{E}_d\left(k_x,k_y,z\right)e^{j(k_x x+k_y y)}e^{-j(k_{rx}+k'_{sx})x}e^{-jk'_{sy}y} \\ &= \frac{j2\pi^2\Delta\varepsilon k'^2 L}{\varepsilon_0 k'_{dz}}\exp\left(jk'_{dz}z\right)\mathrm{sinc}\left[\frac{L}{2\pi}\left(K_{gz}+k'_{sz}-k'_{dz}\right)\right] \quad ,\end{aligned} \tag{6.9}$$

then the integral in Equation (6.8) can be represented as the inverse Fourier transform of $E'_d(k_x, k_y, z)$ as:

$$E_d\left(x,y,z\right) = \frac{e^{j(k_{rx}+k'_{sx})x}e^{jk'_{sy}y}}{4\pi^2}\iint \widetilde{E}'_d\left(k_x,k_y,z\right)e^{-j(k_x x+k_y y)}dk_x dk_y \,, \tag{6.10}$$

or

$$E_d\left(x,y,z\right) = e^{j(k_{rx}+k'_{sx})x}e^{jk'_{sy}y}\mathcal{F}^{-1}\left\{\widetilde{E}'_d\left(k_x,k_y,z\right)\right\}\Big|_{\substack{x\to -x\\ y\to -y}} \,, \tag{6.11}$$

where $\mathcal{F}^{-1}$ represents the inverse Fourier operation.

6.3 Analysis of spherical beam volume holograms as SDFs

When a SBVH is read by a collimated beam with angle θ'_s with respect to the z-axis, the diffracted beam can be found by combining Equations (6.9) and (6.11). Note that the recorded hologram is represented by the change in the dielectric constant, $\Delta\varepsilon$. We substitute $\Delta\varepsilon$ for the SBVH in Equation (6.9) and expand k_z and k'_{dz} in term of small x- and y-components of $\mathbf{k}$ and $\mathbf{k}_d$ using binomial expansion (paraxial approximation). We

also assume $z << d$ and neglect the small variations for the amplitude because of $1/k'_{dz}$ term in Equation (6.9). All these assumptions are valid for practical implementation of SDFs using SBVHs. Using these approximations, the output-diffracted beam can be simplified as

$$E_d(x,y,z) = C_1 \mathcal{F}^{-1}\left\{ e^{jk_x a} e^{-\frac{j}{2k}\left(k_x^2+k_x^2\right)d} \operatorname{sinc}\left[\left(K_{gz}+k'_{sz}-k'_{dz}\right)\frac{L}{2\pi}\right]\right\}\Bigg|_{x\to -x,\, y\to -y}, \quad (6.12)$$

where C_1 is a complex constant that includes all terms independent of k_x, k_y, x, or y. The phase factor outside the integral in Equation (6.12) (the phase of C_1) does not affect the spatial intensity distribution of the diffracted beam right after the hologram. Thus, we do not explicitly consider it in the rest of our derivation (they are still included in C_1). This closed form inverse Fourier transform can be found approximately by using the properties of Fresnel transform [70]. For simplicity we show the approach for the case that the reading beam is normal to the hologram (*i.e.*, $\theta'_s = 0$ or $k'_{sx} = k'_{sy} = 0$). For more general case, the approach is the same but more algebraic manipulations are needed. Rewriting Equation (6.12) in terms of the inverse Fourier transform integral and representing every parameter in terms of k_x and k_y, we find:

$$E_d(x,y,z) = C_2 \iint \exp\left\{-j\frac{kd}{2}\left[\left(\frac{k_x}{k}-\frac{x-a}{d}\right)^2+\left(\frac{k_y}{k}-\frac{y}{d}\right)^2\right]\right\} \operatorname{sinc}\left[\left(K_{gz}+k'-k'_{dz}\right)\frac{L}{2\pi}\right]\frac{dk_x}{k}\frac{dk_y}{k}, \quad (6.13)$$

where C_2 is another complex constant. The integral in Equation (6.13) is the Fresnel transform with parameter $\alpha = kd/2$ [70]. For α with very large absolute value (*i.e.*, $|\alpha| \to \infty$), the Fresnel transform of a function becomes the function itself with proper change of variable. In Equation (6.13), the integrand has a non-zero value for $|k_x/k| \le 1$ and $|k_y/k| \le 1$ and rapidly goes to zero for $|k_x/k| > 1$ or $|k_y/k| > 1$ as we discussed before. Therefore, α is very large [typically $d >> \lambda$ in Figure 6.1(a)] compare to the integration variables. Therefore, as an approximate solution, the result of the integral in Equation (6.13) is the *sinc* function with integration variables k_x/k and k_y/k replaced by $(x - a)/d$ and y/d, respectively, *i.e.*,

$$E_d(x,y,z) \approx C_3 \operatorname{sinc}\left[f\left(\frac{x-a}{d}, \frac{y}{d}\right)\frac{L}{2\pi}\right] \ , \tag{6.14}$$

where again C_3 is another complex constant and the function $f(u, v)$ is

$$f(u,v) = k_z + k' - k\sqrt{1-u^2-v^2} - k\sqrt{\frac{k'^2}{k^2} - \left(\frac{k_{rx}}{k} - u\right)^2 - v^2} \ . \tag{6.15}$$

For the simple case of $\lambda = \lambda'$, and for $u << 1$ and $v << 1$ we have

$$f(u,v) \approx \frac{k}{2}\left[1 + \frac{1}{\cos(\theta_r)}\right]\left\{\left[u - \frac{\sin(\theta_r)}{1+\cos(\theta_r)}\right]^2 + v^2 - \left[\frac{\sin(\theta_r)}{1+\cos(\theta_r)}\right]^2\right\}. \tag{6.16}$$

Note that in Equation (6.16), we have used $k_{rx} = k \sin(\theta_r)$ and $k_{rz} = k \cos(\theta_r)$.

It is clear from Equation (6.14) that the diffracted beam intensity is maximum when the argument of the *sinc* function [and thus, $f(u,v)$] is zero. The minimum intensity is zero and it occurs when $f(u,v) = 2\pi m/L$, with m being a non-zero integer.

From the definition of the function $f(u, v)$, given by Equation (6.15), it is clear that the loci of the points with a constant diffracted intensity (for example maximum or zero) is a circle. If we only consider the diffracted signal in the main lobe of the *sinc* function in Equation (6.14), the diffracted beam will resemble an annulus whose intensity is maximum at the center and goes to zero at the edges at which $f(u,v) = 2\pi m/L$ for $m = \pm 1$.

Figure 6.3(a) shows the theoretical calculations of the pattern of the diffracted beam (at the back face of the hologram) of a spherical beam hologram recorded using the setup in Figure 6.1 with d = 1.6 cm, λ = 532 nm. The holographic material is assumed to have a refractive index of 1.5 and a thickness of 100 μm. The angles θ_r and θ_s are chosen to be 45º and 0º, respectively. For these calculations, we assumed the dimensions of the holograms in x and y directions to be 1.5 cm and 1.5 cm, respectively. A normal incident-beam at 700 nm wavelength reads the hologram. The coordinate origin is shown by **O** in Figure 6.3. Dashed lines represent corresponding output region for a hologram with practical dimensions of 3.5 mm × 3.5 mm. The diffracted pattern from this smaller size SBVH is shown in Figure 6.3(b). It is clear that because of the smaller size of the hologram, only a portion of the diffracted annulus (which we call a crescent) appears in the output.

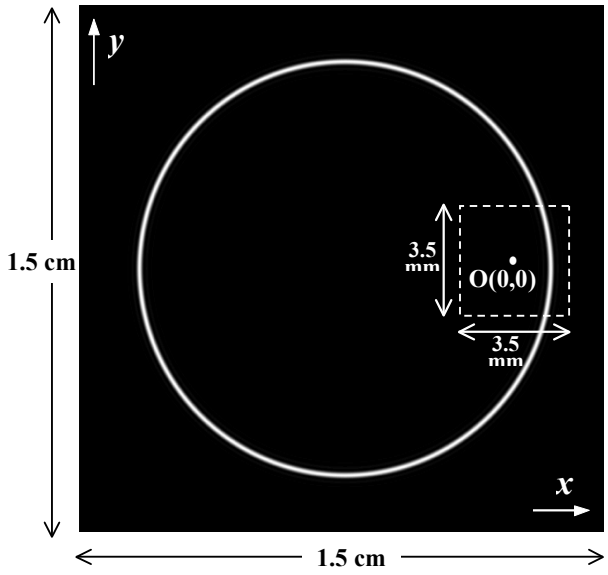

(a)

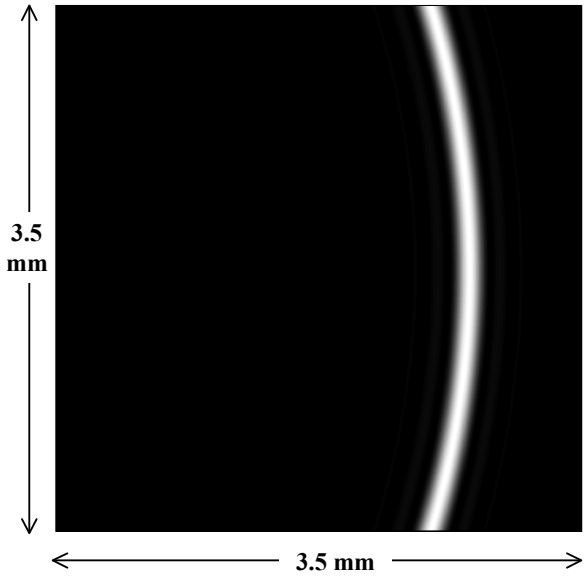

(b)

Figure 6.3. (a) Theoretical calculations of the pattern of the diffracted beam of a spherical beam volume hologram recorded using the set up in Figure 6.1 with d = 1.6 cm and λ = 532 nm. The angles θ_r and θ_s are chosen to be 45° and 0°, respectively. The holographic material is assumed to have a refractive index of 1.5 and a thickness of 100 μm. For these calculations, we assumed the dimensions of the holograms in x and y directions to be 1.5 cm and 1.5 cm, respectively. The hologram is read using a beam with normal incident (i.e. propagation along z-axis) at wavelength 700 nm. The origin of the coordinate system is shown by O. (b) The diffracted beam pattern of the same spherical beam volume hologram as in (a) but with lateral dimensions of 3.5 mm × 3.5 mm. The corresponding hologram is shown by dashed line in (a).

Using Equations (6.14) we can determine several properties of the diffracted crescent. For example, the width of the crescent can be calculating by putting $y = 0$ and finding the distance between the zeros of the main lobe of the *sinc* function in Equation (6.14). For the case of identical recording and reading wavelengths, the result is

$$w = \frac{2d\lambda}{L}\cot(\theta_r). \tag{6.17}$$

If we consider the refractive index of the holographic recording material to be n, we can write the width of the crescent as

$$w_a = \frac{2\left[d - \frac{L}{2}\left(1 - \frac{1}{n}\right)\right]\lambda_a}{L}\cot(\theta_{r,inside}), \tag{6.18}$$

where subscript a means the parameter measured in the air. The reference angle (θ_r) should be measured inside the material for Equation (6.18).

The location of the center of the crescent (maximum intensity) also depends on the reading wavelength, λ'. For example, at $y = 0$ plane, the crescent is located at

$$x = \frac{a}{d} + \sqrt{\frac{2k_r'(k - k_{rz} - k' + k_r')}{k(k + k_r')} + \frac{k_{rx}^2}{(k + k_r')^2}}\,. \tag{6.19}$$

Note that k' and k_r' are functions of reading wavelength, λ'. This wavelength dependence of the location of the crescent is the main factor in SBVHs for making SDFs. Figure 6.4 shows the diffracted crescent calculated using different reading wavelengths of 532, 630, and 700nm with normal incident angle. All other parameters are the same as

those used for Figure 6.3. The wavelength dependency of the location of the crescent is clearly seen in Figure 6.4. The transmitted beam field pattern (E_t) can be also calculated by subtracting the diffracted field pattern (E_d) from the incident beam pattern ($E_{s'}$), *i.e.*, $E_t = E_{s'} - E_d$.

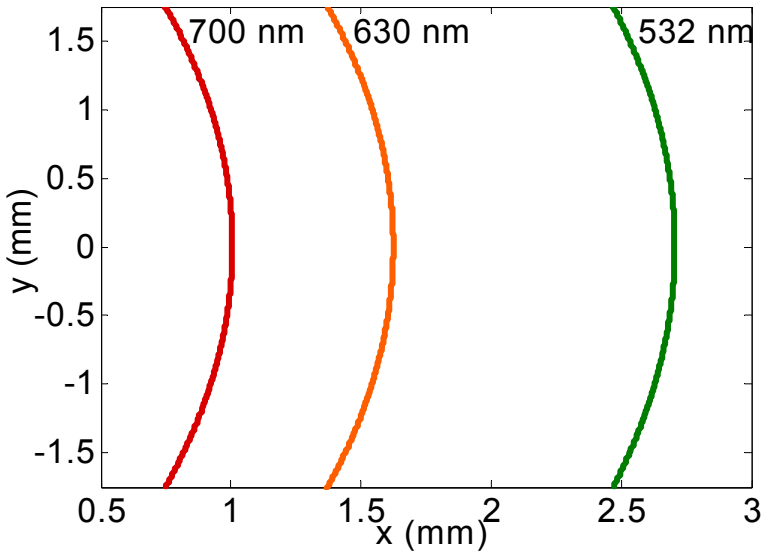

Figure 6.4. Different crescents for reading with different wavelengths of 532, 630, and 700nm. All other parameters are the same as those described in the caption of Figure 6.3(b).

In order to calculate the exact value of the field, we can find the inverse Fourier transform in Equation (6.11) numerically. We use two-dimensional inverse fast Fourier transform (IFFT) in MATLAB® with adequate sampling rate to verify the approximated approach. We found that the exact numerical results agree very well with the approximate results derived earlier. Even using the numerical computation, the method we use for estimating the diffraction is more efficient than the conventional Born approximation [71] from computational point of view. Our method gives the diffracted beam all over the desired output plane by getting only one integral that can be easily implemented using efficient inverse Fourier transform techniques such as IFFT. Also, in comparison to other

numerical approaches, the multi-grating method uses the minimal number of diffraction orders; therefore, large problems can be solved with reasonable memory requirement. Also, since the method is based on Born approximation (in contrast to coupled wave analysis [9]), the limited lateral size of the hologram can be taken into account in the calculation to obtain accurate results for holograms with small lateral size.

6.4 Experimental results

To investigate the properties of the SBVHs for spectroscopy and to check the validity of theoretical results obtained using the proposed method, we recorded several transmission geometry SBVHs using the setup in Figure 6.1(a). The recording material was Aprilis photopolymer [72]. The thicknesses of the samples used were 100 μm, 200 μm, or 300 μm. The recording wavelength was 532 nm. The values of θ_s and θ_r were –9.6º and 44º, respectively. These angles were selected to allow the operation of the SDF with the normal incident angle at a reading wavelength around $\lambda' = 800$ nm. The distance of the point source to the hologram (d) varied in the range from 1.6 cm to 12 cm for different holograms. The polarization of both recording beams was TE.

To investigate the performance of SBVHs as spectral diversity filters, we read each hologram with reading beams at different wavelengths, using the setup in Figure 6.1(b). For each reading beam, we monitor both the diffracted beam (diffracted at an angle θ'_r and focused on a screen) and the transmitted beam (at the back-face of the hologram using a zoomed CCD camera). The spectral diversity of the diffracted beam can be monitored by reading the hologram with white light. Figure 6.5(a) shows the diffracted beam from a SBVH that is illuminated by an approximately collimated white

light beam (from a regular 60 W lamp) from the direction of the spherical recording beam (*i.e.*, $\theta'_s \cong -10^o$). The white screen is about 20 mm from the hologram. It is clear that different wavelength channels (or colors) of the incident beam are separated at this output plane.

Figure 6.5(b) shows the transmitted beam through a SBVH when illuminated by a collimated beam at $\lambda' = 700$ nm at normal incident angle ($\theta'_s = 0^o$). The incident light is obtained by passing a white light beam through a monochromator with aperture size of 0.45 mm. The full-width half-maximum of the output spectrum of the monochromator at 700 nm wavelength is about 3 nm. The output beam of monochromator is collimated using a collimating lens. The dark crescent in the transmitted beam resembles the diffracted crescent discussed in Section 6.3. The shape of this dark crescent is defined by Bragg selectivity of the SBVH in the *x*-direction in Figure 6.1(b). The position of the crescent depends on the incident wavelength and on the incident angle. By reading the hologram with a collimated white light source, several color crescents appear in the transmitted beam. This is shown in Figure 6.6. The color of each crescent corresponds to the reduction of a diffracted crescent at a specific wavelength from the incident white light.

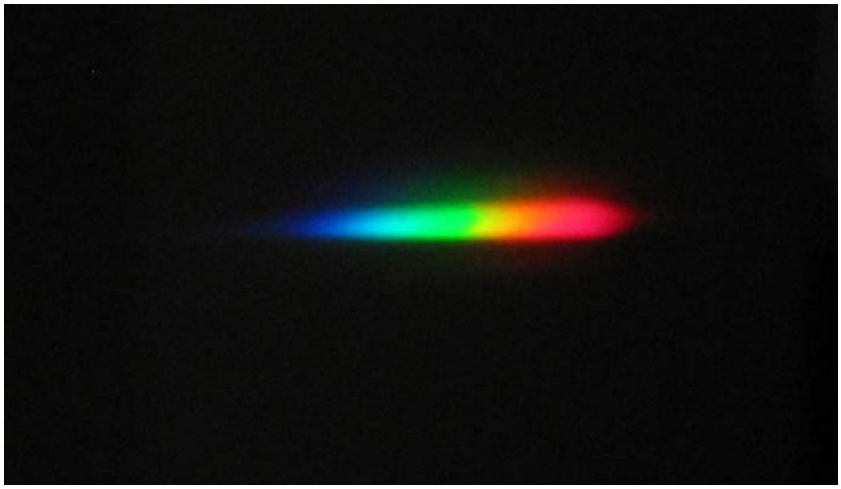

(a)

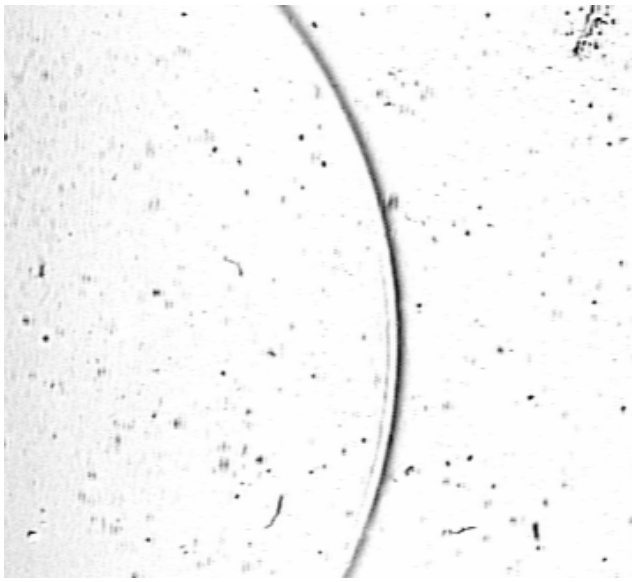

(b)

Figure 6.5. (a) The diffracted beam from a spherical beam volume hologram illuminated by an approximately collimated white light beam from the direction of the spherical recording beam. The white light is from a regular 60 W lamp. The white screen is about 20 mm from the hologram. The hologram is recorded using the set up in Figure 6.1 with d = 1.6 cm and λ = 532 nm. The holographic material is Aprilis photopolymer with refractive index of 1.5 and a thickness of 100 μm. The angles θ_s and θ_r in the recording setup are –9.6º and 44º, respectively. (b) The transmitted beam through the spherical beam volume hologram when illuminated by a collimated beam at λ = 700 nm at normal incident angle (θ'_s = 0º). The reading light is obtained by passing a white light beam through a monochromator with output aperture size of 0.45 mm. The full-width half-maximum of the output spectrum of the monochromator at 700 nm wavelength is about 3 nm. The output of the monochromator is collimated using a collimating lens. The dark crescent in the transmitted beam is clearly seen. The dots in the figure correspond to the imperfection in the material.

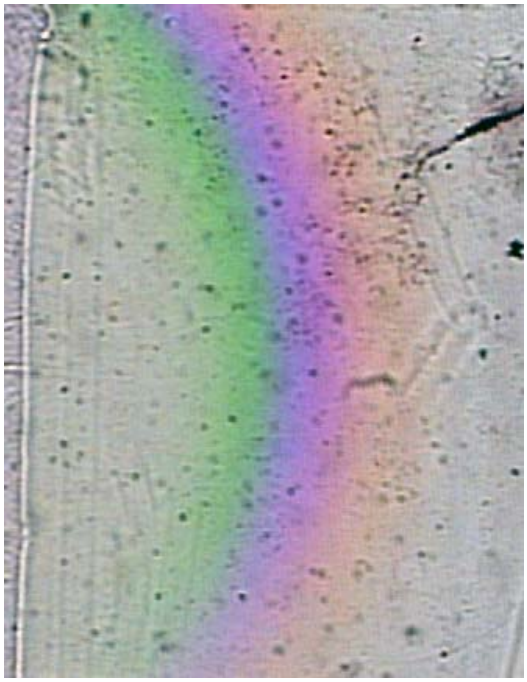

Figure 6.6. The transmitted beam through the spherical beam volume hologram when read by an approximately collimated white light beam from the direction of the spherical recording beam. The hologram is the same as those described in the caption of Figure 6.5(a).

For quantitative measurements, we define two measures for the dark crescent seen in the output. The first measure is the width of the crescent, which is defined as the distance between the edges of the dark crescent at the back face of the hologram in the x-direction at $y = 0$. This measure is directly related to the resolution of the spectrometer. The thinner the crescent, the finer the wavelength resolution of the spectrometer will be. The other measure is the curvature of the crescent. This measure helps us to characterize the expected shape of the detecting signal. It also gives us the information that is useful for designing rotation-multiplexed spherical beam holograms [8].

Figure 6.7(a) shows the variation of the crescent width with the distance between the point source and the recording material during recording (*i.e.*, d). The experimental results were obtained by recording 5 holograms at $\lambda = 532$ nm for 5 different values of d and reading them at both $\lambda' = \lambda = 532$ nm (squares) and $\lambda' = 830$ nm (diamonds). The

variations associated with the measurements are also shown as the corresponding error-bars. The error-bars represent the range of crescent widths measured at different heights of each crescent (*i.e.*, different value of y in Figure 6.4) close to the crescent center (y = 0). We have also shown in Figure 6.7(a), the theoretical variations of the crescent width with d, using our theoretical model. The difference between theory and experiment is less than 7%. The limited bandwidth of the reading incident beam (about 3 nm FWHM) is the main source of this error. Considering this bandwidth, the theoretical result will be increased about 8%, reducing the total difference between the theory and experiment to less than 5%. We used a lens to form the point source of the spherical recording beam. The size of the resulting beam at focus is finite (non-zero). This is an important reason for the difference between theoretical and experimental results in Figure 6.7(a).

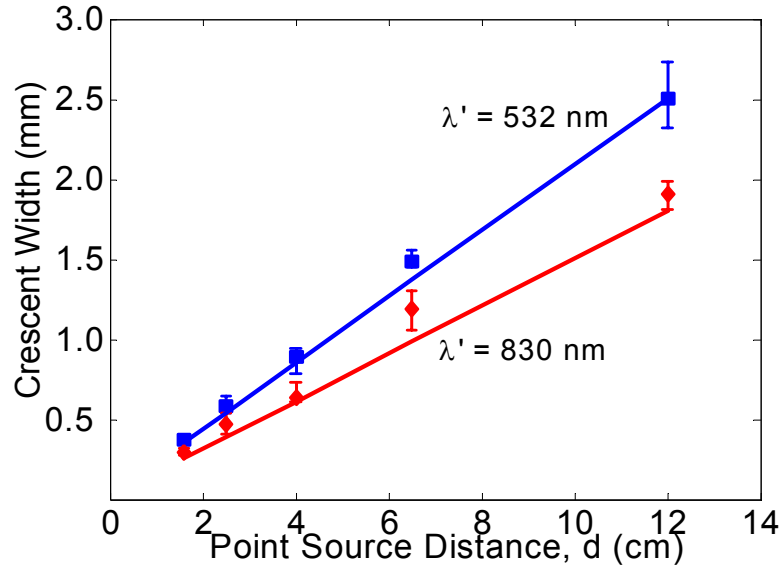

(a)

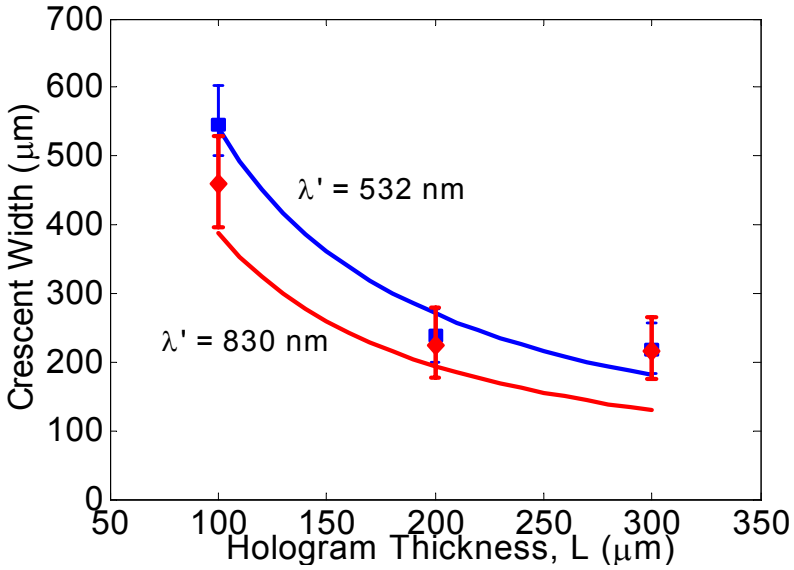

(b)

Figure 6.7. (a) The variation of the crescent width with the distance between the point source and the recording material during recording (*i.e.*, *d* in Figure 6.1(a)). Five different holograms are recorded at λ = 532 nm each with a different value of *d*. All other recording parameters are the same as those described in the caption of Figure 6.5(a). The hologram is read at both λ′ = 532 nm and λ′ = 830 nm. (b) Experimental and theoretical variation of the crescent width with hologram thickness for 100, 200 and 300 μm thick samples. The recording point source is at a distance of *d* = 1.6 cm from the hologram for all the cases. All other recording parameters are the same as those described in the caption of Figure 6.5(a). In both plots squares and diamonds with the error bars show the experimental results for reading at 532 nm and 830 nm wavelengths, respectively. The solid lines show the corresponding theoretical results based on the model described in this paper. In both figures, the error-bars represent the range of crescent widths measured at different heights of each crescent (*i.e.*, different value of *y* in Figure 6.4) close to the crescent center (*y* = 0).

As it is clear in Figure 6.7(a), the dark crescent becomes wider as d increases. To understand this variation, we can use a ray-optics approach [73] to relate the coordinates of each point in the hologram to the incident k-vectors in the recording spherical beam that originate from the point source. By increasing d, the difference between the k-vectors of two fixed points in the hologram plane becomes smaller. On the other hand, Bragg condition of the hologram allows for a fixed range of Δk of the original grating vectors to Bragg-match an incident collimated beam. Thus, by increasing d, the Bragg-matching region in the k-domain (*i.e.* Δk) corresponds to a larger range in the space-domain, resulting in a wider crescent. In the extreme case as $d \to \infty$, the spherical beam becomes a plane wave and the Bragg-matched diffracted beam becomes a plane-wave as well, resulting in an infinitely wide dark crescent in the transmitted beam for 100% diffraction efficiency.

Figure 6.7(b) shows the variation of the crescent width with hologram thickness. Again, the experimental results for reading at $\lambda' = 532$ nm and $\lambda' = 830$ nm are shown with squares and diamonds, respectively, for three different thicknesses. The corresponding error-bars as well as the theoretical variations of the width of the crescent as a function of the hologram thickness for reading at 532 nm and 830 nm wavelengths are also shown in this figure. As in Figure 6.7(a), the error-bars represent the range of crescent widths measured at different heights of each crescent close to the crescent center ($y = 0$). The finite bandwidth (about 3 nm) of the reading beam is taken into account for these calculations. The agreement between theory and experiment is good and in average, the theoretical results are within 10% of the experimental ones. More accurate results can be obtained using numerical inverse Fourier transformation as described before. Again,

the finite size of the experimental point source mainly contributes to the difference between theoretical and experimental results. Figure 6.7(b) shows that thicker holograms result in narrower crescents (*i.e.*, better spectral diversity) with all other parameters fixed. This is explained by noting that thicker holograms have better wavelength and angular selectivity. Thus, the range of grating vectors (*i.e.* Δk) that diffract the incident collimated beam becomes smaller as the hologram becomes thicker resulting in a smaller diffracted crescent.

The theoretical and experimental shape of the dark crescent read at $\lambda' = 532$ nm and $\lambda' = 830$ nm are depicted in Figures 6.8(a) and 6.8(b), respectively. The reading beam incident angle is about 13º for $\lambda' = 532$ nm. The hologram thickness is 300 μm. All other parameters are the same as those described in the caption of Figure 6.5. The agreement between theory and experiment in both cases is good. Note that we assumed a spherical beam originated from a true point source in our theoretical analysis, which is different from the actual experimental condition. Again, the finite size of the point source in the experiments is the main reason of the difference between theoretical and experimental results.

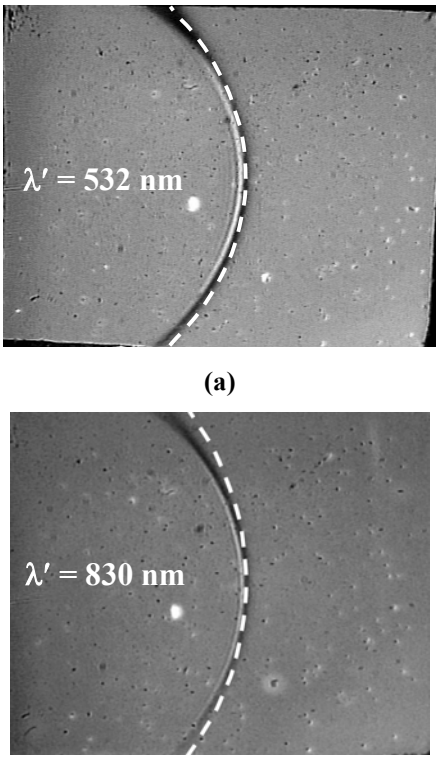

Figure 6.8. Theoretical (dashed white line) and experimental (dark crescent) shape of the dark crescent in the transmitted beam when the SBVH is read at (a) λ′ = 532 nm and (b) λ′ = 830 nm. All the parameters are the same as those described in the caption of Figure 6.5(a).

6.5 Discussion

The mapping of different wavelengths to different crescents by SBVHs (as shown in Figures 6.4) is useful for designing compact spectrometers. For these SBVHs, the output signal can be detected at the back face of the hologram, which allows for compact designs. A main limitation of such holographic spectrometers for using with incoherent light is caused by the ambiguity between the wavelength and the angle of the incident beam in Bragg condition [8]. For example, the size of the crescent in Figure 6.5(b) becomes larger when the divergence angle of the incident beam increases since the crescents corresponding to different reading plane waves of the same wavelength but different angles of incident occur at different (but close to each other) locations. The

same behavior is observed if we keep the incident angle constant but increase the wavelength range of the reading beam. It was shown in Ref. [74] that the acceptable divergence angle for a SBVH spectrometer that can still resolve a dark crescent is 45º in transmission geometry and 14º in reflection geometry. One interesting feature of the SBVH is the Fresnel transform relation between *k*-domain and space domain in these holograms. In conventional plane wave holograms used in spectroscopy, this relation (*k*-domain to space domain) is governed by a Fourier transformation. Thus, decreasing the size of the diffracted beam in one domain results in increasing the size of that in the other domain. In Fresnel transform, on the other hand, the quadratic phase factor caused by spherical recording beam allows for similar variations of size in the two domains. The limitation on this relation is imposed by the distance of the point source to the hologram (*d*) and the plane that the dark crescent is observed [*L* in Figure 6.1(a)].

We believe that optimal holographic spectral diversity filters (SDF) must be designed by using a more complicated spatial profile for the recording beam (compared to a spherical beam). Such a hologram can be recorded by interfering a plane wave and a modulated beam obtained by passing another plane wave through a spatial light modulator (SLM). Having a reliable and efficient simulation tool is essential for the optimization of such holograms. We believe the method we presented in this paper can efficiently be used for such optimization. In analyzing a hologram recorded by a plane wave and a beam from a SLM, we treat each pixel of the SLM as a point source and combine the output crescents corresponding to all these point sources. Since the analysis of the point source (*i.e.* pixel) can be done using analytic formulation, we can combine

this technique with sophisticated optimization schemes like stimulated annealing [75] to find the optimal SLM pattern.

6.6 Conclusion

We presented here a simple and efficient technique for the analysis of diffraction from spherical beam volume holograms (SBVHs). We showed that the output of a SBVH read by a collimated monochromatic plane wave could be found using a Fresnel transform. In special circumstances (which happen in most practical applications) the Fresnel transform can be simplified to an identity transformation by proper change of variables.

The method presented here can be extended to analyze more complicated holograms when read by plane waves. Although we used the proposed method to analyze holographic spectral diversity filters (SDFs), the method is quite general and can be used for any other application of SBVHs and even more complicated volume holograms. This method will be useful in optimizing volume holograms for several applications including spectroscopy.

We used the method for the analysis of SBVH spectral diversity filters and showed that the method can predict the experimental results with good accuracy. In particular, we showed that the diffraction of such a SBVH read by a monochromatic plane wave is a circular pattern for a large-size hologram and a crescent-shape pattern for smaller (practical) holograms. The dependence of the position of this crescent on reading wavelength both in the diffracted beam and in the transmitted beam allows for using these holograms for spectroscopy.

Chapter 7

Analysis of Slitless Holographic Spectrometers Implemented by Spherical Beam Volume Holograms

7.1 Introduction

In this chapter, we present a practical technique for implementing slitless spectrometers that is based on spherical beam volume holograms (SBVHs). We show that a compact and low-cost spectrometer can be designed by using a SBVH, thus making it a good candidate as a portable device for environmental and biological applications. In the previous section, we proposed the idea of using a SBVH as a diffractive element for spectroscopy. We showed when the SBVH is read with a collimated beam, a dark crescent forms in the back face of the hologram. The position of the dark crescent is a function of the reading wavelength. Using this method, the spectral contents of a collimated reading beam can be measured based on the location and the intensity of the dark crescents. Besides using the dark crescent, we also mentioned that the diffracted crescent could be used for spectroscopic applications. The diffracted crescents corresponding to different incident wavelengths propagate in different directions and focus in different locations. The main limitation imposed on the performance of a simple SBVH spectrometer based on these two approaches is the ambiguity between the reading incident angle and wavelength. Any change in the incident angle of the reading beam at a fixed wavelength also changes the location of the dark crescent and the location where

the diffracted beam is focused. Therefore, neither the dark crescent nor the diffracted crescent can be used directly to resolve the spectrum when the hologram is read with a non-collimated or a spatially incoherent beam. Although using a SBVH recorded in reflection geometry can reduce this ambiguity, it cannot eliminate it completely [74].

The analysis of the SBVH, presented in Chapter 6, suggests that although the dark crescents corresponding to different direction of the input are formed at different locations on the back face of the hologram. As we will show in this chapter, different diffracted crescents from different locations on the hologram propagate in the same direction for a monochromatic input beam. The direction of the propagation of these diffracted crescents changes with the wavelength. Therefore, using a Fourier-transforming lens after the SBVH, we can separate the diffracted crescents corresponding to different input wavelength at the focal plane of the lens. In this implementation, the effect of the incident angle of the reading beam on the locations of the output crescent is minimal. Different wavelength components are separated in different locations at the Fourier plane of the lens even when the input beam is spatially incoherent. As a result, there is no need to use a slit in the input plane of the spectrometer. This is the reason we refer to this spectrometer as a slitless volume holographic spectrometer.

In this chapter we focus on the exact analysis of these slitless spectrometers. We also provide the analysis of the conventional spectrometers and use the results to compare the slitless spectrometers with the conventional spectrometers. This analysis is important for understanding the main features and limitations of the slitless spectrometers. Furthermore, it is also useful for designing and optimizing these spectrometers both for general spectroscopy and for specific applications. In Section 7.2, we derive the transfer

function of the slitless volume holographic spectrometer. For later comparison, the transfer function of a conventional (slit-based) spectrometer, having a simple plane wave hologram as a diffractive element, is derived in Section 7.3. The theoretical evaluations are compared with the experimental results in Section 7.4 for both cases. In Section 7.5, we compare the performance of the proposed slitless spectrometer with the slit-based holographic spectrometer. Final conclusions are made in Section 7.6.

7.2 Transfer function of the slitless spectrometer

The slitless volume holographic spectrometer is based on a SBVH as a diffractive element. The SBVH is recorded in a holographic medium with thickness L using a point source and a plane wave as shown in Figure 7.1(a). The hologram thickness (L), the incident angle of the plane wave (θ_r), the location of the point source ($-a$, 0, $-d$), and the wavelength of the recording beams (λ) are the design parameters for the recording. The hologram is recorded in the transmission geometry as shown in Figure 7.1(a). This recording arrangement is the same as the one used in Section 6.2.

The hologram is then used in the spectrometer arrangement shown in Figure 7.1(b). The reading beam illuminates the hologram primarily in the direction of the recording spherical beam. Therefore, the diffracted beam, for the desired range of wavelength, diffracts mainly in the direction of the recording plane wave as indicated in Figure 7.1(b). The Fourier transforming lens is placed in the main direction of the diffracted beam and the output is captured in the focal (or Fourier) plane of the lens using a CCD camera. The focal length of the lens (f) is another design parameter of the spectrometer. The SBVH in this arrangement can be directly read with non-collimated beam and there is no need to

use a slit in the input of the spectrometer as we show in the following. Therefore, the SBVH is positioned at the very beginning of the system.

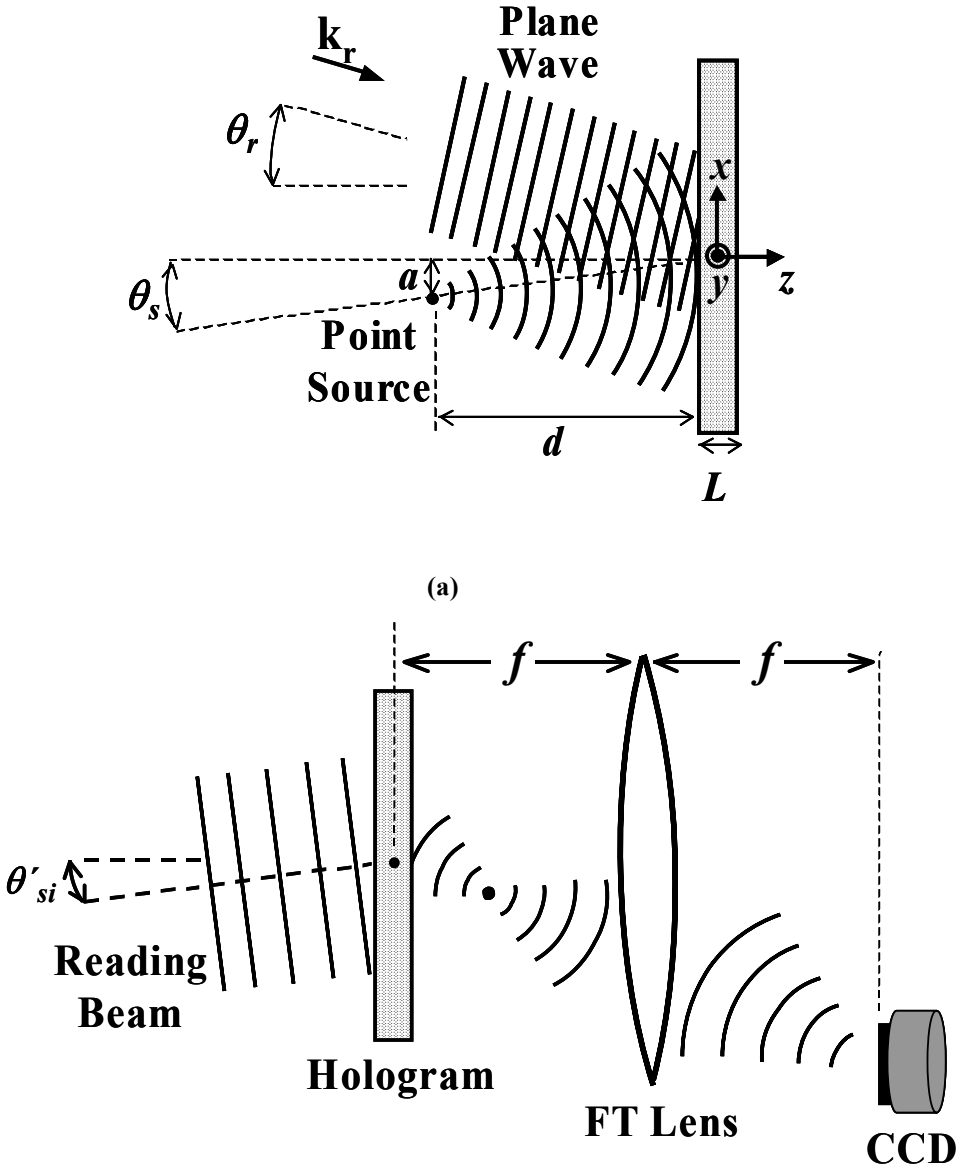

Figure 7.1. (a) Recording geometry of a spherical beam volume hologram. The point source is located at (-*a*, 0, -*d*). The reference beam (plane wave) incident angle is θ_r. A line from the coordinate origin to the point source makes an angle θ_s with the *z*-axis. The thickness of the holographic material is *L*. (b) Slitless spectrometer configuration. The reading beam is the input to the spectrometer having the incident angle of θ'_{si}. The focal length of the lens is *f*. The CCD is located at the back focal plane of the lens.

To analyze the slitless spectrometer, we first find the optical transfer function of the system shown in Figure 7.1(b). The transfer function is defined as the output of the system [at the CCD plane in Figure 7.1(b)] to an arbitrary input plane wave (with arbitrary propagation direction) at an arbitrary wavelength λ' [73]. In general, any input beam at wavelength λ' can be represented as a summation of several plane waves at that wavelength. Therefore, using the transfer function, the output of the system to an arbitrary beam can be found at any wavelength. As a result, the output corresponding to any input beam can be found by the analysis of different wavelength components of the beam.

In Chapter 6, we presented the complete analysis of a SBVH when read by a collimated beam from the direction of the point source at an arbitrary wavelength. In that analysis, the spherical beam was decomposed into several plane wave components. Each plane wave was assumed to form a hologram with the reference beam. To estimate the diffracted beam, the superposition of the diffracted plane waves was found from the corresponding holograms when read by a collimated beam at wavelength λ'. All the diffraction components were calculated using Born approximation. We can use the same approach to study the properties of the slitless volume holographic spectrometer, under diffuse light illumination at wavelength λ'. To calculate the output, we first find the transfer function (*i.e.*, the output from a specific input plane wave at wavelength λ') and then add the output components corresponding to different plane wave components of the input beam incoherently. We assume that the reading beam consists of several plane waves propagating in different directions and with independent random phases with uniform probability distribution. Throughout the analysis, we also assume both recording

and reading beams have TE polarization [*i.e.* electric field normal to the incident *x*-*z* plane in Figure 7.1(a)]. Calculation for the TM polarization (*i.e.* magnetic field normal to the incident *x*-*z* plane) can be found in a similar way.

To find the transfer function, assume that the electric field of a reading plane wave propagating in the direction $\mathbf{k'_i} = k'_{ix}\,\hat{\mathbf{a}}_\mathbf{x} + k'_{iy}\,\hat{\mathbf{a}}_\mathbf{y} + k'_{iz}\,\hat{\mathbf{a}}_\mathbf{z}$ with amplitude A_i and the phase φ_i, is represented by

$$E_i(k'_{ix}, k'_{iy}, k'_{iz}) = A_i\, e^{j\left(k'_{ix}x + k'_{iy}y + k'_{iz}z\right) + \varphi_i}\,. \tag{7.1}$$

From the analysis of Chapter 6, the electric field of the diffracted beam (E_{id}) from a SBVH can be written as

$$E_{id}(x,y,z) = \frac{e^{j(k_{rx}+k'_{ix})x} e^{jk'_{iy}y}}{4\pi^2} \iint \widetilde{E}_{id}(k_x, k_y, z) e^{-j(k_x x + k_y y)} dk_x dk_y\,, \tag{7.2}$$

where k_{rx} represent the *x*-component of the recording plane wave in Figure 7.1(a) and the diffracted field in the spatial-spectral domain [i.e., $\widetilde{E}_{id}(k_x, k_y, z)$] is represented by

$$\widetilde{E}_{id}(k_x, k_y, z) = \frac{j2\pi^2 \Delta\varepsilon\, k'^2 L\, A_i e^{j\varphi_i}}{\varepsilon\, k'_{idz}} \exp(jk'_{idz} z)\,\mathrm{sinc}\left[\frac{L}{2\pi}\left(K_{gz} + k'_{iz} - k'_{idz}\right)\right]. \tag{7.3}$$

In Equation (7.3), ε is the permittivity of the holographic recording material, $\Delta\varepsilon$ is the amplitude of the modulated permittivity, k' is the wave number at wavelength λ', and K_{gz} and k_{idz} are given by

$$K_{gz} = k_{rz} - \sqrt{k^2 - k_x^2 - k_y^2} \tag{7.4}$$

$$k'_{idz} = \sqrt{k'^2 - (K_{gx} + k'_{ix})^2 - (K_{gy} + k'_{iy})^2} \ . \tag{7.5}$$

with k being the wave number at wavelength λ, $K_{gx} = K_{rx} - k_x$, $K_{gy} = -k_y$, and $\mathbf{k_r} = k_{rx}\,\hat{\mathbf{a}}_\mathbf{x} + k_{rz}\,\hat{\mathbf{a}}_\mathbf{z}$ being the propagation vector of the recording plane wave.

Now we assume that the Fourier transforming lens is located at a distance f from the hologram as shown in Figure 7.1(b). Although this is not a necessary assumption for the operation of the spectrometer (*i.e.*, the Fourier transform can be obtained by other arrangements of the lens), it simplifies the calculations by eliminating the quadratic phase term resulted from the Fourier transform operation of the lens [73]. In this configuration, the CCD is located exactly at the back focal plane (or Fourier plane) of the lens. Assuming the lens is very large compare to the size of the hologram and using the paraxial approximation, the electric field of the output beam in the Fourier plane of the lens can be written as [73]

$$E_{io}(u, v, z = 2f) = \frac{A_i}{j\lambda' f}\mathcal{F}\{E_{id}(x, y, L/2)\}\Big|_{f_x = \frac{u}{\lambda' f} \text{ and } f_y = \frac{v}{\lambda' f}} \ , \tag{7.6}$$

where u and v are the output coordinates in the focal plane, f_x and f_y are the frequency variables of the two-dimensional Fourier transform operator $\mathcal{F}\{\cdot\}$ defined as [73]

$$\widetilde{P}(2\pi f_x, 2\pi f_y, z) = \mathcal{F}\{p(x, y, z)\} = \iint p(x, y, z) e^{-j\cdot 2\pi (f_x x + f_y y)}\, dx\, dy \ . \tag{7.7}$$

From Equation (7.2) it is clear that the diffracted beam (E_{id}) can be also represented as a Fourier transform. Therefore, Equation (7.6) can be written as

$$E_{io}(u,v,2f)=\frac{A_i}{j\lambda' f}\mathcal{F}\left\{e^{j(k_{rx}+k'_{ix})x}e^{jk'_{iy}y}\mathcal{F}^{-1}\left\{\widetilde{E}_{di}(k_x,k_y,2f)\right\}_{\substack{x\to -x\\ y\to -y}}\right\}_{f_x=\frac{u}{\lambda' f}\text{ and }f_y=\frac{v}{\lambda' f}}$$

$$=\frac{A_i}{j\lambda' f}\widetilde{E}_{id}\left(-(2\pi f_x-k_{rx}-k'_{ix}),-(2\pi f_y-k'_{iy}),2f\right)\Big|_{f_x=\frac{u}{\lambda' f}\text{ and }f_y=\frac{v}{\lambda' f}}$$

$$=\frac{A_i}{j\lambda' f}\widetilde{E}_{id}\left(-k'u/f+k_{rx}+k'_{ix},-k'v/f+k'_{iy},2f\right). \qquad (7.8)$$

Substituting $\widetilde{E}_{id}(k_x,k_y,z)$ from Equation (7.3) and replacing k_x and k_y by the its corresponding arguments according to Equation (7.8), the transfer function (the output electric field) can be written as

$$H(u,v,z=2f,\lambda')=E_{io}(u,v,2f)/(A_i e^{j\varphi_i})=$$
$$\frac{j2\pi^2\Delta\varepsilon k'^2 L}{\varepsilon_0\sqrt{k'^2-(k'u/f)^2-(k'v/f)^2}}\exp\left(j2f\sqrt{k'^2-(k'u/f)^2-(k'v/f)^2}\right)\times \qquad (7.9)$$
$$\operatorname{sinc}\left[\frac{L}{2\pi}\left(k_{rz}-\sqrt{k^2-(k'u/f-k_{rx}-k'_{ix})^2-(k'v/f-k'_{iy})^2}+k'_{iz}-\sqrt{k'^2-(k'u/f)^2-(k'v/f)^2}\right)\right]$$

As seen from Equation (7.9), the amplitude of the transfer function (the electric field in the output, E_{io}) is a function of output coordinate (u, v). Note that the maximum of H occurs at the output coordinates for which the argument of the *sinc* function in Equation (7.9) is zero. The locus of the maximum electric field is also a function of the reading beam direction represented by k'_{ix} and k'_{iy} in Equation (7.9). However, the effect of the direction of the reading beam on the location of the diffracted beam in the output is minimal for the practical range of angles, as we will examine below.

To find the output to an incoherent beam, we should add the output intensity of all of the input plane wave components (each one is a plane wave in Equation (7.1) with a random phase). Therefore, the total output intensity is

$$I_o(u,v,2f) = \int A_i^2(k'_{ix},k'_{iy})\left|H(u,v,z=2f,\lambda')\right|^2 dk'_x dk'_y = \int \left|E_{io}(u,v,2f)\right|^2 dk'_x dk'_y \ , \quad (7.10)$$

where the integration is over all the spatial frequency components (k'_{ix} and k'_{iy}) of the input reading beam.

Figure 7.2 shows the intensity distribution in the output for the region corresponding to the CCD area (6.9 mm × 4.6 mm) when a typical hologram is read with a spatially incoherent beam. In this calculation, the reading beam is modeled as a series of plane wave components with equal amplitudes and independent random phases for the incident angles in the range from $-\theta'_s$ to θ'_s with $2\theta'_s$ being the actual divergence angle of the input beam in the actual experiments in both *x*- and *y*-direction. The hologram is assumed to be recorded using the set up in Figure 7.1(a) with d = 4 cm, L = 300 μm, θ_r = 46º, and θ_s = -9º. The reading wavelength is λ' = 532 nm and is equal to the recording wavelength (λ). The refractive index of the recording material is assumed to be 1.5. The results in Figure 7.2 are calculated using θ'_s = 5º. As it is seen from Figure 7.2, the output is a single crescent, which is very similar to the output when a single collimated beam reads the hologram [for example see Figure 6.5(a)]. Therefore, the outputs of different plane wave components (or directions) of the reading beam at a single wavelength almost overlap at the same location in the output plane.

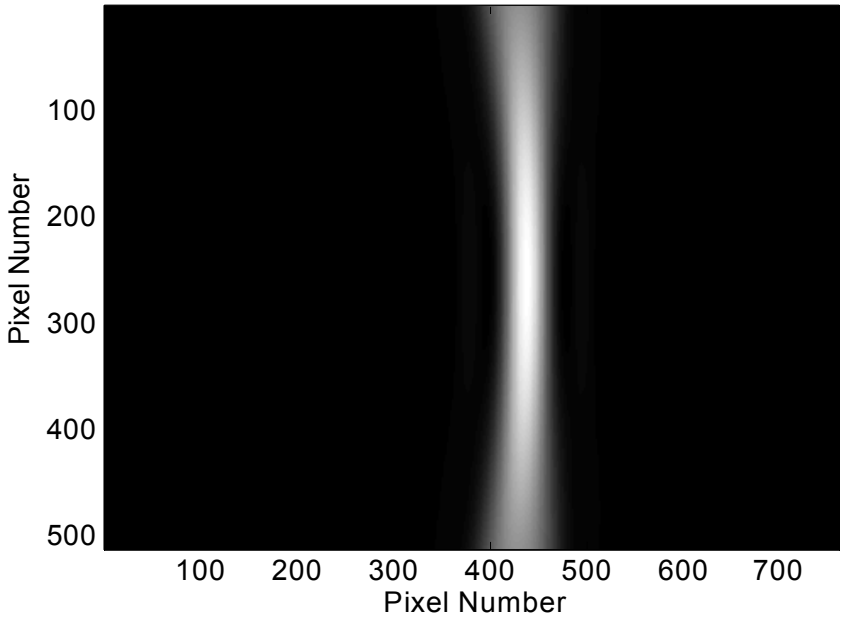

Figure 7.2. Theoretical intensity distribution in the output of the slitless holographic spectrometer estimated for the region corresponding to the CCD area when the hologram is read with a spatially incoherent reading beam. The incident angle of the reading beam is assumed to be from –5º to 5º measured in the air in both *x*- and *y*-direction. The hologram is assumed to be recorded using the set up in Figure 7.1(a) with d = 4 cm, L = 300 μm, θ_r = 46º and θ_s = -9º. The reading wavelength is 532 nm, which is equal to the recording wavelength. The refractive index of the recording material is assumed to be 1.5.

Note that for the experimental measurements, the Fourier transforming lens is mounted perpendicular to the direction of the diffracted beam as shown in Figure 7.3. Compared to the arrangement shown in Figure 7.1(b), the experimental configuration is rotated and also shifted in the space domain. The rotation of the lens is equivalent to the rotation (or a phase shift) of the incident beam in paraxial approximation. Therefore, the effect is equivalent to a shift in the Fourier domain or a shift in the position of the diffracted crescent in the Fourier plane of the lens. Also, the shifts in the lens coordinate, as it is seen in Figure 7.3 compared to Figure 7.1(b), results in a shift in the Fourier coordinates. Therefore, the difference in the theoretical configuration with the experimental setup is a shift in the Fourier plane and can be compensated with a constant

shift. The theoretical configuration reduces complicated conversions between rotated coordinates and is easier to analyze. On the other hand, the main benefit of mounting the lens in the direction of the diffracted beam in the experimental setup is to reduce the vignetting effect caused by the limited size of the lens. Also, the aberration introduced by the lens is minimal in this configuration [73].

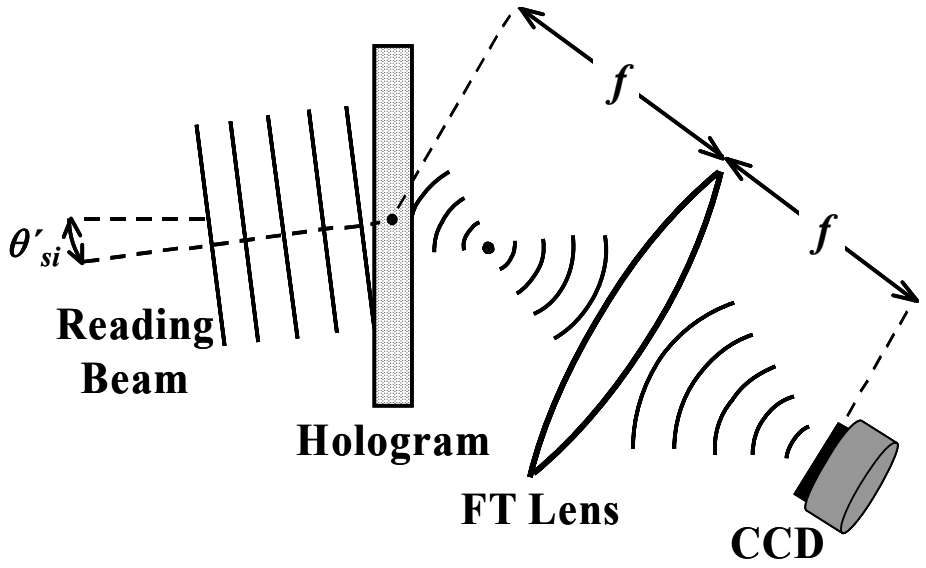

Figure 7.3. The experimental arrangement of the slitless spectrometer. All the parameters are the same as those in the caption of Figure 7.1(b).

7.3 Transfer function of a conventional spectrometer

To better understand the properties of the slitless volume holographic spectrometer, we compare it with a spectrometer based on a conventional implementation shown in Figure 7.4. This spectrometer consists of a 4-*f* like system that images the input to the output at each wavelength. The hologram crosses the Fourier plane of the first lens and contains its focal point as shown in Figure 7.4.

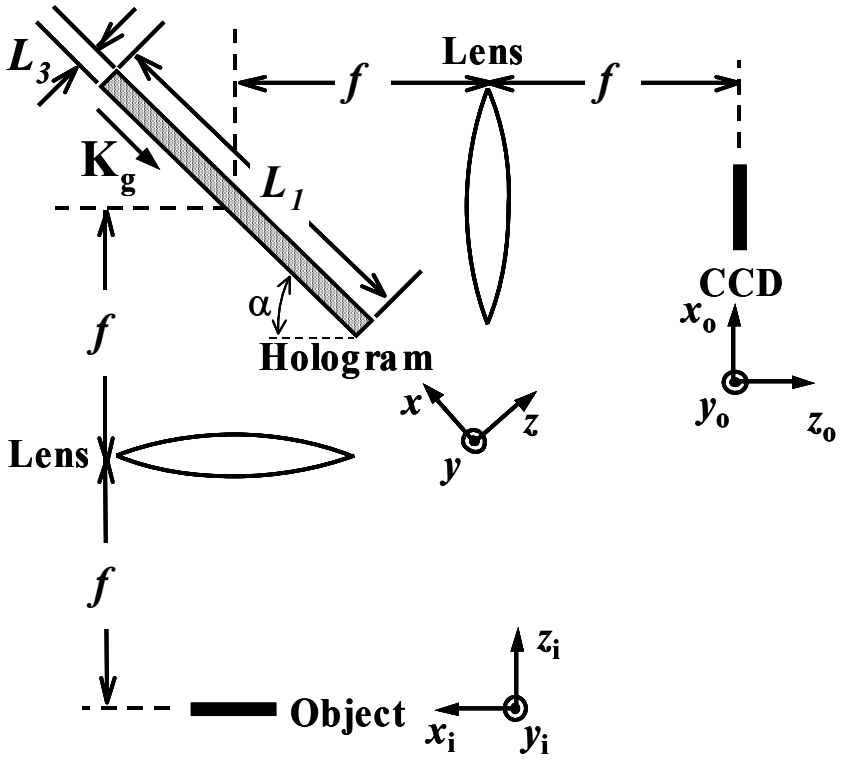

Figure 7.4. A basic arrangement of a spectrometer using a plane wave hologram as the diffractive element. The hologram dimensions are shown in the figure. The hologram height (the dimension in the *y*-direction) is assumed to be L_2 (not shown in the figure). The focal length of both lenses is *f*. The input object is usually a slit in the y_i-direction.

The angle between the hologram and the input plane (α) in the spectrometer setup is determined by the desired wavelength range of operation and the hologram recording parameters (*i.e.*, the direction and the period of the grating). The hologram is recorded with two interfering plane waves at wavelength λ using transmission geometry. The total angle between the recording beams in the air is 2θ and the beams have equal incident angles (measured between each beam and the normal to the hologram surface). Therefore, the grating vector ($\mathbf{K_g}$) is parallel to the hologram larger surface (parallel to *x*-axis in Figure 7.4) and its magnitude is $4\pi\cdot\sin(\theta)/\lambda$. Using Born approximation [71], the output corresponding to a monochromatic input point source at wavelength λ' located at (x_i, y_i) (i.e. the point spread function) can be written as

$$h(x_i, y_i; x_o, y_o; \lambda') = C\,\mathrm{sinc}\left(\frac{L_1}{2\pi}k_1\right)\mathrm{sinc}\left(\frac{L_2}{2\pi}k_2\right)\mathrm{sinc}\left(\frac{L_3}{2\pi}k_3\right), \tag{7.11}$$

$$k_1 = \frac{2\pi}{\lambda'}\left[\left(\frac{-x_i}{f}+1\right)\cos(\alpha)-\left(\frac{x_o}{f}-1\right)\sin(\alpha)\right]+K_g \tag{7.12}$$

$$k_2 = \frac{2\pi}{\lambda'}\left(\frac{y_i}{f}+\frac{y_o}{f}\right) \tag{7.13}$$

$$k_3 = n\frac{2\pi}{\lambda'}\left[-\left(\frac{-x_i}{f}+1\right)\sin(\alpha)-\left(\frac{x_o}{f}-1\right)\cos(\alpha)\right] \tag{7.14}$$

where (x_o, y_o) represent the output coordinates, f is the focal length of the lenses, n is the index of refraction of the holographic material, K_g is the magnitude of the grating vector, and L_1, L_2, and L_3 are the hologram dimensions in x, y, and z directions, respectively. The amplitude factor C is a function of the diffraction efficiency of the hologram and can be estimated from Born approximation when the amplitude modulation of the permittivity (or the modulated refractive index) of the hologram is given. Since the throughput of the spectrometer is an important design factor, the hologram should have high diffraction efficiency. The ideal case would be a hologram with 100% diffraction efficiency. Therefore, Born approximation is not accurate for estimating such diffraction efficiencies and more accurate models like Kogelnik method [9] or rigorous coupled wave analysis (RCWA) [10] must be used. The RCWA method considers all the reflected and transmitted orders for diffraction and yields to accurate numerical estimation in most of the cases [10]. In the Kogelnik method, which provides the closed-form solution, only the zeroth and first order diffraction for the transmitted beam is considered and might not

result in very accurate estimation when the reflection at the boundaries are significant. It should be noted that the results from the Kogelnik approach and the RCWA are exactly the same if we consider no reflection from faces of the hologram due to change in the refractive index from air to material and the hologram is a Bragg grating (only zeroth and first order diffraction).

In the both accurate approaches (RCWA and Kogelnik) the hologram is assumed to have infinite transverse dimensions. While Born approximation is a valid assumption for weak holograms, as it is illustrated in Equation (7.11), it provides a closed-from solution and can also be used for a hologram with finite lateral dimensions. When the hologram becomes strong the depletion of the reading beam should be taken into account for Born approximation. Comparing Born approximation with Kogelnik's method, we expect that the depletion of the reading beam results in the variation of the diffraction efficiency as a sin^2 of the constant C in Equation (7.11). It means that we can simply use the "*sin"* of the point spread function in Equation (7.11) and the results would be similar to those we can get from the Kogelnik method for all the practical purposes. We refer to this method as modified Born approximation and we calculate the diffraction efficiency (η_{MB}) as $\eta_{MB} = \sin^2\left(\sqrt{\eta_{Born}}\right)$, where η_{Born} is the diffraction efficiency calculated using Born approximation.

Figure 7.5(a) shows the diffraction efficiency of a typical strong hologram as a function of normalized modulated permittivity ($\Delta\varepsilon/\varepsilon$) when it is calculated using Born approximation, modified Born approximation, and Kogelnik method. The hologram is assumed to be recorded using two plane waves at 532 nm wavelength. Each plane wave has an incident angle of 35º in the air. The refractive index of the recording material is *n*

= 1.5. The hologram is read with one of the beams to match the Bragg condition. The hologram thickness is assumed to be 100 μm. The polarization of the recording beams is TE. As it is seen in Figure 7.5(a), the maximum diffraction efficiency calculated using modified Born approximation and Kogelnik method are exactly the same. Note that using Born approximation for large permittivity modulations results in diffraction efficiencies greater than 100% that is meaningless. From Figure 7.5(a) it is clear that Born approximation is valid for diffraction efficiencies less than 10%. We have found similar behavior for TM polarization (*i.e.* magnetic field perpendicular to the plane of incident). Figure 7.5(b) shows the diffraction efficiency for the same hologram and for the maximum permittivity modulation $\Delta\varepsilon = 0.0062\ \varepsilon$ when the incident angle of the reading beam is changed from 32º to 38º outside the crystal. The reading beam, at 532 nm wavelength, has the TE polarization. There is an excellent agreement between the modified Born approximation and Kogelnik method. Again, similar results were obtained for TM polarization. Therefore, the modified Born approximation can be used with good accuracy for the analysis of the strong grating while it provides analytic solution for holograms with finite lateral dimensions. Note that we have not yet developed a mathematical proof for the equivalence of the two techniques (Modified Born and Kogelnik), but all our observations suggest very good agreement between them.

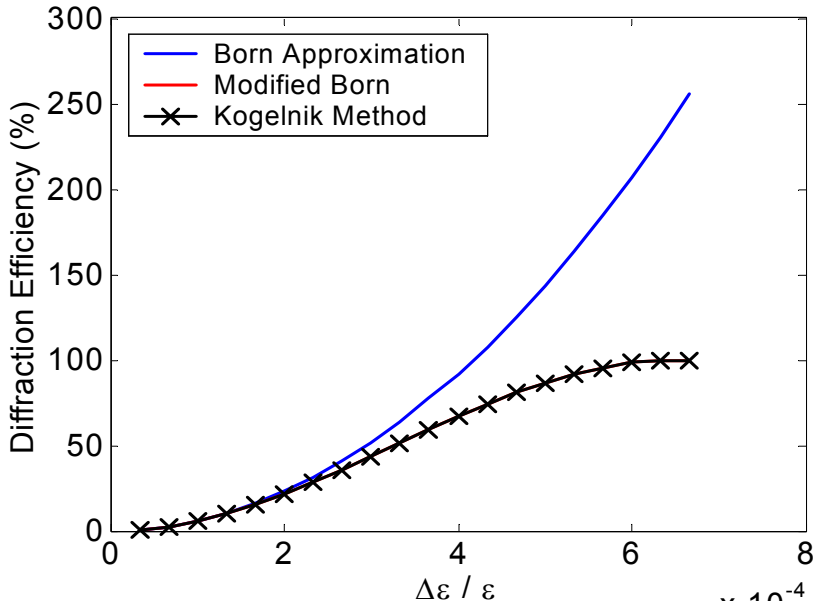

(a)

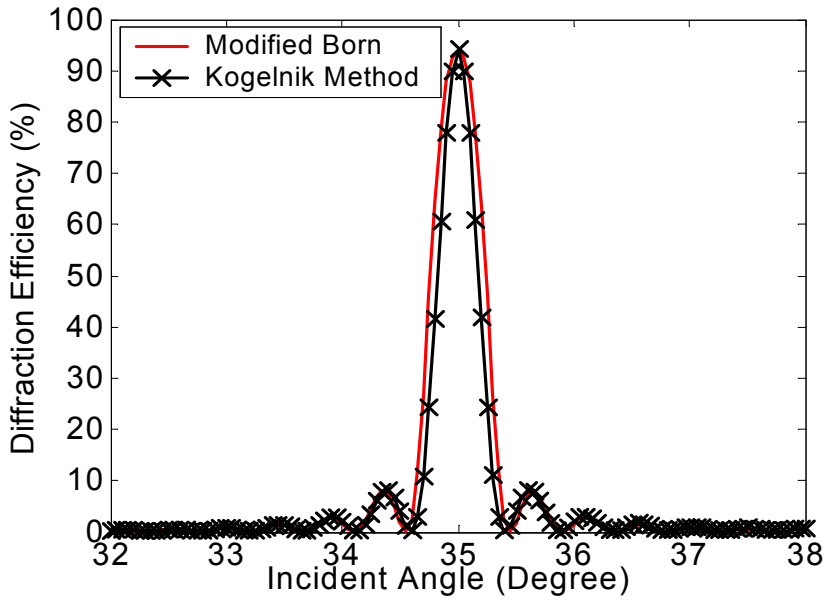

(b)

Figure 7.5. Diffraction efficiency of a plane wave hologram (a) as a function of normalized modulated permittivity (Δε/ε) for a Bragg-matched reading beam and (b) as a function of the incident angle of the reading beam for Δε/ε = 0.0062, calculated using Born approximation and Kogelnik method. The hologram is assumed to be recorded using two plane waves at 532 nm wavelength. Each recording plane wave has an incident angle of 35° in the air. The refractive index of the recording material is *n* = 1.5. The hologram thickness is assumed to be 100 μm. The polarization of the recording beams is TE. The diffraction efficiency in modified Born approximation (η_{MB}) is calculated as $\eta_{MB} = \sin^2\left(\sqrt{\eta_{Born}}\right)$, where η_{Born} is the diffraction efficiency calculated using Born approximation as described in the text.

For finding the complete output of the spectrometer, we assume the input is a spatial incoherent source with uniform intensity I_i over a slit in the input plane. We also assume that the slit size in the x- and y- directions are s_x and s_y, respectively. Therefore, the output corresponding to this input can be found form the convolution of $|h|^2$ [from Equation (7.11)] with the intensity distribution of $I_i \cdot \text{rect}(x/s_x) \cdot \text{rect}(y/s_y)$, where the rectangle function [rect(u)] is defined as

$$\text{rect}(u) = \begin{cases} 1 & |u| < \frac{1}{2} \\ 0 & \text{otherwise} \end{cases}. \tag{15}$$

When the diffraction efficiency of the hologram is high, we can use modified Born approximation by convolution of $\sin(|h|)^2$ with the intensity distribution of the input slit.

7.4 Experimental measurements of the spectrometers

In this section the theoretical results are compared with the experimental results for both the slitless volume holographic spectrometer and the conventional holographic spectrometer. For all the experiments, the holograms were recorded in Aprilis photopolymer [72] with a refractive index of 1.5. The recording wavelength was 532 nm. The polarization of the recording beams was TE and the holograms were recorded in transmission geometry.

For the SBVH, the hologram was recorded using the setup in Figure 7.1(a) with d = 4 cm, θ_r = 46º (in air), θ_s = 9º (in air), and L = 300 μm. For the conventional spectroscopy, we used a plane wave hologram recorded using two coherent plane waves at λ = 532 nm, each having an incident angle of θ = 35º in air with respect to the normal

to the surface of the recording material. The hologram dimensions were 1 cm, 1 cm, and 100 μm corresponding to L_1, L_2, and L_3 in Figure 7.4, respectively. The reason that a thinner hologram was used for this case was to obtain broader wavelength selectivity.

The reading configuration for the SBVH is shown in Figure 7.3. A beam from a monochromator with output aperture size of 1 mm reads the SBVH after passing through a rotating diffuser. The full-width half-maximum (FWHM) of the output of the monochromator was about 7.5 nm for the range of wavelength used in the experiment. The rotating diffuser is placed adjacent to the hologram (not shown in Figure 7.3) to generate a spatially incoherent reading beam that reads the hologram from almost every direction. The focal length (f) of the Fourier transform lens was 10 cm. The diffracted beam was monitored using a cooled CCD camera with 9 μm × 9 μm pixels mounted at the focal plane of the lens. The experimental result for the reading beam having three wavelength components at 492 nm, 532 nm and 562 nm is shown in Figure 7.6(a). The output corresponding to each wavelength was obtained separately and the results were added to obtain this figure. The theoretical results corresponding to the experimental ones are shown in Figure 7.6(b). The theoretical results were obtained from the analysis presented in Section 7.2 for the experimental parameters. Figure 7.6 shows good agreement between the theoretical and the experimental results. Note that the side lobes in the experimental results [Figure 7.6(b)] looks stronger that those in the theoretical results [Figure 7.6(a)], since the hologram is strong. The analysis of the strong SBVH is presented in Chapter 8.

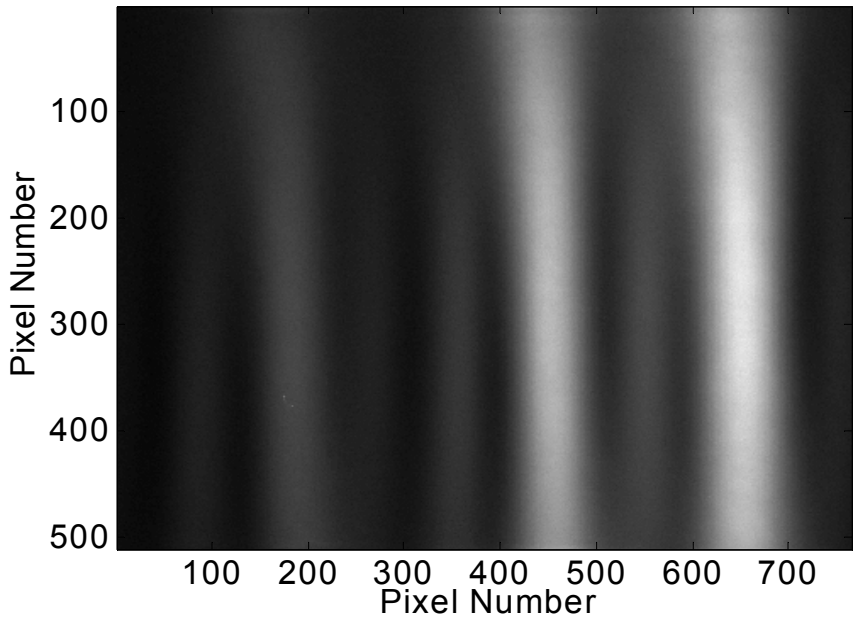

(a)

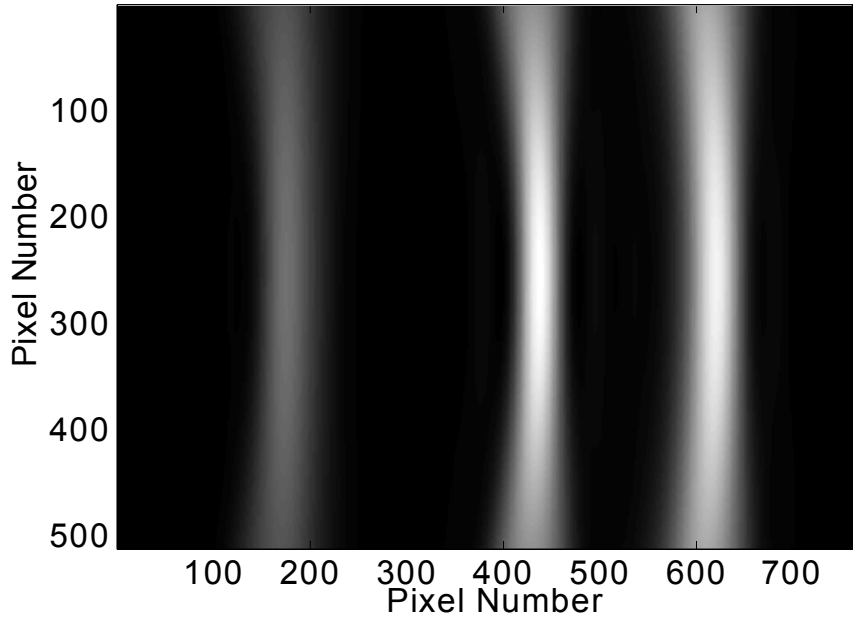

(b)

Figure 7.6. The output of the slitless spectrometer for an input beam having wavelength components at 492 nm, 532 nm and 562 nm obtained from (a) experiment and (b) theory. The SBVH was recorded using in Figure 7.1(a) with d = 4 cm, θ_r = 46° (in air), θ_s = 9° (in air), L = 300 μm, and f = 10 cm. The recording wavelength was 532 nm. The pixel size of the CCD camera was 9 μm × 9 μm. Note that the side lobes in the experimental results looks stronger that those in the theoretical results.

For the conventional plane wave holographic spectrometer (with slit present), the hologram was read by a beam obtained by passing white light through the monochromator described earlier with FWHM of 7.5 nm centered at 532 nm wavelength. The beam was collimated and passed through a square opening (or slit) of the size 140 μm × 140 μm. The focal length of the lenses was 6.5 cm. The output was monitored using a commercial CCD camera with pixel size of 9.8 μm × 9.8 μm. Note that the CCD in this case is different from that used in the previous experiment; however, this does not affect our results. The intensity distribution along the *x*-axis in the output plane is shown in Figure 7.7(a). The intensity distribution was also found theoretically by taking into account the FWHM of the reading beam and shown in Figure 7.7(a). The same results for the *y*-axis in the output plane are shown in Figure 7.7(b). The main reason for the difference in the output along *x*- and *y*-direction is the finite line-width of the monochromator. Since the grating vector is perpendicular to the *y*-axis (Figure 7.4), the broadening is only observed in the *x*-direction. This effect is observed in both theoretical and experimental results. In the *y*-direction the output is almost identical to the input in both theory and experiment. As it is seen from these figures, there is a good agreement between theoretical and experimental results for the conventional spectrometer.

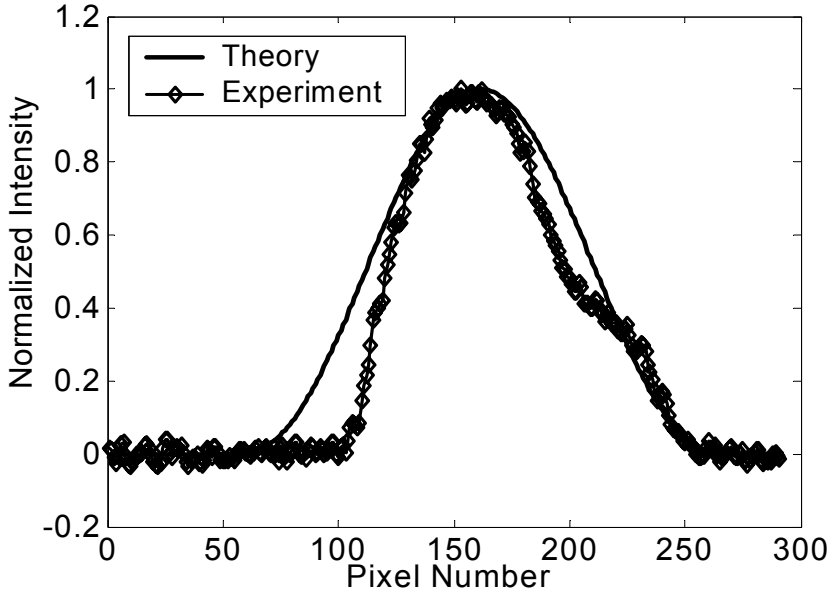

(a)

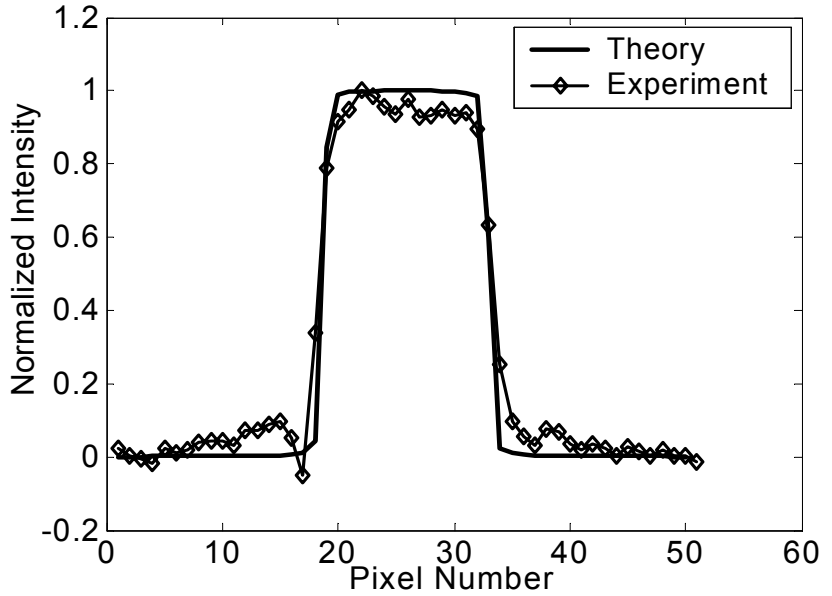

(b)

Figure 7.7. The distribution of the output intensity of the conventional spectrometer shown in Figure 7.4 obtained from both theory and experiment for (a) x_o-direction and (b) y_o-direction. The hologram dimensions were L_1 = 1 cm, L_2 = 1 cm, and L_3 = 100 μm. The focal length of both lenses was 6.5 cm. The hologram was recorded at 532 nm using two plane waves each having an incident angle of 35° measured in the air. The hologram was read by a beam at 532 nm obtained by passing white-light through a monochromator. The full-width half-maximum (FWHM) of the output spectrum of the monochromator at 532 nm wavelength was 7.5 nm. The beam was collimated and passed through a square opening of the size 140 μm × 140 μm (the object in Figure 7.4). The square shape was selected to show the difference in the output for different input directions. The output was monitored using a commercial CCD camera with pixel size of 9.8 μm × 9.8 μm. Note that only the range of CCD pixels corresponding to significant output signal is shown.

7.5 Comparison between slitless and conventional spectrometer

In this section, we use the theoretical model we derived so far to qualitatively compare the performance of spectrometers implemented based on two methods. We start by finding the output of the conventional spectrometer to a monochromatic and incoherent input beam. We then find the response of the slitless spectrometer to the same input and show the similarities between the two systems. We then discuss the effect of different components on the performance of each system.

We assume the input to the conventional spectrometer, shown in Figure 7.4, is an incoherent beam at wavelength λ', consisting of several plane wave components with random relative phases. A slit of the width s_w is placed in the object plane in Figure 7.4 that allows a small portion of each plane wave component to enter the spectrometer. For each monochromatic plane wave, the conventional spectrometer is equal to a 4*f* imaging system with the point-spread function given by Equation (7.11). Therefore, the output is a slit with the width s_w that is blurred with the point-spread function h. The effect of the change in the direction of the input plane wave does not change the location of the output since the 4*f* system images the input slit into the same output image at each wavelength. Therefore, the total output for the incoherent input is equal to the incoherent (or intensity) summation of the outputs of all plane wave components. Note that the performance of the 4*f* system is precise in to the paraxial regime and is limited to vignetting effect of the first Fourier transforming lens (the lens before the hologram) [73].

We derived the output of the slitless spectrometer to an incoherent input in Section 7.2. We showed that the output was a portion of a ring (or a crescent) as shown in Figure 7.2. We assumed that the monochromatic incoherent input beam is a summation of

several plane wave components with random phases. The output of each plane wave is a crescent in the output. The crescents for different plane wave components overlap in the output at a location that is a function of input wavelength. Therefore, the total output is the incoherent (or intensity) summation of the individual crescents at the output plane.

Comparing the operating principles of the two spectrometers we find several similarities. The output corresponding to a monochromatic input plane wave does not change with the incident angle of the plane wave. Therefore, the output to a monochromatic incoherent beam can be found by adding the output intensities of individual plane wave components. Also, we found that the spatial intensity pattern of the spectrometer output is a function of the input wavelength in both cases. In the conventional spectrometer the output is a narrow slit while in slitless spectrometer it is a narrow crescent for each monochromatic input beam. Since the output of the conventional spectrometer is almost the image of the input slit, we can substitute the rectangular input slit with a crescent shape slit (a transparency function similar to the beam shape in Figure 7.2) and the results of the conventional spectrometer would be the same as that of the slitless spectrometer. It suggests that the two systems operate similarly. By comparing the configuration of the slitless spectrometer (Figure 7.3) with the conventional spectrometer (Figure 7.4), we conclude that *the role of the spherical beam volume hologram is to implement three elements of the conventional spectrometer, i.e. the input slit, the input lens, and the diffractive element (plane wave hologram), into one element, i.e. the spherical beam volume hologram*. To be more specific, in the slitless spectrometer the input lens is implemented with a grating formed by a spherical beam

and a plane wave. Also, the role of the slit in conventional spectrometer is implemented by the Bragg selectivity of the volume hologram.

To further compare the two system, we must take into account some practical limitations such as the numerical aperture (NA) of the lenses. For example, the NA of the lens used to form the point source for recording the SBVH is the key parameter that specifies the range of the incident angle of the input beam of the spectrometer (reading beam), which by itself defines the throughput. Similarly, the NA of the first lens in the arrangement of the conventional implementation is the important parameter in finding the range of the incident angle of the input beam to the system. For example, if the input source is a fully incoherent source that emits light in all the directions, only a portion of the energy that is distributed over 4π steradian solid angle goes into the system. Therefore, a limitation exists on the acceptance input power due to limited NA of the practical lenses in both cases. Lenses with high NA are hard and costly to make. For conventional spectrometer the lens is a part of the actual system. However, in slitless spectrometer, the lens is used to record the hologram that is installed in the system. Therefore, the cost per device of the slitless spectrometer with a lens with high NA is much less than that of the conventional spectrometer with a similar input lens performance.

For the dispersive element that should be used in each system, both the diffraction efficiency and the wavelength selectivity of the holograms are important. In the conventional spectrometer, the grating should be thin (thickness in the range of a few microns) to diffract a large range of wavelength with high diffraction efficiency. On the other hand, the diffraction efficiency of the hologram reduces by decreasing the material

thickness [9-10, 71]. The main challenge in fabricating the holograms for conventional spectrometers is maximizing the diffraction efficiency for the thin material. In slitless spectrometer, in contrast to the conventional spectrometer, the range of the diffracted wavelength is limited by the divergence angle of the recording point source. The wider the angle, the larger the wavelength range of the operation is. Therefore, there is not direct relation (or trade-off) between the operating range of wavelength and the thickness of the material. However, the hologram thickness defines the crescent thickness and, therefore, the wavelength resolution. The thicker the hologram, the narrower the crescent is and the higher the resolution. The role of the thickness of the crystal in slitless spectrometer is similar to the width of the slit in the conventional spectrometer. As we mentioned before, increasing the material thickness results in a higher dynamic range for holographic recording. In the slitless spectrometer, increasing the material thickness improves the peak diffraction efficiency of the crescent. Therefore, the peak diffraction efficiency and the wavelength resolution can be improved simultaneously by using a thicker hologram. This makes the fabrication of the SBVH very easy for the slitless spectrometer. Furthermore, we can multiplex more SBVHs to obtain multiple (thin) crescents for each wavelength to avoid loosing the throughput of the spectrometer. The detection parts of both devices are almost the same and we do not consider the effects of the CCD in our analysis.

Implementing three different elements of the conventional spectrometer into one element in the proposed slitless spectrometer makes it more compact. Also, the Fourier transform lens can be placed very close to the hologram that further reduces the total size of the device. Since the slitless spectrometer uses fewer optical elements, it is less

sensitive to the alignment. It is also more robust to the changes in the alignment because of temperature change, vibration, and aging. Also, removing the input slit and lens reduces the total cost of the device. The SBVH is placed at the very beginning of the device and the coupling to the device is very easy. For the conventional spectrometer, usually an external lens is needed to provide efficient coupling of the light to the spectrometer. All these features make the proposed slitless spectrometer a very good candidate for low-cost portable spectrometers. Furthermore, replacing the input slit and lens with a volume hologram provides us with more design flexibility, especially for application-specific spectrometers, through optimization of the volume hologram that we record. Some possibilities are multiplexing several SBVHs to develop more complex spatial-spectral pattern in the spectrometer output (compared to a simple crescent) to implement multimode-multiplex spectroscopy. Such complex (and in the ideal case, optimal) volume holograms in the slitless architecture would implement complex slits in conventional architecture that are more expensive and more alignment sensitive. Note that by using a more complex volume hologram, it is even possible to remove Fourier-transform lens and develop an ultra-compact spectrometer, which is composed of only a volume hologram and a CCD camera (or a detector array). These are all the possible directions to improve the performance of the SBVH based spectrometer.

7.6 Conclusion

We presented in this chapter the complete analysis of the slitless spectrometer based on spherical beam volume hologram. The proposed spectrometer consists of a spherical beam volume hologram followed by a Fourier transform lens and a CCD. We derived the

transfer function of the slitless spectrometer and showed that the output is not sensitive to the incident angle of the input beam. We showed that the theoretical results agree well with the experimental data. Also, we found the transfer function of the conventional spectrometer that consists of an entrance slit, a collimating lens, a plane wave hologram, a collector lens, and a CCD. Again, the agreement between the theoretical and the experimental results was very good. Using the theoretical models, we showed that the slitless spectrometer is a compact implementation of the conventional spectrometer when the slit is implemented by the Bragg selectivity of the volume hologram, and the function of the collimating lens is included in the spherical beam volume hologram. Therefore, the proposed method enables making compact and low-cost spectrometer suitable for portable applications. Since the hologram is placed at the input of the spectrometer, light can easily couple into the device.

We also showed that the slitless architecture has more design flexibility, as the dependency of the performance on the design parameters is different from that of the conventional spectrometer. Particularly, we showed that the wavelength range of operation depends on the recording parameters of the SBVH (basically, the divergence angle of the recording spherical beam) in the slitless spectrometer in contrast to that dependency on the thickness of the holographic material in the conventional spectrometer. We also showed that the resolution of the slitless spectrometer is a function of the hologram thickness, and it is possible to design optimal spectrometer by simply recording an optimal volume hologram, which does not add the hardware complexity of the spectrometer.

Chapter 8

Generalization of Multi-Grating Method

8.1 Introduction

In chapter 6, we introduced the multi-grating method and used that for analysis of the spherical beam volume hologram (SBVH). We found the closed form solution of the diffraction from the SBVH when it is read by a plane wave at any wavelength. We showed that the experimental results are in good agreement with the results from the closed form solution. We further used the method in Chapter 7 to fully analyze the slitless spectrometer based on SBVHs. In all these cases, the SBVH was recorded using a spherical beam and a plane wave.

In this Chapter, we generalize the multi-grating method that can be used to analyze any arbitrary hologram recorded by complicated reference and signal beams. We use the idea of multi-grating method to represent the hologram as a superposition of several sinusoidal gratings. When the reading beam reads the hologram, the diffracted beam is obtained by the superposition of the diffracted components from all the gratings.

In the multi-grating method we assume that Born approximation is a valid assumption for analysis of each holographic grating. This is a valid assumption for many applications. However, for strong holograms (with large diffraction efficiency) a more accurate method is needed. In this chapter we also introduce a modified multi-grating method that can be used for the analysis of the strong hologram. We show that the

method is capable of explaining some experimental observations that are not clearly understood by the original multi-grating method.

After this introduction and in Section 8.2, the generalized multi-grating method is introduced for the analysis of an arbitrary hologram. The method is then used in Section 8.3 to analyze a hologram recorded using two point sources. The results from the analysis of the hologram recorded by two point sources are presented and compared with the experimental results in Section 8.4. In Section 8.5 the modified multi-gratin method based on coupled wave theory is explained that can be used to analyze strong holograms. The results of the analysis of a strong SBVH is also presented and explained. Final conclusions are made in Section 8.6.

8.2 Analysis of a hologram recorded by two arbitrary beams

In the multi-grating method of Chapter 6, the complicated signal beam was decomposed into its plane wave components. The gratings formed by the interference of these plane wave components with the reference plane wave were considered to find the diffraction from the hologram. For an arbitrary hologram, in addition to the signal beam, the reference beam is also a complicated beam. Using the idea of the multi-grating method, we can also decompose the reference beam to its plane wave components. The gratings formed by the interference of plane wave components of the signal and the reference beam can be used to obtain the diffraction from the hologram. Therefore, there is a potential for the multi-grating method to be extended for the analysis of a general hologram. It should be mentioned that this is a direct expansion of the method. However, as we develop the generalized multi-grating method, we explain how the idea can be

easily implemented by considering the expansion of the hologram itself (based on several grating components) rather than using all the gratings formed by plane wave components of the signal and reference beams.

To mathematically describe the method, we use the same approach as explained in Appendix C. The perturbation in permittivity in the interference region is

$$\Delta\varepsilon(\mathbf{r}') = \varepsilon_1 E_r(\mathbf{r}') E_s^*(\mathbf{r}') + \text{c.c.} \tag{8.1}$$

where E_r and E_s are the scalar electric fields of the reference and signal beams, respectively, $\mathbf{r}'$ is the position vector, ε_1 is a proportional constant, the elevated star (*) shows the complex conjugate operation, and c.c. means the complex conjugate of the preceding term. Suppose that we represent the signal beam (E_s) in a plane parallel to $x'y'$ plane using its Fourier components as

$$E_s(\mathbf{r}') = \iint_{k_{sx},k_{sy}} A_s(k_{sx},k_{sy},z') e^{j\left(k_{sx}x'+k_{sy}y'\right)} dk_{sx}dk_{sy} \ , \tag{8.2}$$

where the integration is over all values of k_{sx} and k_{sy}. The prime coordinates refers to the region inside the material, x'-direction is parallel to the x-direction in Figure (8.1) and the direction of y' is outward the plane of Figure (8.1). Similarly, the electric field of the reference beam can be written as

$$E_r(\mathbf{r}') = \iint_{k_{rx},k_{ry}} A_r(k_{rx},k_{ry},z') e^{j\left(k_{rx}x'+k_{ry}y'\right)} dk_{rx}dk_{ry} \ . \tag{8.3}$$

The perturbation in permittivity can be written as

$$\Delta\varepsilon(\mathbf{r}') = \varepsilon_1 \iint_{k_{rx},k_{ry}} \iint_{k_{sx},k_{sy}} \left[A_r(k_{rx},k_{ry},z') A_s^*(k_{sx},k_{sy},z') e^{j\left[(k_{rx}-k_{sx})x'+(k_{ry}-k_{sy})y'\right]} + \text{c.c.} \right] dk_{sx}dk_{sy}dk_{rx}dk_{ry} \quad . \quad (8.4)$$

The relation in Equation (8.4) can be efficiently rewritten using the convolution property of Fourier transform. However, we keep the current format since the argument of the integral represents a sinusoidal grating and the diffraction from such a grating can be calculated in the closed form using Born approximation. Using the Born approximation (Appendix C), the electric field of the diffracted beam $\mathbf{E}_d$ at position $\mathbf{r}$ from the hologram read by a beam with an electric field of $\mathbf{E}_p$ and a wavelength of λ' is

$$\mathbf{E}_d(\mathbf{r}) = \iint_{k_{rx}k_{ry}} \iint_{k_{sx}k_{sy}} \left\{ \int_V \frac{\varepsilon_1 e^{jk'|\mathbf{r}-\mathbf{r}'|}}{4\pi\varepsilon_0 \,|\, \mathbf{r}-\mathbf{r}' \,|} \nabla' \times \nabla' \times \left[\left(A_r A_s^* e^{-j\left[(k_{rx}-k_{sx})x'+(k_{ry}-k_{sy})y'\right]} + \text{c.c.} \right) \mathbf{E}_p(\mathbf{r}') \right] dv' \right\} dk_{sx}dk_{sy}dk_{rx}dk_{ry} \quad , (8.5)$$

where the inner integral is over the volume V, ε_0 is the average (unperturbed) permittivity of the medium, k' is the wave number at wavelength λ', and $\mathbf{r}' = (x', y', z')$ is a position vector in the volume V. Note that in Equation (8.5) we consider both terms of $\Delta\varepsilon$. Depending on the direction and the spatial frequency content of the reading beam, either one of the terms in $\Delta\varepsilon$ or both of them can result in Bragg matched diffracted components. Equation (8.5) represents the general form of calculating the diffracted beam from an arbitrary hologram using the Born approximation. The integral over the volume V in Equation (8.5) represents the diffraction from a sinusoidal grating when it is read by a plane wave. This integration can be obtained in a closed form and, therefore, the total diffracted beam can be calculated using two inverse Fourier transforms as stated

in Equation (8.5). For numerical calculation of Equation (8.5), we can use two-dimensional inverse Fourier transform techniques, such as IFFT in MATLAB, and no integration is needed.

In the general multi-grating method explained above, we find different grating components by finding the interference between different plane wave components of the reference and signal beams. However, a complicated hologram can also be represented directly in the Fourier domain by obtaining the Fourier transform of Δε. In this case, a three-dimensional Fourier transform of the Δε provides the complex amplitude of sinusoidal gratings as

$$\Delta\varepsilon(\mathrm{r}') = \iiint_{k_x,k_y,k_z} \Delta\mathrm{E}(k_x,k_y,k_z)\, e^{j\left(k_x x'+k_y y'+k_z z'\right)} dk_x dk_y dk_z \,, \tag{8.6}$$

where the perturbation in the permittivity is represented by ΔE in the Fourier domain. Then the diffracted electric field of the hologram is

$$\mathbf{E}_d(\mathbf{r}) = \iiint_{k_x k_y k_z} \left\{ \int_V \frac{e^{jk'|\mathbf{r}-\mathbf{r}'|}}{4\pi\varepsilon_0\,|\,\mathbf{r}-\mathbf{r}'\,|} \nabla'\times\nabla'\times\left[\Delta\varepsilon(k_x,k_y,k_z) e^{-j\left(k_x x'+k_y y'+k_z z'\right)} \mathbf{E}_p(\mathbf{r}')\right] dv' \right\} dk_x dk_y dk_z \,. \tag{8.7}$$

Again the inner integral over the volume V is the diffraction from a sinusoidal grating that is read with a plane wave and the closed form solution to this integral is straightforward. The three-dimensional Fourier transform can be obtained using IFFN function in MATLAB. Depending on the application, either of these two methods can be used. In our case of interest, the first method requires more computations since we consider the combination of all the plane wave components of the two recording beams.

Nevertheless, the first method is more useful for intuitive understanding of the properties of the complicated holograms, especially when it is considered in the *k*-domain. On the other hand, the second method is easier to implement and it is usually more efficient computationally. It can be also used to obtain closed form solutions for the analysis of particular holograms.

8.3 Analysis of a hologram recorded by two point sources

In this section we use the generalized multi-grating method to analyze the diffraction from a hologram recording using two point sources. We assume the hologram is recorded using a diverging spherical beam and a converging one as shown in Figure (8.1).

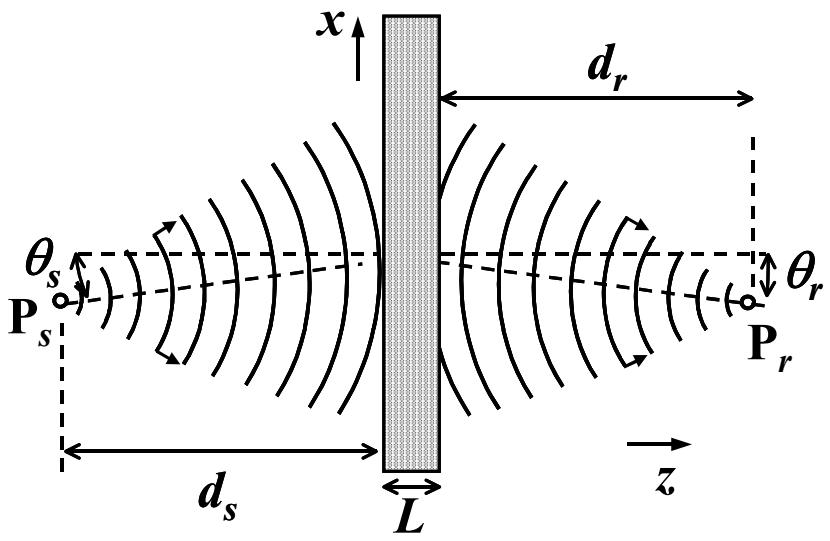

Figure 8.1. The recording configuration for the hologram recorded using two point sources. The signal beam is a diverging beam from a point source located at P_s. The reference beam is a spherical beam converges to the point P_r. The thickness of the holographic material is *L*.

The signal beam is a diverging spherical beam originated from a point source (P_s) at ($-d_s$, 0, $-d_s \tan(\theta_s)$) and the reference beam is a converging spherical beam from a point

source (P_r) at (d_r, 0, -d_r tan (θ_r)). The thickness of the recording material is L. The wavelength of the recording beam is λ.

The hologram is read mainly in the direction of the signal beam and the diffracted beam is monitored close to the reference point source (P_r). The wavelength of the reading beam is λ'. The reading beam is assumed to be a monochromatic incoherent beam. As before, the output from the plane wave components of the reading beam is obtained separately and then the outputs are added incoherently to find the diffracted beam.

Suppose that a plane wave component of the reading beam has complex amplitude of A_p and a wavevector of (k'_{px}, k'_{py}, k'_{pz}). To obtain the output corresponding to this reading plane wave we use Equation (8.4). The inner integral in Equation (8.4), *i.e.* the integral over the volume V, is the Born integral for the simple case of a plane wave reading a sinusoidal grating and the result is available in closed form solution [71]. The integral over the volume in Equation (8.5) results in plane wave components of the diffracted electric field that can be represented by

$$\widetilde{E}_d\left(k'_{dx}, k'_{dy}, z\right) = \frac{j\Delta\varepsilon k'^2 L}{2\varepsilon_0 k'_{dz}} e^{jk'_{dx}x} e^{jk'_{dy}y} e^{jk'_{dz}z} \operatorname{sinc}\left[\frac{L}{2\pi}\left(K_{gz} + k'_{pz} - k'_{dz}\right)\right], \qquad (8.7)$$

where the components of the wave vector of the diffracted beam are

$$k'_{dx} = k_{rx} - k_{sx} + k'_{px}, \qquad (8.8)$$

$$k'_{dy} = k_{ry} - k_{sy} + k'_{py}, \qquad (8.9)$$

$$k'_{dz} = \sqrt{k'^2 - k'^2_{dx} - k'^2_{dy}}, \qquad (8.10)$$

the z-component of the grating vector (K_{gz}) is

$$K_{gz} = \sqrt{k^2 - {k_{rx}}^2 - {k_{ry}}^2} - \sqrt{k^2 - {k_{sx}}^2 - {k_{sy}}^2}\,, \tag{8.11}$$

and the value of $\Delta\varepsilon$ is given by

$$\Delta\varepsilon = j\chi \frac{e^{-jk_{rx}d_r \sin(\theta_r)} e^{jk_{rz}d_r}}{\sqrt{k^2 - k_{rx}^2 - k_{ry}^2}} \frac{e^{jk_{sx}d_s \sin(\theta_s)} e^{jk_{sz}d_s}}{\sqrt{k^2 - k_{sx}^2 - k_{sy}^2}}, \tag{8.12}$$

where χ is a constant. Then, the diffracted beam can be found by adding all of its plane wave components diffracted from all the gratings. From Equation (8.8) and (8.9) we expect that for example for different sets of k_{rx} and k_{sx}, we obtain the same value for k'_{dx}. The same behavior can observe for the *y*-components. This means that the diffraction from different grating components would propagate in the same direction. This is similar to the convolution property in the Fourier domain and suggests representing Equation (8.5) with a simpler relation based on convolution. However, we cannot replace the consecutive inverse-Fourier transforms of Equation (8.5) with a single inverse Fourier transform using the convolution theorem because of the *sinc* term inside the integrals. The *x*- and *y*-components of the gratings diffract in the direction of k'_{dx} are the same, however, the *z*-components of the grating vectors are different as suggested by Equation (8.11) and, therefore, the value of the *sinc* function in Equation (8.5) would be different for different set of k_{rx} and k_{sx}.

8.4 Simulation and experimental results

In this section we present the simulation results as well as the experimental results for the diffraction from a hologram recorded in the configuration shown in Figure 8.1. In all the cases, the hologram is recorded in a 300 μm thick Aprilis photopolymer. The signal point source is at a distance d_s = 4 cm from the hologram and θ_s = 35º. The reference beam is at a distance d_r = 4 cm from the hologram and θ_r = 0º. The hologram is recorded at wavelength λ = 532 nm. The hologram is read using an incoherent beam at wavelength λ' that can be different from the recording wavelength λ. The incoherent beam is modeled by several plane waves with different incident angles. The intensities of the diffracted beams from the plane waves are added to obtain the intensity of the output.

Since the two point sources are in the *x*-*z* plane and the main directions of the two spherical beams make an angle of 35º with each other in this plane, the dispersion property of the hologram is mainly observed in the *x*-direction. Figure 8.2 shows the experimental measurement of the diffracted pattern in a plane parallel to the *x*-*y* plane and located at z = 4 cm. The reading wavelength is 532 nm. As shown in this figure, the output is similar to the typical outputs we obtained for slitless spectrometers in Chapter 7. If we change the wavelength of the reading beam, the output will shift in the *x*-direction. Therefore, the main dispersion property of the hologram is observed in the *x*-direction and the *y*-direction is the degeneracy direction for the diffraction from the hologram. Knowing this, we calculate Equation (8.5) in a two dimensional space (the *x*-*z* plane) only to reduce the time of the simulations.

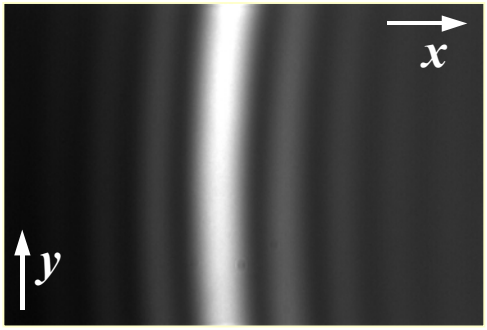

Figure 8.2. A typical output pattern from a hologram recorded in the arrangement of Figure 8.1 when read by a monochromatic beam. The recording parameters are $\lambda = 532$ nm, $d_r = 4$ cm, $\theta_r = 0^\circ$, $d_s = 4$ cm, $\theta_s = 35^\circ$, and $L = 300$ μm. The output is captured using a CCD located at $z = 4$ cm.

To obtain the diffracted beam, we use numerical calculation by sampling the wave vectors (k_{rx} and k_{sx}) and performing the simulations using MATLAB. The sampling period is always less than $\lambda/2$ to guarantee the sufficient sampling rate. When the diffracted plane wave components are obtained, the correct propagating phase factor is multiplied to each component corresponding to propagation in the z-direction. Then, the inverse Fourier-transform is obtained using IFFT function in MATLAB for the components propagated to a distance of z. Figure 8.3 shows the cross section of the diffracted beam in the x-direction for different propagation distances from $z = 3.6$ cm to $z = 4.7$ cm. The reading beam at wavelength $\lambda' = 532$ nm is modeled using 11 mutually incoherent plane waves. The incident angles of the plane waves are equally spaced over a range of 6.24º. The diffracted intensity is obtained by adding the intensities of the outputs corresponding to the diffraction by reading the hologram with these incoherent plane waves. As shown in Figure 8.3, the diffracted beam converges to its minimal width at distance $z = 4$ cm and then diverges. This distance is corresponding to the location of the converging spherical beam used during the recording. If a beam exactly the same as the signal beam was used, the output at $z = 4$ cm would be the same as the reference beam.

However, in the case of an incoherent reading beam, the output is no more similar to the reference beam used for the recording (see Figure 8.2). However, the output still has its minimal size in the *x*-direction at the location of the reference point source as suggested by Figure 8.3.

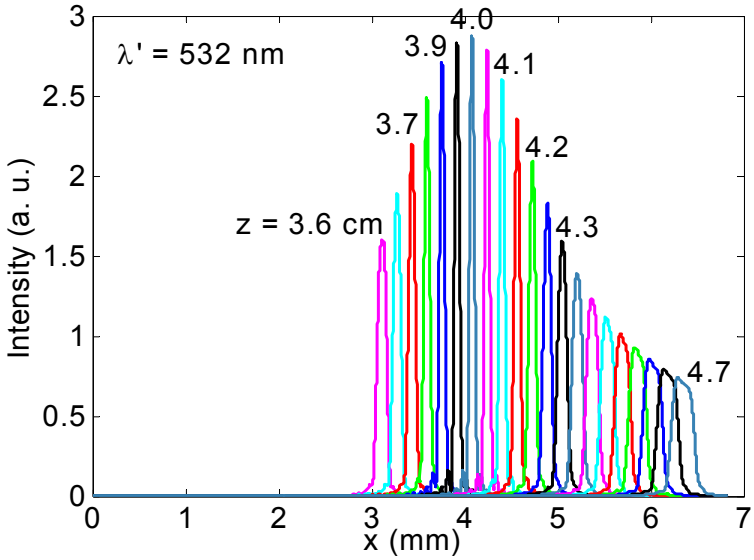

Figure 8.3. Intensity profile of the diffracted beam in the *x*-direction for different propagation distance *z*. The hologram is recorded in the geometry of Figure 8.1 with λ = 532 nm, d_r = 4 cm, θ_r = 0°, d_s = 4 cm, θ_s = 35°, and *L* = 300 μm. The reading beam at wavelength λ′ = 532 nm is modeled using 11 mutual incoherent plane waves as explained in the text.

In a case that an incoherent beam at another wavelength reads the hologram, the output will have its minimal width at a different location in both *x*- and *z*-directions. This is shown in Figure 8.4 where the outputs at their minimal width are shown when the hologram is read using an incoherent beam at wavelength λ′ = 532 nm and at wavelength λ′ = 502 nm. From the results shown in Figure 8.3 and Figure 8.4, it is clear that the output from a monochromatic and incoherent input source has a limited size around the location of the reference point source. Note that we have not used any filtering in the input and the incoherent beam directly reads the hologram. Another important result is

that the location of the output is wavelength dependent, *i.e.* if the wavelength of the input incoherent beam is changed the location of the output is changed. The change in the location of the output in the *x*-direction is the desire property of the hologram that can be used for spectroscopy (similar to the slitless spectrometer in Chapter 7). However, the change in the location of the output in the *z*-direction would affect the dispersive property of the hologram. Considering the output at the same distance *z* for both cases (for example at z = 4.3 cm in Figure 8.3 and Figure 8.4), we still observe the distinct separation of the output in the *x*-direction. However, the output beam at z = 4.3 cm and λ' = 532 nm is not at its minimal width. Therefore, the separation of the outputs at different wavelengths is not optimally obtained at a fixed distance *z*.

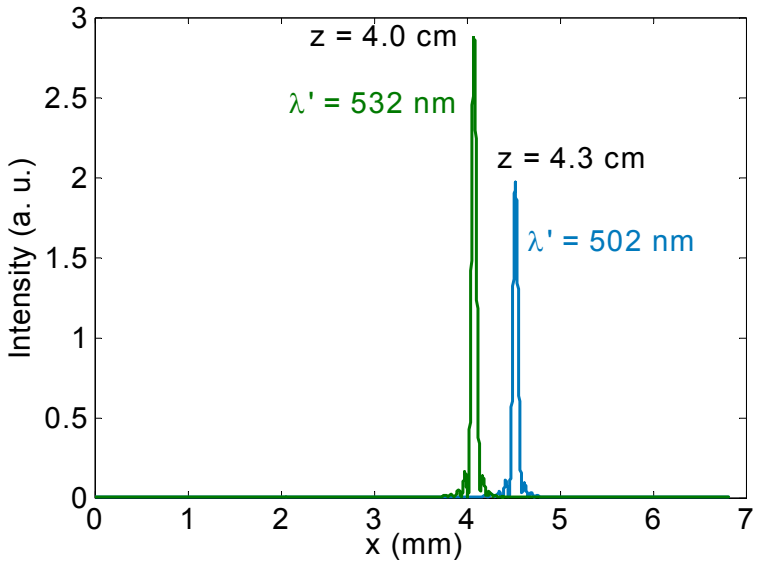

Figure 8.4. Intensity profile of the diffracted beam in the *x*-direction when the hologram is read with an incoherent beam at wavelength λ' = 532 nm and λ' = 502 nm. All the other parameters are the same as those explained in the caption of Figure 8.3.

Figure 8.5 shows the variation of the location of the minimal width of the output for different input wavelength. All the parameters are the same as those used for the results in Figure 8.3. As it is seen, there is a good agreement between the experimental and the

simulation results. However, the location of the minimal width of the output changes considerably (from 4 cm at $\lambda' = 532$ nm to more than 5 cm at $\lambda' = 442$ nm) for a wavelength range of 90 nm. This might be a limiting factor for the application of such a hologram as a dispersive element in a spectrometer. The analytical tool we developed here can be used to optimally design the recording parameters and reduce the variation of the location of the minimal width of the output over the spectrum range of operation.

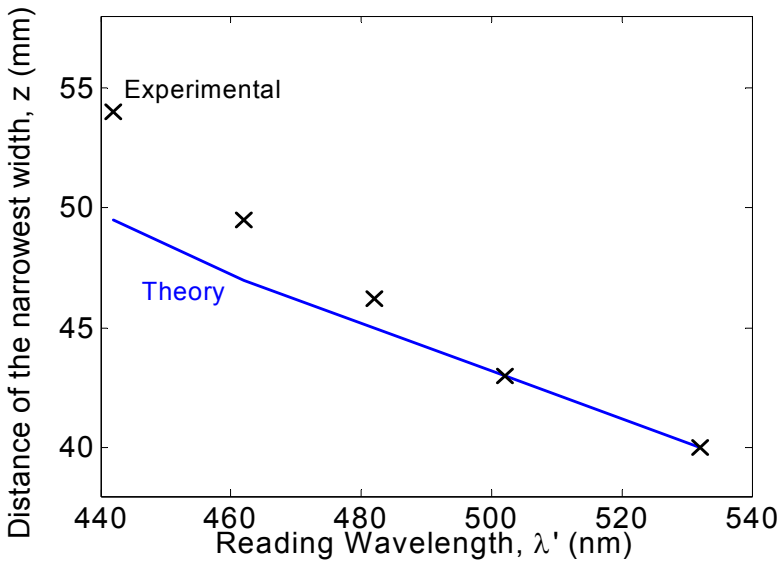

Figure 8.5. Variation of the location of the minimal width of the output when the hologram is read using incoherent beams at different wavelengths. All the other parameters are the same as those mentioned in the caption of Figure 8.3.

8.5 Multi-grating method and coupled wave theory

As mentioned before, the multi-grating method is based on the Born approximation. In this approximation, the depletion of the reading beam in the diffraction process is neglected. As we explained in Chapter 7, this assumption is valid for the weak modulation of the permittivity corresponding to low diffraction efficiency of the hologram. We know from the analysis of the slitless spectrometer in Chapter 7 that

increasing the thickness of the hologram is necessary to enhance the resolution of the spectrometer. In the cases of high diffraction efficiency and thick hologram, which are desired for implementing the slitless spectrometer, the depletion of the reading beam becomes very important. Therefore, the extension of the multi-grating method is needed to be able to accurately analyze the holograms in these cases.

To understand the importance of having such an accurate model, we compare the experimental results for the diffracted crescent from a weak and a strong spherical beam volume holograms. Both the holograms were recorded in the configuration of Figure 7.1(a) with $d = 4$ cm, $a = 0$, $\theta_r = 35^\circ$, and $L = 400$ μm. The recording wavelength was $\lambda = 532$ nm. The first SBVH was recorded for a few seconds (we refer to it as the weak hologram) while the second SBVH was recorded for more than a minute (strong hologram). Both the holograms were then put in the slitless spectrometer setup (Figure 7.4) to monitor the output for a monochromatic input beam. The light from a lamp passed through a spectrometer with the output slit size of 300 μm and then illuminate the hologram in the slitless spectrometer setup. The central wavelength of the reading beam is selected to be at 532 nm with a FWHM of about 1.5 nm. The focal length of the Fourier transforming lens in the spectrometer setup is 3 cm.

Figure 8.6 (a) and (b) show the profile of the output crescent for the weak and strong holograms, respectively. The crescent profile for the weak hologram is what we expect from our analysis; a narrow main lobe with very small side lobes (see Figure 7.2 for the two-dimensional pattern of the output crescent). However in the case of the strong hologram, very large side lobes are observed that cannot be modeled by the methods

described so far. Also, the main lobe is almost replaced by a null and the two side lobes are very strong with almost equal intensity.

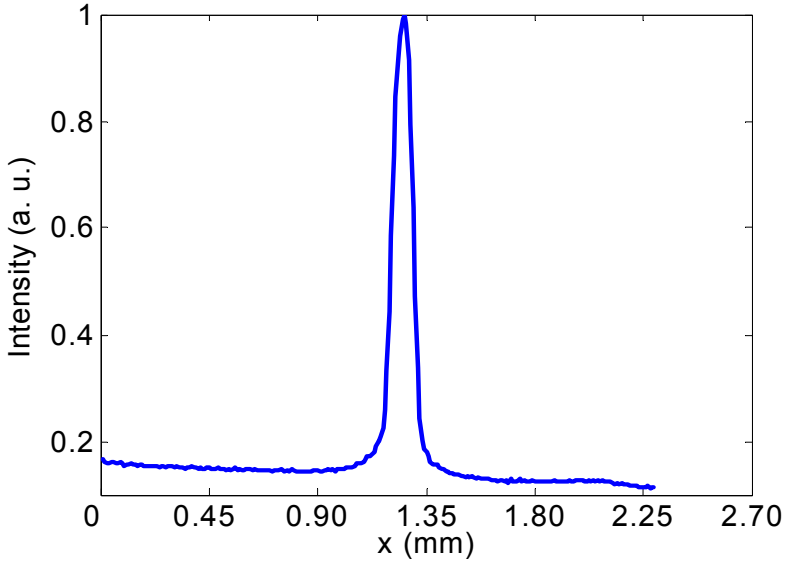

(a)

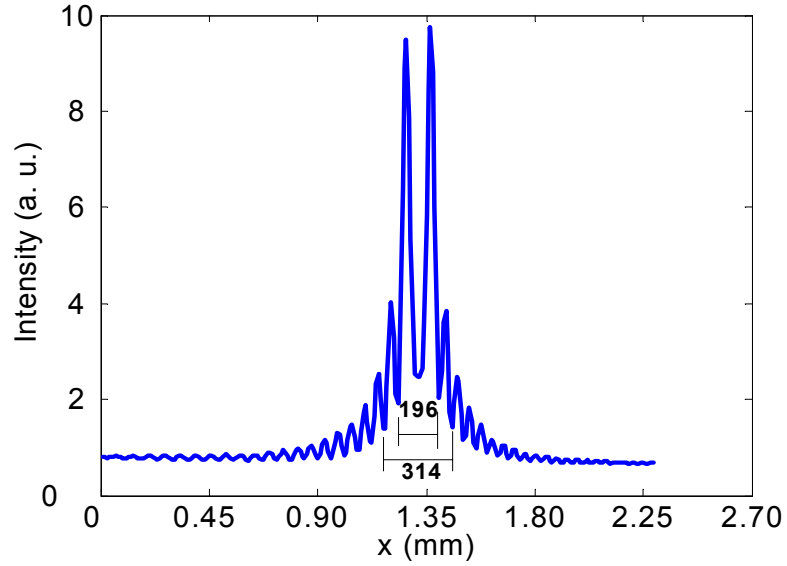

(b)

Figure 8.6. The profile of the output pattern in the slitless spectrometer configuration for (a) a weak and (b) a strong SBVH. Both the holograms were recorded in the configuration of Figure 7.1(a) with d = 4 cm, a = 0, θ_r = 35°, and L = 400 μm. The recording wavelength was 532 nm. The recording time for the hologram in (b) was more than that for (a). The holograms were monitored in the slitless spectrometer setup (Figure 7.3) with f = 6.5 cm. The monochromatic beam at the wavelength of 532 nm reads the holograms.

From the multi-grating analysis of Chapter 7 we know that the cross section of the crescent intensity can be represented by a $sinc^2$. We can assume that the variation of the crescent intensity in Figure 8.6(b) was originally a $sinc^2$ function but it is distorted in the regions corresponding to high diffraction efficiencies because of the coupling of the diffracted components to the reading beam. This assumption can be tested by finding the ratio of the distance between the third zeros on each side to the second zeros of intensity as shown in Figure 8.6(b). The ratio is 314/196 that is very close to the ratio of 6/4 that we expect from a $sinc^2$ function. In other word, the relative position of the second and third nulls is the same as that for a $sinc^2$ function. Therefore, we can expect by considering the coupling of the diffracted components we will be able to accurately model strong SBVH holograms.

To formulize the multi-grating theory based on the coupled wave analysis we start with the representation of the hologram as the summation of several gratings recorded using the reference plane wave and the plane wave components of the spherical beam as outlined in Chapter 6. Therefore, the grating recorded by a reference plane wave with a wave vector (k_{rx}, 0, k_{rz}) and a spherical beam represented by its wave vector components (k_x, k_y, k_z) can be represented as

$$\Delta\varepsilon(\mathbf{r}') = \iint_{k_x,k_y} \varepsilon_1 A_r A_s^*(k_x, k_y, z') e^{j\mathbf{K}_g \cdot \mathbf{r}'} dk_x dk_y + \text{c.c.}, \tag{8.13}$$

where the grating vector $\mathbf{K}_g$ is given by

$$\mathbf{K}_g = (k_{rx} - k_x)\hat{\mathbf{x}}' + (-k_y)\hat{\mathbf{y}}' + (k_{rz} - k_z)\hat{\mathbf{z}}' . \tag{8.14}$$

We suppose that the reading beam at wavelength λ' is a plane wave that has a wave vector of (k'_{px}, k'_{py}, k'_{pz}). Therefore, we need to write the coupled wave equations for the reading beam and the set of the grating vectors represented in Equation (8.13). Again we analyze the hologram in the *x*-*z* plane only corresponding to the expansion of the grating in the *x*-direction only. We also sample the grating components with a sampling period of Δk to be able to form a set of linear equations for coupled wave analysis. Therefore, we can represent the sampled grating with the complex amplitude $\kappa(m)$ and the grating vector $\mathbf{K}_g(m)$ as

$$\Delta\varepsilon(\mathbf{r}') = \sum_{m=1}^{M} \kappa(m) e^{j\mathbf{K}_g(m)\cdot\mathbf{r}'} + \text{c.c.}, \tag{8.15}$$

where M is the total number of the grating components and $\kappa(m) = \varepsilon_1 A_r A_s^* \Delta k$. In the most general case of the rigorous coupled wave analysis [10] the coupling between all the diffracted orders are considered. If we assume N diffracted order for each grating, we need to solve an eigenvalue problem of the size of $2N^M$. If we consider coupled wave analysis (assuming slow energy exchange between diffracted orders [9]), the size of the eigenvalue problem reduces to N^M. For the analysis of the spherical beam volume hologram we usually need considerable number of gratings (usually $M > 100$ and $N > 10$). Therefore, it is not practical to use either of these methods. Also, for the practical applications, most of the diffracted components considered in these two methods do not have considerable power. Therefore, careful selection of the diffracted components results in a reasonable size of the eigenvalue problem that can be solved with available computation capabilities.

When we read the set of M gratings of the spherical beam volume hologram, we have at least M diffraction components. In the Born approximation, we only considered these components. We also neglected the coupling between these components and the reading beam. However, when the diffraction efficiency of some of the grating components becomes considerably large, we have to consider the coupling between the diffracted components and the reading beam. Furthermore, the strong diffracted components can diffract from some of the gratings and this effect should be also considered in the analysis. In this case, we consider the diffraction from the reading beam and diffraction caused by the diffracted beam as it propagates inside the hologram. The coupling is taken into account between all the components. Therefore, the size of the eigenvalue problem is reduced to at most M^2, while all the diffracted components with considerable power are considered in the model. Following the same approach as the couple wave theory [9, 76], we find a set of differential equations for the diffracted plane wave components as

$$\frac{\sigma_z(i)}{k}\frac{dA_d(i)}{dz} + j\kappa(i)A_p + j\left(\frac{k^2-\sigma(i)^2}{2k}\right)A_d(i) + j\sum_{\substack{m=1\\ m\neq i}}^{M}\kappa(m)A_d(iM+m) = 0, \quad i=1,\ldots,M \tag{8.16}$$

$$\frac{\sigma_z(i)-K_{gz}(m)}{k}\frac{dA_d(iM+m)}{dz} + j\kappa(m)A_d(i) + j\left(\frac{k^2-\left|\boldsymbol{\sigma}(i)-\mathbf{K}_{\mathbf{g}}(m)\right|^2}{2k}\right) = 0, \quad \begin{matrix} i,m=1,\ldots,M \\ i\neq m \end{matrix} \tag{8.17}$$

$$\frac{k_{rz}}{k}\frac{dA_p}{dz} + j\sum_{m=1}^{M}\kappa(m)A_d(m) = 0\,, \tag{8.18}$$

where $A_d(i)$ is the complex amplitude of the i'th component of the diffracted electric field, A_p is the complex amplitude of the reading beam, the m'th components of the grating vector in the z-direction and the grating amplitude are represented by $K_{gz}(m)$ and $\kappa(m)$, respectively, and $|x|$ represents the amplitude of x. The i'th component of the wave vector of the diffracted components is

$$\boldsymbol{\sigma}(i) = \mathbf{k_p} + \mathbf{K_g}(i)\,. \tag{8.19}$$

The initial condition of the set of equations is

$$A_p\big|_{z=0} = A_{p0} \;\; and \;\; A_d(i)\big|_{z=0} = 0, i = 1,...,M^2 \tag{8.20}$$

Rewriting the equations in the matrix format, we have

$$\frac{d}{dz}\mathbf{A}_d = \mathbf{C}\,\mathbf{A}_d\,. \tag{8.21}$$

To find the amplitude matrix of the diffracted beam, we first need to solve for the eigenvalues and eigenvectors of the matrix **C**. Then we use the initial condition to completely calculate all the diffracted components [10].

We now use the method to simulate the diffraction from a strong spherical beam volume hologram. We assume the hologram is recorded in the configuration of Figure 7.1(a) using a plane wave with an incident angle of 25º and a point source located at d = 9 cm and a = 0 from the hologram. The recording wavelength is λ = 532 nm. For

simplicity, we assume the refractive index of the recording material is n = 1 and the reading plane wave reads the hologram from the normal direction. We consider a limited number of grating components (M = 30 to 35) to be able to form a matrix with a reasonable size for solving eigenvalue problem. We assume the hologram is read in the slitless spectrometer setup (Figure 7.3) in which a Fourier transforming lens with a focal length of f = 6.5 cm is located after the hologram and the output is monitored on a CCD camera located at the focal plane of the lens. In this case, the outputs at different locations on the CCD correspond to plane wave components of the diffracted beam from the hologram. We then analyze the hologram with different thicknesses to observe the effect of the coupling between the diffracted components as the hologram becomes thicker. The intensity profile of the output is shown for different hologram thicknesses in Figure 8.7.

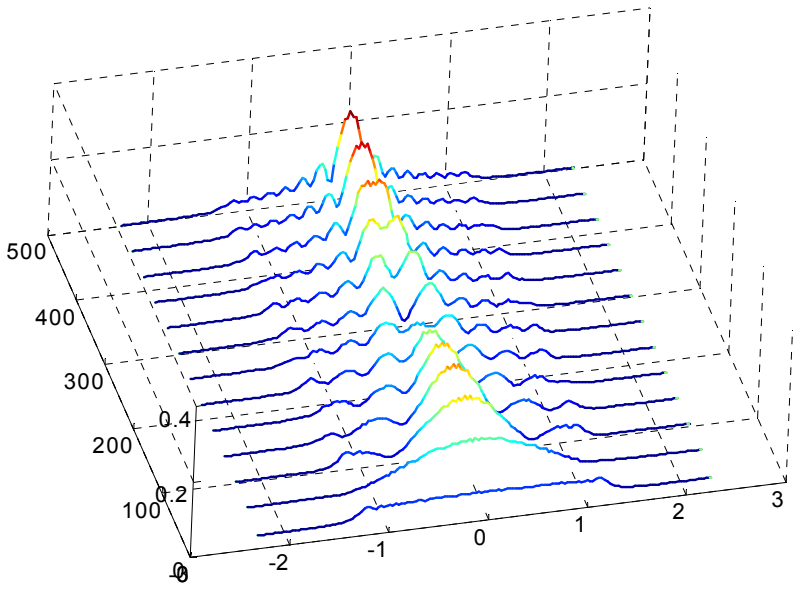

Figure 8.7. The intensity profile of the output of the a slitless spectrometer (Figure 7.3) implemented using holograms with different thicknesses. The parameters of the recording for the holograms are the same.

As it is clearly seen, almost all the diffracted components have low intensity in the case of the thin grating (thickness about 30 μm). As the hologram becomes thicker and thicker the Bragg selectivity becomes more important and a limited number of the diffracted components with considerable intensity are diffracted. Also, the side lobes become more important as the beams propagate in a thicker hologram and have a better chance of coupling. At some point, for example for the hologram with a thickness of about 250 μm, the intensity of the side lobes becomes more than the intensity of the main lobe and the main lobe becomes almost a null. This is similar to what we observed in the experimental result of Figure 8.6(b). Note that the exact simulation of the experimental results needs considerable grating components and a very large matrix for eigenvalue problem. The storage and processing of such a large matrix is beyond the capability of the available computer facilities.

It should be mentioned that the extension of the multi-grating method based on the coupled wave analysis provides a practical solution to understand the diffraction properties of a strong spherical beam volume hologram. The exact simulation of these holograms is not the aim of this work since for the spectroscopic applications we prefer to have only a main lobe in the output with very small side lobes [similar to what we observed in Figure 8.6(a)]. Using the method developed in this section we are able to explain unexpected experimental observation of Figure 8.6(b). The method, within its computation limitations, can be used to analyze strong spherical beam volume holograms. To the best of our knowledge, these holograms cannot be accurately analyzed using any other technique and our method is the only one that can analyze these structures with the current computation facilities.

8.6 Conclusion

The multi-grating method is generalized in this chapter to analyze a complicated hologram recorded using two arbitrary beams. We showed that the analysis of a complicated hologram is similar to the analysis of the spherical beam volume hologram we previously derived in Chapter 6. We presented two different models for the analysis of a complicated hologram. In the first model, the hologram is represented as the summation of the sinusoidal gratings formed by the plane wave components of the signal and the reference beams. In the second model, the three-dimensional Fourier transform of the change in the permittivity of the hologram is used to obtain the sinusoidal grating components. The superposition of the diffracted plane waves from the grating components forms the diffracted beam in the both models. We used the method to analyze a hologram recorded using two spherical beams and the results were compared with the experimental ones.

Another extension to the multi-grating method is introduced based on the coupled wave analysis. This version of the multi-grating method can be used to analyze strong holograms. We used the method for the analysis of a SBVH and successfully explained the experimental results for the diffraction from a strong hologram. The method can be used for a hologram recorded using two arbitrary beams if the same approach as that of generalized multi-grating method is used. In this case, the hologram should be first expanded based on sinusoidal gratings and then the gratings should be used in the coupled wave formulation to find the diffracted components. Although because of high computational cost, this method is limited to holograms that can be represented with limited number of gratings, to the best of our knowledge, this is the only practical method

that can be used for analysis of strong holograms recorded by a plane wave and a complicated beam.

Chapter 9

Future Work and Conclusion

In this chapter, some of the potential extensions to this thesis that can be perused for future research endeavors are briefly discussed. These extensions include global optimization of two-center recording for other doubly doped crystals, extension of stabilized holographic recording system for measuring and controlling the phase of the grating, enhancing the diffraction efficiency in two-center recording using the tunneling effect, recording at high temperature in doubly doped lithium niobate, design of compact spectrometers using cylindrical beam volume holograms, and optimization of holographic based spectrometers. At the end of this chapter, the key conclusions of this dissertation are summarized.

9.1 Global optimization of two-center recording for other doubly doped crystals

The global optimization method we discussed in Chapter 2 is a complete and a general method that can be used for two-center recording in any doubly doped lithium niobate crystal. We performed the detailed analysis and the global optimization for LiNbO3:Fe:Mn. The same approach can be used for analysis and optimization of *M*/# and sensitivity in doubly doped lithium niobate crystals such as $LiNbO_3$:Cu:Ce,

$LiNbO_3$:Tb:Fe, $LiNbO_3$:Ce:Mn, and recently proposed $LiNbO_3$:Fe:Ru. Also, it can be extended for recording in other photorefractive crystals that have the potential of two-center recording such as $LiTaO_3$.

To use the method for these photorefractive crystals, the proper material parameters should be used. Some of these parameters can be found in or calculated from the literature, similar to what we did in Chapter 2. The other parameters should be measured experimentally for these crystals. When we have all the parameters, we can use the two-center model and the optimization approach to obtain the best performance in each case.

9.2 Complete measurement of amplitude and phase of a hologram

The software-based stabilized recording system, we introduced in Chapter 3, has a unique flexibility that can be used to perform different measurements. It can be used to measure and control the phase of the grating during the recording. During the recording in lithium niobate crystals, the grating has always a phase shift relative to the interference pattern [77]. This phase shift that is varying during the recording is mainly due to dominant photovoltaic effect in these crystals. The measurement and also control of this phase can provide useful information about the recording process inside the material.

As we mentioned in Chapter 3, the relative phase of the reference and the signal beam can be set and fixed using the software-based stabilizer. Select the same intensity for the reference and the signal beam, during the recording and for each monitoring interval, we measure the beam at PD_{diff} (Figure 3.1) for three different cases that the reference beam, the signal beam, and both of the beams illuminate the hologram. From

the information of these three measurements, we can find both the amplitude of the diffraction efficiency and the relative phase of the grating with respect to the interference pattern. In another extension to the method, the set point for the relative phase of the reference and the signal beam can be changed in the software during the recording and its effect on the diffraction efficiency and the relative phase of the grating can be measured.

9.3 Enhancing the diffraction efficiency in two-center recording using the tunneling effect

We have reported the enhancement of the diffraction efficiency in $LiNbO_3$:Fe:Mn after the recording and without any external illumination. The reason for this effect is the tunneling of the electrons between the dopants sites in the crystal when the material is doped with high Fe concentration. The same idea can be investigated in other doubly doped lithium niobate crystal. Also, different concentrations as well as different recording conditions can be investigated to obtain the maximum enhancement in the diffraction efficiency. This can be the topic of an extensive research with potentially important applications.

9.4 High temperature recording in other doubly doped lithium niobate

In Chapter 5, we performed thermal fixing experiments in $LiNbO_3$:Fe:Mn crystal. We concluded that the developing ratio is very small in these crystals. Therefore, the thermal fixing and also high temperature recording cannot be performed efficiently in these

materials. We mentioned that some unknown properties of the Mn dopant might be responsible for very low developing ratio since thermal fixing process in $LiNbO_3$:Mn suffers from the same problem. The idea of high temperature recording that potentially enhances the dynamic range of the material can be tested for lithium niobate crystal doped with other dopants. If the developing phase is successful in those crystals, the approach presented in Chapter 5 can be used to find the enhancement in the dynamic range using the high temperature recording.

9.5 Design of compact spectrometers using cylindrical beam volume holograms

We introduced a new class of spectrometers that can be realized using spherical beam volume holograms (SBVHs). In particular, we showed that the entrance slit, the collimating lens, and the dispersive grating of the conventional spectrometer can be replaced with a SBVH in the slitless spectrometer arrangement. Based on multi-grating analysis for the diffraction from the spherical beam volume hologram, we showed that the output beam has a crescent shape. The location of the output crescent is only a function of the input wavelength. Therefore, it can be used to provide the spectral-spatial mapping needed for spectroscopy applications. It is important to note that similar to the conventional spectrometer, the dispersive property of the volume hologram is only observed in one direction in the output plane. The other direction is the direction of the degeneracy of the Bragg condition and does not provide any spectral information. Therefore in SBVH based spectrometer, a linear 1-D detector array can be used to

provide the information for the spectroscopy. The rest of the output crescent will not be used for the spectrum estimation that limits the power efficiency of the system.

Similar to the spherical beam volume hologram, we can design a specific hologram that shows different functionality in the two orthogonal directions in the output plane. For example, the hologram does the spectral mapping in one direction while it does not affect the beam in the other direction. This idea can be implemented using a cylindrical beam volume hologram (CBVH) recorded using a plane wave and a cylindrical beam. While the dispersion property of the hologram is observed in one direction, the beam can be independently modified in the orthogonal direction, providing more flexibility in the design of spectrometers.

The methods of implementation of such holograms and the potential improvement of the system performance can be an important topic of the research. Almost all the ideas investigated for SBVH can be also tested using CBVH. Our method of analysis which is for the general case of 3-dimensional beams can be easily implemented for 2-dimensional analysis of CBVH with less limitation for numerical simulations.

9.6 Optimization of holographic based spectrometers

We presented a general multi-grating method for analysis of a hologram recorded using two arbitrary beams. The method was used to investigate the properties of a hologram recorded using two spherical beams. A lensless spectrometer can be implemented using such a hologram. In this case, the spectrometer consists of a hologram recorded using two spherical beam and a detector. We showed that the output beam at different wavelengths is focused at different distances from the hologram. This limits the resolution of the

spectrometer since the detector cannot be optimally located to capture minimum width of the output at different wavelengths. However, our analytic method can be used to design an optimum hologram to reduce the effect of this problem or completely solve it. In general, we can use the multi-gratin method to design and optimized an arbitrary hologram for different spectroscopic applications.

9.7 Conclusion of dissertation

The main contributions of this thesis are as follows:

1. A global optimization scheme for two-center holographic recording in doubly-doped crystals is proposed. Our method is based on a combination of analytic formulas with numerical simulations. We considered both *M/#* and sensitivity in our method. The global optimum set of design parameters is found by varying all parameters simultaneously. The method is implemented for $LiNbO_3$:Fe:Mn crystals and the optimum set of parameters for maximizing *M/#* and *S* at different reading and sensitizing wavelengths are obtained.
2. The complete variation of the sensitivity with different design parameters in two-center recording is investigated in details. It is shown, both theoretically and experimentally, that the sensitivity in two-center recording is a function of the ratio of the recording to sensitizing intensities and not the absolute intensities.
3. The evidence of electron tunneling in a $LiNbO_3$:Fe:Mn crystal doped with high Fe concentration is presented for the first time. It is shown experimentally that the electron concentration in $LiNbO_3$:Fe:Mn can increase the diffraction efficiency after the recording even when the hologram is kept in dark.

4. The model for the two-center recording is modified to include the effect of electron tunneling in doubly doped crystals with high dopant concentration. It is shown that depending on the recording condition, the tunneling can increase or decrease the diffraction efficiency after the recording.
5. It is shown theoretically that recording at high temperature can result in an improvement in the dynamic range of the material. During the recording at high temperature, the protons migrate to compensate the electronic charge pattern. Therefore, the space-charge field is reduced and the preventing force is decreased. As a result, the modulated electron concentration (and the modulated proton concentration) can be recorded with larger amplitude. When the hologram is cooled to room temperature, illuminating with a beam with a uniform intensity reveal the hologram stored by the protons. In theory, this hologram can have a higher dynamic range compared to the one that is recorded directly by redistributing the electrons.
6. A simple and efficient technique for the analysis of diffraction from a hologram recorded using a plane wave and a complicated beam is presented. The method is called multi-grating method and is used for the analysis of spherical beam volume holograms as spectral diversity filters. It is shown that the method can predict the experimental results with good accuracy. In particular, it is shown that the diffraction of such a SBVH read by a monochromatic plane wave is a crescent-shape pattern.
7. The multi-grating method is generalized to analyze a complicated hologram recorded using two arbitrary beams. Two different models for the analysis of a

complicated hologram are presented. In the first model, the hologram is represented as the summation of the sinusoidal gratings formed by the plane wave components of the signal and the reference beams. In the second model, the three-dimensional Fourier transform of the change in the permittivity of the hologram is used to obtain the sinusoidal grating components. The superposition of the diffracted plane waves from the grating components forms the diffracted beam in the both cases.

8. The multi-grating method is further extended based on the coupled wave analysis to analyze holograms with large change in the permittivity. Based on this model, the properties of such holograms can be explained.
9. A new class of optical devices that integrates the functionalities of different optical elements into a simple volume hologram is introduced. As a result, very compact, low cost, and easy to use devices such as portable spectrometers can be made with particular applications in biological and environmental sensing. As an example of such devices, a slitless volume holographic spectrometer lumps three elements (the entrance slit, the collimator, and the diffractive element) of the conventional spectrometer into one spherical beam volume hologram. Besides being compact and low cost, this spectrometer is less sensitive to alignment issues.

Appendix A

Derivation of the Analytic Solution for the Recording Phase

Considering the steady state solution of the Equations (2.6)-(2.13) by setting all the time derivatives to zero and solving for E_1 we find:

$$E_{SC} = E_1\big|_{t\to\infty} \approx \frac{-1}{\varepsilon\varepsilon_0}\left[\frac{B_S\gamma_S\left(N_S - N_{S0}^-\right) + B_D\gamma_D\left(N_D - N_{D0}^-\right)}{C_S\gamma_S\left(N_S - N_{S0}^-\right) + C_D\gamma_D\left(N_D - N_{D0}^-\right)}\right] m I_{L0}, \tag{A1}$$

where the B and C coefficients are:

$$B_S = \left(\kappa_{S,L}N_{S0}^- + \kappa_{D,L}N_{D0}^-\right)\left(q_{D,L}s_{D,L}I_{L0} + q_{D,H}s_{D,H}I_H + \gamma_D n_0\right)$$

$$+ q_{D,L}s_{D,L}N_{D0}^-\left[\left(\kappa_{S,L} - \kappa_{D,L}\right)I_{L0} + \left(\kappa_{S,H} - \kappa_{D,H}\right)I_H\right], \tag{A2}$$

$$B_D = \left(\kappa_{S,L}N_{S0}^- + \kappa_{D,L}N_{D0}^-\right)\left(q_{S,L}s_{S,L}I_{L0} + q_{S,H}s_{S,H}I_H + \gamma_S n_0\right)$$

$$+ q_{S,L}s_{S,L}N_{S0}^-\left[\left(\kappa_{D,L} - \kappa_{S,L}\right)I_{L0} + \left(\kappa_{D,H} - \kappa_{S,H}\right)I_H\right], \tag{A3}$$

$$C_S = \left[\frac{e\mu n_0}{\varepsilon\varepsilon_0} + \frac{iK}{e}\left(\kappa_{S,L}I_{L0} + \kappa_{S,H}I_H\right)\right]\cdot\left(q_{D,L}s_{D,L}I_{L0} + q_{D,H}s_{D,H}I_H + \gamma_D n_0\right), \tag{A4}$$

$$C_D = \left[\frac{e\mu n_0}{\varepsilon\varepsilon_0} + \frac{iK}{e}\left(\kappa_{D,L}I_{L0} + \kappa_{D,H}I_H\right)\right]\cdot\left(q_{S,L}s_{S,L}I_{L0} + q_{S,H}s_{S,H}I_H + \gamma_S n_0\right), \tag{A5}$$

and variables N_{S0}^{-}, N_{D0}^{-}, and n_0 are given by:

$$N_{S0}^{-} = \frac{\left\{\left[\Gamma_D\left(N_D - N_A\right) - \Gamma_S\left(N_S - N_A\right)\right]^2 + 4\Gamma_D\Gamma_S N_D N_S\right\}^{1/2}}{2\left(\Gamma_D - \Gamma_S\right)}$$

$$- \frac{\Gamma_S\left(N_S + N_A\right) + \Gamma_D\left(N_D - N_A\right)}{2\left(\Gamma_D - \Gamma_S\right)}, \tag{A6}$$

$$N_{D0}^{-} = N_A - N_{S0}^{-}, \tag{A7}$$

$$n_0 = \frac{\left(\Gamma_D/\gamma_S\right)N_{S0}^{-} + \left(\Gamma_S/\gamma_D\right)N_{D0}^{-}}{\gamma_S\left(N_S - N_{S0}^{-}\right) + \gamma_D\left(N_D - N_{D0}^{-}\right)}, \tag{A8}$$

and coefficients Γ_S and Γ_D are:

$$\Gamma_S = \gamma_S\left(q_{D,L}s_{D,L}I_{L0} + q_{D,H}s_{D,H}I_H\right), \tag{A9-a}$$

$$\Gamma_D = \gamma_D\left(q_{S,L}s_{S,L}I_{L0} + q_{S,H}s_{S,H}I_H\right). \tag{A9-b}$$

All other variables and parameters are defined in Table 2.1.

For finding the recording time constant, we should find the differential equation for the space-charge field. Since the space-charge field is proportional to $N_{S1}^{-} + N_{D1}^{-}$, by using Equation (2.9) through Equation (2.12) and by proper substitutions we find a second order linear differential equation with time-varying coefficients for the space-charge field. To find an approximate formula for recording time constant, we assume that the space-charge field can be represented by a mono-exponential function of time. Assuming that the zeroth order terms reach their steady state values much faster than the

first order terms (this is justified by using numerical simulations) results in a first order differential equation with constant coefficient for $N_{S1}^{-}+N_{D1}^{-}$. In this case the recording time constant can be written as:

$$\tau_r \approx \frac{G_S\gamma_S\left(N_S-N_{S0}^{-}\right)+G_D\gamma_D\left(N_D-N_{D0}^{-}\right)}{C_S\gamma_S\left(N_S-N_{S0}^{-}\right)+C_D\gamma_D\left(N_D-N_{D0}^{-}\right)}, \tag{A10}$$

where C_S and C_D are given by Equations (A4) and (A5) and G_S and G_D are defined as:

$$G_S=\left[\frac{e\mu n_0}{\varepsilon\varepsilon_0}+\frac{iK}{e}\left(\kappa_{S,L}I_{L0}+\kappa_{S,H}I_H\right)\right]+\left(q_{D,L}s_{D,L}I_{L0}+q_{D,H}s_{D,H}I_H+\gamma_D n_0\right), \tag{A11}$$

$$G_D=\left[\frac{e\mu n_0}{\varepsilon\varepsilon_0}+\frac{iK}{e}\left(\kappa_{D,L}I_{L0}+\kappa_{D,H}I_H\right)\right]+\left(q_{S,L}s_{S,L}I_{L0}+q_{S,H}s_{S,H}I_H+\gamma_S n_0\right). \tag{A12}$$

For the lithium niobate crystal doped with iron (Fe) and manganese (Mn) and for recording with red and sensitizing with UV the above equations can be simplified further. When the sensitizing intensity is much lower than the recording intensity ($I_{UV}<<I_R$) and the Mn concentration is much less than the Fe concentration, the following approximate formula can be obtained for space-charge field:

$$E_{SC} \approx \frac{\kappa_{Fe,R}N_{Fe0}^{-}}{e\mu n_0} m I_{R0}\times CF\,, \tag{A13}$$

where all the parameters and variable can be found from Table 2.1 by replacing the indices S with Fe, D with Mn, L with R, and H with UV. Similarly N_{Fe0}^{-} can be found from Equation (A6). Also the factor CF is introduced as:

$$CF = \left[1 + \frac{q_{Fe,R} s_{Fe,R} I_{R0} \gamma_{Mn} \left(N_{Mn} - N_{Mn0}^{-}\right)}{H}\right]^{-1}, \tag{A14}$$

where H is defined as:

$$H = q_{Fe,UV} s_{Fe,UV} I_{UV} \gamma_{Mn} \left(N_{Mn} - N_{Mn0}^{-}\right) + q_{Mn,UV} s_{Mn,UV} I_{UV} \gamma_{Fe} \left(N_{Fe} - N_{Fe0}^{-}\right)$$

$$+ \gamma_{Fe} \gamma_{Mn} n_0 \left(N_{Mn} + N_{Fe} - N_A\right)$$

For the same condition (i.e. $I_{UV} << I_R$ and $N_{Mn} << N_{Fe}$), the recording time constant is approximately given by:

$$\tau_r \approx \left(\frac{\varepsilon \varepsilon_0}{e \mu n_0}\right) + \left[\frac{\gamma_{Fe} \left(N_{Fe} - N_{Fe0}^{-}\right) + \gamma_{Mn} \left(N_{Mn} - N_{Mn0}^{-}\right)}{H}\right]. \tag{A15}$$

Appendix B

Simplifying the Reading Phase

Finding the analytic solution for the readout phase is very difficult. The main problem is that we cannot further assume that the average electron concentrations in the shallower and the deeper traps are constant. In this case, we should solve all the zeroth and first order equations simultaneously, and a closed form solution cannot be found easily. Since the most important part of the solution in this phase is the final value for the space-charge field, we concentrate on finding this value. During the readout process, the reading beam excites electrons from the shallower traps to the conduction band. These electrons will be eventually trapped and remain in the deeper traps. It is expected that varying the intensity of the reference beam only changes the dynamics of the process and does not affect the final electron concentrations in the deeper traps. Simulating the readout phase by reference beams with different intensities agrees very well with this observation and shows that the final electron concentration in deeper traps (and therefore, the final space-charge field) is independent of the intensity of the readout beam (See Figure 2.4). Using this fact we can assume an appropriate variation of the reading beam intensity with time to simplify the equations. This intensity variation is given by:

$$I_R(t) = I_0\left[\frac{\gamma_{Fe}N_{Fe}}{\gamma_{Mn}\left(N_{Mn} - N_A + N_{Fe0}^{-}(t)\right)} + 1\right], \tag{B1}$$

where I_0 is a constant intensity and all other variables and parameters can be found from Table 2.1 by replacing the indices S with Fe, and D with Mn. Since we are interested in $LiNbO_3$:Fe:Mn crystals, we used the proper notation for this crystal in Equation (B1). We further assume that $N_{Fe0}^{-} << N_{Fe}$. This assumption is acceptable since for practical $LiNbO_3$:Fe:Mn crystals, N_A is much less than Fe concentration. Also the average electron concentration in the Fe traps (N_{Fe0}^{-}) is continuously decreasing with time during readout. Therefore, except at the very early stage of readout, the assumption $N_{Fe0}^{-} << N_{Fe}$ is valid.

Solving for N_{Fe0}^{-} from the zeroth order equations results in:

$$N_{Fe0}^{-}(t) = N_0 \exp\left(-q_{Fe,R} s_{Fe,R} I_0 t\right), \tag{B2}$$

where N_0 is the concentration of Fe^{2+} traps at the beginning of the readout, i.e., $N_0 = N_{Fe0}^{-}(t=0)$, and $q_{Fe,R}\ s_{Fe,R}$ is the absorption cross section of red photons to excite electrons from Fe traps to the conduction band. Then, we find N_{Mn0}^{-} and n_0 using Equations (A7) and (A8) and substitute all the zeroth order terms in the first order equations. In the next step, we change the variable from time (t) to $W=N_{Mn}-N_A+N_{Fe0}^{-}(t)$. The derivative with respect to time (*i.e.*, *d/dt*) will be replaced by:

$$\frac{d}{dt} = -q_{Fe,R} s_{Fe,R} I_0 \left(W - N_{Mn} + N_A\right) \frac{d}{dW}.$$

Note that N_{Mn} and N_A are constant with time and $W-N_{Mn}+N_A = N_{Fe0}^{-}(t)$ is given by Equation (B2).

After some algebraic manipulations, we reach the following differential equation for the space-charge field:

$$P(W)\frac{d^2E_1}{dW^2}+Q(W)\frac{dE_1}{dW}+R(W)E_1=0\,, \tag{B3}$$

where the coefficients are given by

$$P(W)=\gamma_{Mn}W^2\left(\gamma_{Mn}W^2+\left[\gamma_{Fe}N_{Fe}+\gamma_{Mn}\left(N_A-N_{Mn}\right)\right]\cdot W+\gamma_{Fe}N_{Fe}\left(N_A-N_{Mn}\right)\right), \tag{B4}$$

$$Q(W)=-W\left\{\gamma_{Mn}\left(\frac{e\mu}{\varepsilon\varepsilon_0}+\gamma_{Fe}\right)W^2\right.$$

$$+\left[\frac{e\mu}{\varepsilon\varepsilon_0}\left(\gamma_{Fe}N_{Fe}+\gamma_{Mn}\left(N_A-N_{Mn}\right)\right)+\gamma_{Fe}\gamma_{Mn}\left(N_A-N_{Mn}\right)+\frac{iK\kappa_{Fe,R}}{eq_{Fe,R}s_{Fe,R}}\gamma_{Fe}\gamma_{Mn}N_{Fe}\right]W$$

$$\left.+\left(\frac{e\mu}{\varepsilon\varepsilon_0}\gamma_{Fe}N_{Fe}\left(N_A-N_{Mn}\right)+\frac{iK\kappa_{Fe,R}}{eq_{Fe,R}s_{Fe,R}}\gamma_{Fe}^2N_{Fe}^2\right)\right\}, \tag{B5}$$

$$R(W)=\frac{e\mu}{\varepsilon\varepsilon_0}\left(\gamma_{Fe}+\gamma_{Mn}\right)W^2$$

$$+\left[\frac{e\mu}{\varepsilon\varepsilon_0}\left[\gamma_{Fe}N_{Fe}+\left(\gamma_{Fe}+\gamma_{Mn}\right)\left(N_A-N_{Mn}\right)\right]+\frac{iK\kappa_{Fe,R}}{eq_{Fe,R}s_{Fe,R}}\gamma_{Fe}\gamma_{Mn}N_{Fe}\right]W$$

$$+\left(\frac{e\mu}{\varepsilon\varepsilon_0}\gamma_{Fe}N_{Fe}\left(N_A-N_{Mn}\right)+\frac{iK\kappa_{Fe,R}}{eq_{Fe,R}s_{Fe,R}}\gamma_{Fe}^2N_{Fe}^2\right), \tag{B6}$$

and all the parameters can be found from Table 2.1 by replacing the indices S with Fe, D with Mn, and L with R. To find the final space-charge field (after sufficient readout), we should solve the differential equation (B3) and find the solution at $W=N_{Mn}-N_A$. The initial conditions at $t=0$, or $W(t=0)=W_0= N_{Mn}-N_A+ N_0$, are:

$$E_1(W_0) = E_1(t=0) = E_{SC}\,, \tag{B7}$$

$$\left.\frac{dE_1}{dW}\right|_{W=W_0} = \left(\frac{e}{\varepsilon\varepsilon_0}\right)^2 \frac{\mu}{iK}\frac{1}{\gamma_{Mn}W_0} + \frac{\kappa_{Fe,R}}{\varepsilon\varepsilon_0 q_{Fe,R}s_{Fe,R}}\frac{1}{N_0}\left(1+\frac{\gamma_{Fe}N_{Fe}}{\gamma_{Mn}W_0}\right)N_{Fe1}^{-}(t=0)\,. \tag{B8}$$

where, E_{sc} and $N_{Fe1}^{-}(t=0)$ are the saturation space-charge field and first order electron concentration in Fe traps at the beginning of the readout ,respectively. Both E_{sc} and $N_{Fe1}^{-}(t=0)$ are calculated from the analytic solution of the recording phase.

Appendix C

Derivation of Multi-Grating Method

When a medium with a small perturbation in permittivity [$\Delta\varepsilon(\mathbf{r}')$] is illuminated by an incident beam $\mathbf{E}_p$, the diffracted electric field $\mathbf{E}_d$ at position $\mathbf{r}$ is found using the Born approximation [11]

$$\mathbf{E}_d(\mathbf{r}) = \frac{1}{4\pi}\int_V \frac{e^{jk|\mathbf{r}-\mathbf{r}'|}}{|\mathbf{r}-\mathbf{r}'|}\nabla'\times\nabla'\times\left[\frac{\Delta\varepsilon(\mathbf{r}')}{\varepsilon_0}\mathbf{E}_p(\mathbf{r}')\right]dv', \tag{C1}$$

where the integration is over the volume V, ε_0 is the average (unperturbed) permittivity of the medium, and $\mathbf{r}' = (x', y', z')$ is a position vector in the volume V. In holographic recording, the perturbation in permittivity is caused by the interference between the reference plane wave ($\mathbf{E}_r$) and the signal beam ($\mathbf{E}_s$) during the recording. The polarizations of these fields are considered to be the same for practical cases. In general, the two beams are obtained from a single linearly polarized beam using a beam splitter. Therefore, we consider the scalar values of the field (E_r and E_s) in our analysis. The perturbation in permittivity in the interference region is

$$\Delta\varepsilon(\mathbf{r}') = \varepsilon_1 E_r(\mathbf{r}')E_s^*(\mathbf{r}') + \text{c.c.} \tag{C2}$$

where ε_1 is a proportional constant, the elevated star (*) shows the complex conjugate operation, and c.c. means the complex conjugate of the preceding term. In the following we consider the first term in Equation (C2) only, since the contribution from the complex

conjugate can be found similarly. Suppose that we represent the signal beam (E_s) in a plane parallel to $x'y'$ plane using its Fourier components as

$$E_s(\mathbf{r}') = \iint_{k_x,k_y} A(k_x,k_y,z')\, e^{j\left(k_x x' + k_y y'\right)} dk_x dk_y \,, \tag{C3}$$

where the integration is over all values of k_x and k_y. Note that we consider all the factors (such as $1/4\pi^2$ in inverse Fourier integral) into the each component $A(k_x, k_y, z')$.

We substitute $\Delta\varepsilon(\mathbf{r}')$ from Equation (C2) into Equation (C1) using the expansion in Equation (C3). Since the curl operators ($\nabla\times$) and the integration in Equation (C1) are functions of $\mathbf{r}'$ only, and the integration in Equation (C3) is a function of k_x and k_y only, we can change the order of integration over k_x and k_y with the curl operation and integration in Equation (C1) to get

$$\mathbf{E}_d(\mathbf{r}) = \iint_{k_x k_y} \left\{ \int_V \frac{\varepsilon_1 e^{jk|\mathbf{r}-\mathbf{r}'|}}{4\pi\varepsilon_0 \,|\,\mathbf{r}-\mathbf{r}'\,|} \nabla'\times\nabla'\times\left[A^*(k_x,k_y,z') e^{-j\left(k_x x' + k_y y'\right)} E_r(\mathbf{r}')\mathbf{E}_p(\mathbf{r}')\right] dv' \right\} dk_x dk_y \tag{C4}$$

where V indicates the whole volume where the hologram is recorded. If the reading beam ($\mathbf{E}p$) is a plane wave, the integral over the volume (V) in Equation (C4) is the diffraction from a simple grating formed by the reference plane wave (E_r) and the plane wave component from Fourier representation of the signal beam. This diffraction of a plane wave from a simple grating using Born approximation is treated in detail in the literature (for example see Ref. [71]). After calculating diffracted plane wave component,

$\widetilde{\mathbf{E}}(k_x, k_y, z')$, from integration over the holographic volume in Equation (C4), total diffracted field is found from

$$\mathbf{E}_d(\mathbf{r}) = \iint_{k_x k_y} \widetilde{\mathbf{E}}(k_x, k_y, z')\, dk_x dk_y \quad . \tag{C5}$$

In order to extend this approach for reading with an arbitrary beam, we can expand the reading beam into its plane wave components. We find the diffracted beam from each component using Equation (C5). Then, the total diffracted beam can be found by combining all the diffracted components.

References

1. D. Gabor, “A new microscopic principle,” Nature 161, 777-778 (1948).

2. P. J. van Heerden, “A new optical method of storing and retrieving information,” Appl. Opt. 2, 387-392 (1963).

3. P. J. van Heerden, “Theory of optical information storage in solids,” Appl. Opt. 2, 393-400 (1963).

4. J. F. Heanue, M. C. Bashaw, L. Hesselink, “Volume holographic storage and retrieval of digital data,” Science 265, 749-752 (1994).

5. D. Psaltis, and F. Mok, “Holographic memories,” Scientific American 273 (5), 70-76 (1995).

6. D. Psaltis and G. W. Burr, "Holographic data storage," Computer 31, 52-60 (1998).

7. G. Barbastathis and D. J. Brady, " Multidimensional tomographic imaging using volume holography," Proc. IEEE 87, 2098-2120 (1999).

8. A. Karbaschi, C. Hsieh, O. Momtahan, A. Adibi, M. E. Sullivan, and D. J. Brady, " Qualitative demonstration of spectral diversity filtering using spherical beam volume holograms," Opt. Express 12, 3018-3024 (2004), www.opticsexpress.org.

9. H. Kogelnik, “Coupled wave theory for thick hologram grating,” Bell Sys. Tech. J. 48, 2909-2947 (1969).

10. T. K. Gaylord and M. G. Moharam, “Analysis and applications of optical diffraction by gratings,” Proc. IEEE 73, 894-937 (1985).

11. J. D. Jackson, Classical Electrodynamics, 2nd Edition, Wiley, New York, 1975.

12. T. A. Shankoff, "Phase holograms in dichromated gelatin" Appl. Opt. 7, 2101-2105 (1968).

13. H. Franke, H. G. Festl, and E. Kratzig, “Light-induced refractive index change in PMMA files doped with Styrene,” Colloid Polym. Sci. 262, 213-216 (1984).

14. D. L. Staebler and J. J. Amodei, “Coupled-wave analysis of holographic storage in $LiNbO_3$,” J. Appl. Phys. 43, 1042-1049 (1972).

15. F. H. Mok, “Angle-multiplexed storage of 5000 holograms in lithium niobate,” Opt. Lett. 18, 915-917 (1993).

16. A. Yariv, S. S. Orlov, and G. A. Rakuljic, “Holographic storage dynamics in lithium niobate**:** Theory and experiment,” J. Opt. Soc. Am. B 13, 2513-2523 (1996).

17. O. Mikami, “Cu-diffused layers in $LiNbO_3$ for reversible holographic storage,” Opt. Commun. 11, 30-32 (1975).

18. P. Hertel, K. H. Ringhofer, and R. Sommerfeldt, “Theory of thermal hologram fixing and application to $LiNbO_3$:Cu,” Phys. Stat. Sol. A 104, 855-862 (1987).

19. J. J. Amodei and D. L. Staebler, “holographic pattern fixing in electro-optic crystals,” Appl. Phys. Lett. 18, 540-542 (1971).

20. X. An, D. Psaltis, G. W. Burr, “Thermal fixing of 10,000 holograms in $LiNbO_3$:Fe,” Appl. Opt. 38, 386-393 (1999).

21. F. Micheron and G. Bismuth, “Electrical control of fixing and erasure of holographic pattern in ferroelectric materials,” Appl. Phys. Lett. 20, 79-81 (1972).

22. J. A. Ma, T. Chang, J. Hong, R. Neurgaonkar, G. Barbastathis, D. Psaltis, “Electrical fixing of 1000 angle-multiplexed holograms in SBN:75,” Opt. Lett. 22, 1116-1118 (1997).

23. H. C. Kulich, “A new approach to read volume holograms at different wavelengths,” Opt. Commun. 64, 407-411 (1987).

24. E. Chuang E, D. Psaltis, “Storage of 1000 holograms with use of a dual-wavelength method,” Appl. Opt. 36, 8445-8454 (1997).

25. D. von der Linde, A. M. Glass, and K. F. Rodgers, “Multiphoton photorefractive process for optical storage in $LiNbO_3$” Appl. Phys. Lett. 25, 155-157 (1974).

26. K. Buse, F. Jermann, and E. Krätzig, “two-step photorefractive hologram recording in $LiNbO_3$:Fe,” Ferroelectrics 141, 197-205 (1993).

27. L. Hesselink, S. S. Orlov, A. Liu, A. Akella, D. Lande, R. R. Neurgaonkar, “Photorefractive materials for nonvolatile volume holographic data storage,” Science 282, 1089-1094 (1998).

28. H. Guenther, R. Macfarlane, Y. Furukawa, K. Kitamura, and R. Neurgaonkar, “Two-color holography in reduced near-stoichiometric lithium niobate,” Appl. Opt. 37, 7611-7623 (1998).

29. K. Buse, A. Adibi, and D. Psaltis, “Non-volatile holographic recording in doubly doped lithium niobate crystals,” Nature 393, 665-668 (1998).

30. A. Adibi, K. Buse, and D. Psaltis, “Two-center holographic recording,” J. Opt. Soc. Am. B 18, 584-601 (2001).

31. O. Momtahan, A. Karbaschi, and A. Adibi, “Gated holography: materials, techniques, and applications,” Proc. of the SPIE, vol. 4988, 24-39 (2003).

32. A. Van der Lugt, “Signal detection by complex spatial filtering,” IEEE Trans. Inf. Theory, IT-10, 139-145 (1964).

33. A. Adibi, K. Buse, and D. Psaltis, “Two-center holographic recording,” J. Opt. Soc. Am. B 18, 584-601 (2001).

34. A. Adibi, K. Buse, and D. Psaltis, “Effect of annealing in two-center holographic recording,” Appl. Phys. Lett. 74, 3767-3769 (1999).

35. C. Moser, B. Schupp, and D. Psaltis, “Localized holographic recording in doubly doped lithium niobate,” Opt. Lett. 25, 162-164 (2000).

36. Y. Liu, L. Liu, and C. Zhou, “Prescription for optimizing holograms in $LiNbO_3$:Fe:Mn,” Opt. Lett. 25, 551-553 (2000).

37. A. Adibi, K. Buse, and D. Psaltis, “Sensitivity improvement in two-center holographic recording,” Opt. Lett. 25, 539-541 (2000).

38. Y. W. Liu, L. R. Liu, Y. C. Guo, and C. H. Zhou, “The dynamics of holographic storage in doubly doped $LiNbO_3$:Fe:Mn,” Acta Physica Sinica 49, 880-886 (2000).

39. Y. W. Liu, L. R. Liu, C. H. Zhou, and L. Y. Xu, “Nonvolatile photorefractive holograms in $LiNbO_3$:Cu:Ce crystals,” Opt. Lett. 25, 908-910 (2000).

40. Y. W. Liu, L. R. Liu, C. H. Zhou, L. Xu, “Photorefractive holographic dynamics in doubly doped $LiNbO_3$:Fe:Mn,” Chinese Phys. Lett. 17, 571-573 (2000).

41. M. Lee, S. Takekawa, Y. Furukawa, K. Kitamura, H. Hatano, and S. Tao, “Angle-multiplexed hologram storage in $LiNbO_3$:Tb, Fe,” Opt. Lett. 25, 1337-1339 (2000).

42. I. G. Kim, M. Lee, S. Takekawa, Y. Furukawa, K. Kitamura, L. Galambos,L. Hesselink, “Volume holographic storage in near-stoichiometric $LiNbO_3$:Ce:Mn,” Japan. J. Appl. Phys. Part 2-Lett. 39, L1094-L1069 (2000).

43. R. Fujimura, S. Ashihara, O. Matoba, T. Shimura, and K. Kuroda, “Enhancement of non-volatile recording by an external field in doubly doped lithium niobate,” in Photorefractive Effects, Materials, and Devices, vol. 62 of OSA Trends in Optics and Photonics Series (Optical Society of America, Delavan, WI, 2001), pp. 212-216.

44. A. Adibi, K. Buse, and D. Psaltis, “The role of carrier mobility in holographic recording in $LiNbO_3$,” Appl. Phys. B 72, 653-659 (2001).

45. D. Liu, L. R. Liu, C. H. Zhou, J. Zhang, and L. Y. Xu, “Experimental study of accumulative recording during nonvolatile holographic storage in $LiNbO_3$:Fe:Mn crystals,” Microwave and Opt. Tech. Lett. 32, 423-425 (2002).

46. F. Jermann and J. Otten, “Light-induced charge transport in $LiNbO_3$:Fe at high light intensities,” J. Opt. Soc. Am. B 10, 2085-2092 (1993).

47. D. Psaltis, D. Brady, and K. Wagner, "Adaptive optical network using photorefractive crystals," Appl. Opt. 27, 1752-1759 (1988).

48. A. Adibi, K. Buse, D. Psaltis, **"**System measure for persistence in holographic recording and application to singly-doped and doubly-doped lithium niobate," Appl. Opt. 40, 5175-5182 (2001).

49. C. Gu, J. Hong, H. Li, D. Psaltis, and P. Yeh, "Dynamics of grating formation in photovoltaic media," J. Appl. Phys. 69, 1167-1172 (1991).

50. I. Nee, M. Müller, K. Buse, and E. Krätzig, "Role of iron in lithium-niobate crystals for the dark-storage time of holograms," J. Appl. Phys. 88, 4282-4286 (2000).

51. Y. P. Yang, K. Buse, and D. Psaltis, "Photorefractive recording in $LiNbO_3$:Mn," Opt. Lett. 27, 158-160 (2002).

52. Y. W. Liu, L. R. Liu, D. A. Liu, L. Y. Xu, C. H. Zhou, "Intensity dependence of two-center nonvolatile holographic recording in LiNbO3 : Cu : Ce crystals," Opt. Commun. 190, 339-343 (2001).

53. E. Kratzig, and H. Kurz, "Photo-induced currents and voltages in $LiNbO_3$," Ferroelectrics 13, 295-296 (1976).

54. E. Kratzig, and H. Kurz, "Photorefractive and photovoltaic effects in doped $LiNbO_3$," Opt. Acta, 24, 475-482 (1977).

55. J. Frejlich, L. Cescato, and G.F. Mendes, "Analysis of an active stabilization system for a holographic setup," Appl. Opt. 27, 1967-1976 (1988).

56. P. Acioly, M. Dos Santos, L. Cescato, and J. Frejlich,"Interference-term real-time measurement for self-stabilized two-wave mixing in photorefractive crystals" Opt. Lett. 13, 1014-1016 (1988).

57. "About Lock-in Amplifiers," Application Note #3, Stanford Research Systems, (1999). Available at http://www.thinksrs.com/downloads/PDFs/ApplicationNotes/AboutLIAs.pdf.

58. "Piezobased Optomechanics," Application Catalogue, Piezomechanik (2003). Available at http://www.piezomechanik.com.

59. K. Peithmann, A. Wiebrock, and K. Buse "Incremental holographic recording in lithium niobate with active phase locking," Opt. Lett. 23, 1927-1929 (1998).

60. J. Y. Beyon, *LabVIEW Programming, Data Acquisition and Analysis*, Prentice Hall PTR, NJ (2001).

61. G. W. Johnson and R. Jennings, *LabVIEW Graphical Programming 3rd edition*, Mcgraw-Hill, NY (2001).

62. Y. Yang, D. Psaltis, M. Luennemann, D. Berben, U. Hartwig, and K. Buse, "Photorefractive properties of lithium niobate crystals doped with manganese ," J. Opt. Soc. Am. B 20, 1491-1502 (2003).

63. D. Liu, L. Liu, Y. Liu, C. Zhou, and L. Xu, "Self-enhanced nonvolatile holographic storage in $LiNbO_3$:Fe:Mn crystals," Appl. Phys. Lett. 77, 2964-2966 (2000).

64. K. Buse, S. Breer, K. Peithmann, S. Kapphan, M. Gao, and E. Kratzig, "Origin of thermal fixing in photorefractive lithium niobate crystals," Phys. Rev. B, vol. 56, pp. 1225-1235, July 15, 1997.

65. A. Karbaschi, O. Momtahan, A. Adibi, and B. Javidi, "Optical correlation using localized gated holography," Opt. Eng. 44, 085802 (2005).

66. C. R. Hsieh, S. H. Lin, K. Y. Hsu, T. C. Hsieh, A. Chiou, and J. Hong, "Optimal conditions for thermal fixing of volume holograms in Fe:$LiNbO_3$ crystals," *Appl. Opt.*, vol. 38, pp. 6141-6151 (1999).

67. Z. Xu, Z. Wang, M. E. Sullivan, D. J. Brady, S. H. Foulger, and A. Adibi, "Multimoldal multiplex spectroscopy using photonic crystals," Optics Express 11, 2126-2133 (2003).

68. P. C. Clemmow, The Plane Wave Spectrum Representation of Electromagnetic Fields, Oxford University Press-IEEE Press, New York, 1996.

69. G. Barbastathis and D. Psaltis, "Volume Holographic Multiplexing Methods," in Holographic Data Storage, H. J. Coufal, D. Psaltis, G. T. Sincerbox Eds., Springer, 2000, pp. 21-59.

70. F. Gori, "Why is the Fresnel transform so little known?" in Current Trends In Optics, J. C. Dainty Ed., Academic Press, 1994, pp. 139-148.

71. G. Barbastathis, M. Levene, and D. Psaltis, "Shift multiplexing with spherical reference waves," Appl. Opt. 35, 2403-2417 (1996).

72. R. T. Ingwall and D. Waldman, "Photopolymer Systems," in Holographic Data Storage, H. J. Coufal, D. Psaltis, G. T. Sincerbox Eds., Springer, 2000, pp. 171-197. Also, www.aprilisinc.com.

73. J. W. Goodman, Introduction to Fourier Optics, 2nd Edition, McGraw-Hill, 1996.

74. C. Hsieh, O. Momtahan, A. Karbaschi, A. Adibi, M. E. Sullivan, and D. J. Brady, "Role of recording geometry in the performance of spectral diversity filters with spherical beam volume holograms," Opt. Lett. 30, 186-188 (2005).

75. S. Kirkpatrick, C. D. Gelatt, and M. P. Vecchi "Optimization by Simulated Annealing," Science 220, 671-680 (1983).

76. R. K. Kostuk, "Comparison of models for multiplexed holograms," Appl. Opt. 28, 771-777 (1989).

77. A. M. Glass, “The photorefractive effect,” Opt. Eng. 17, 470-479 (1978).

Vita

Omid Momtahan obtained a B.S. degree in Electrical Engineering from the University of Shiraz in 1996, ranking first among his graduating class. He was with the Electrical Engineering Department of Sharif University of Technology from 1996, obtaining a M.S.E.E. degree in 1998. Currently, he is a Ph.D. student at the School of Electrical and Computer Engineering, Georgia Institute of Technology. He is the recipient of Outstanding Young Researcher Award, from Optics in the Southeast Conference, Atlanta, GA, in October 2005 and Electrical and Computer Engineering Graduate Research Assistant Excellence Award from School of Electrical and Computer Engineering, Georgia Institute of Technology, in April 2005. He also received the best paper award at the 50th IEEE Vehicular Technology Conference held in Amsterdam, the Netherlands, in September 1999. His technical interests are volume holographic memories, optical spectroscopy, biosensors, biophotonics, optical communications, and wireless communications.